AZAMI, MAHSA. Ph.D. Investigation of Optoelectronic Properties and Anti/Pro-Oxidation Effects of Carbon Nanodots (CNDs) Doped With Different Heteroatoms. (2023)
Directed by Dr. Jianjun Wei. 165 pp.

Owing to unique characteristics, such as low toxicity, outstanding biocompatibility, intrinsically strong photoluminescence, as well as facile synthesis, carbon nanodots (CNDs) have recently been the focal point of different fields of research. However, a full understanding of their potential properties and mechanisms is yet to be achieved. This dissertation focuses on the impacts of doping with two heteroatoms, phosphorus (P) and boron (B), on three major features of CNDs: optoelectronic properties, oxidative stress effects at cellular and genomic levels, and an optical sensing application.

First, we reviewed the cellular uptake, sub-cellular localization, cytotoxicity, and oxidative stress effects of CNDs in cells, and their contributing mechanisms in different diseases associated with oxidative stress. In the second part of this dissertation, different amounts of P and B are incorporated into the structures of CNDs to examine their influence on the optical and anti-oxidation capabilities. Both dopants can increase light absorption and fluorescence, yet in differing ways. In addition, both dopants can boost the radical scavenging capabilities of CNDs in physicochemical conditions.

In the third part of our study, we examined the effects of N, P-CNDs and N, B-CNDs on oxidative stress in normal and cancer cell lines. Using cytotoxicity tests, we attempted to determine the safe concentration range of these CNDs for further biological applications. At varying concentrations, these CNDs behaved differently in terms of their ability to scavenge free radicals, e.g., reactive oxidative species (ROS), in living cells. To study potential genomic effects, we selected three genes associated with anti-oxidation and evaluated the changes upon N,P-CNDs and N,B-CNDs treatment on the expression levels of these genes in both normal and cancer cell lines.

The results indicated that effects and outcomes at the genomic level could differ from those at the cellular level. Overall, it was concluded that both introduced CNDs induced oxidative stress in cancer cells which can be used as effective tools in the direction of pro-oxidant therapy in cancer. However, their final fate in normal cells demonstrated plausible pro-oxidant effects, which needs to be addressed by precise delivery of the agent to cancer cells.

Finally, we examined the selectivity and sensitivity of highly fluorescent N,B-CNDs as an optical probe for the detection of $Fe^{2+}$ in water samples. We also looked at the bioimaging capabilities of these CNDs for $Fe^{2+}$ detection in living cells. With the addition of iron ions, the fluorescence intensity of the CNDs diminishes in a concentration-dependent way, which can be attributed to the charge transfer between the CNDs and $Fe^{2+}$, as confirmed by electrochemical testing and band-gap energy analysis. Therefore, these CNDs could serve as effective "Turn–Off" fluorescence-based probes for $Fe^{2+}$ detection.

Overall, the findings from this dissertation work pave a way to understanding the underlying mechanisms of heteroatom doping effects on tuning the structural and optoelectronic features of CNDs, and their contribution to oxidative stress-related disorders at cellular level.

# INVESTIGATION OF OPTOELECTRONIC PROPERTIES AND ABTI/PRO-OXIDATION EFFECTS OF CARBON NANODOTS (CNDS) DOPED WITH DIFFERENT HETEROATOMS

by

Mahsa Azami

A Dissertation
Submitted to
the Faculty of The Graduate School at
The University of North Carolina at Greensboro
in Partial Fulfillment
of the Requirements for the Degree
Doctor of Philosophy

Greensboro

2023

Approved by

Dr. Jianjun Wei
Committee Chair

# DEDICATION

I would like to express my heartfelt gratitude to my parents, who have been a constant source of support and inspiration throughout my life. I also would like to thank my brother and sister for believing in me, fighting for me, and being the impetus behind my accomplishments. Thank you, Mom and Dad, Saeed, and Saba for everything.

I would like to express my deepest appreciation to my husband, Mehrab, for his unwavering love, support, and encouragement throughout my Ph.D. journey. His patience, understanding, and commitment have been a source of strength and inspiration, and I am forever grateful for his presence in my life. I could not have achieved this significant milestone without him.

I dedicate this dissertation to all those who helped me throughout my education, specially my family. May this recognition serve as a token of my appreciation for all they have done for me and as a symbol of their invaluable contribution to my academic success.

Thank you all, with love.

APPROVAL PAGE

This dissertation written by Mahsa Azami has been approved by the following committee of the Faculty of The Graduate School at The University of North Carolina at Greensboro.

| | |
|---|---|
| Committee Chair | Dr. Jianjun Wei |
| Committee Members | Dr. Dennis R. LaJeunesse |
| | Dr. Eric Josephs |
| | Dr. Zhenquan Jia |

March 15, 2023
Date of Acceptance by Committee

March 15, 2023
Date of Final Oral Examination

# ACKNOWLEDGEMENTS

I would like to express my sincere gratitude to my advisor, Dr. Jianjun Wei, for his support, guidance, and mentorship throughout my Ph.D. journey. His expertise, insights, and constructive feedback have been instrumental in shaping my research and helping me achieve this significant milestone in my academic career. His dedication to his students and his field is truly remarkable, and I am honored to have the privilege of working with him.

There are also a number of wonderful folks who have inspired me during my graduate studies, namely, Mahboobeh, Anitha, Olubunmi, Afsaneh, Mehrnoosh, Frank, Anu, Mengxin, training staff of JSNN, and many others. Each of them pushed my thinking and helped me improve my research with their invaluable contributions, insightful comments, and suggestions throughout this process.

TABLE OF CONTENTS

LIST OF TABLES

LIST OF FIGURES

LIST OF ILLUSTRATIONS

# CHAPTER I: INTRODUCTION

CNDs are zero-dimensional carbon nanomaterials, which were synthesized for the first time in 2006. Most CNDs are smaller than 10 nm. Specific properties of CNDs simplify their implementation in biomedical applications. Based on nuclear magnetic resonance measurement results, the hybridization of carbon on the inner sides is $sp^2$, while the carbons on the outer sides have $sp^3$ hybridization. Overall, CNDs possess advantages such as high Fluorescence emission, high water solubility, biocompatibility, tunable emission, and resistance to photobleaching [1]–[7].

## Precursors and Synthesis Methods

It is feasible to produce CNDs from a wide range of chemical or natural resources. The carbon content in the precursor influences the final percentage yield of CNDs production, effectively [8]. A wide range of carbon sources have been used as precursors, such as L-ascorbic acid (AA) [9], polyethyleneimine [10], and citric acid [11], as chemical sources, and apple seeds [12], Citrus lemon peels [13], cotton [14], coriander leaves [15], carrot [16] as natural sources. While chemical precursors provide CNDs with higher quantum yield, natural precursors will lead to more biocompatible and less toxic CNDs [17]. In general, two main procedures, including top-down and bottom-up approaches, are available for the synthesis of CNDs [18]–[20].

## CNDs Photoluminescence Properties

One of the optical properties of CNDs is their capability of absorbing UV light region (200-400 nm) generally attributed to n–π* transmission of C=O bonds and some extensions in the visible area related to π–π* transition of the aromatic C=C. However, the most attractive optical feature of CNDs is their Fluorescence properties [21]. Regarding their distinguished structure, CNDs

exhibit strong fluorescent properties, unlike carbon molecules which demonstrate weak fluorescent activities. The carbonic core and surface functionalization of CNDs contribute to the photoluminescence features of CNDs. The core-related electrochemical properties are a result of the $sp^2$ hybridization of carbon in these structures, like nanocrystalline graphite. Also, the functionalization of CNDs has a significant effect on CNDs' optical properties [3], [22], [23]. Doping with heteroatoms is one of the important parameters that can highly affect the photoluminescence features of CNDs, leading to synthesizing more favorable CNDs regarding specific applications. For doping purposes of CNDs, the elements located close to carbon in the periodic table, such as Nitrogen (N), Sulfur(S), Phosphorus (P), and Boron (B), are mostly brought into play. N-containing functional groups are the most utilized ones among other functional groups, which have been used to reach a higher Fluorescence intensity and quantum yield for CNDs [7]. Adding each of these heteroatoms can conflict with the original structure of CNDs in different ways. For example, Adding P to CNDs will generate n-type CNDs with excess electrons in their structure, while doping CNDs with B will provide p-type CNDs with excess holes in the structure [24], [25].

**Radical Scavenging Capabilities of Heteroatom-doped CND in Cells**

It has been shown that CNDs can be employed in various biomedical applications. Significant Fluorescence emission, small size, and antioxidant abilities introduce CNDs as ideal drug/gene carriers, imaging tools, or even independent drugs in biomedicine [26]. CNDs have shown considerable antioxidant features in chemical and biological environments. As antioxidant moieties [27], CNDs have the capability of scavenging various oxidant free radicals produced during several processes in cells [28]. Regarding previous studies, a dual behavior of CNDs is observed in terms of their biological performance inside the cells, attributed to different functional

groups and electrical charges implied on CNDs' surfaces [5], [6]. This difference suggests the unclear effect of elemental atoms on changing the CNDs' ability to induce or scavenge intracellular ROS generations. The generation of ROS is a part of the cell's natural cycle, and many mechanisms have evolved to regulate the extra amounts of generated ROS. However, in many diseases such as cancers, autoimmune diseases, neurodegenerative defects, and cardiovascular or inflammation problems, overproduction of ROS is one of the original hallmarks. Breaking the balance of ROS levels in cells will start a chain of redox reactions and cause severe modifications in the cells' vital biomolecules, defunctionalizing them.

Regarding functionalization and doping, the oxidative stress effects of CNDs have been investigated in numerous cell lines in many studies. This influence could take place in the shape of anti- or pro-oxidant properties, for which numerous applications have been developed.

In a study, EA. hy926 and A549 cells have been treated with N, S-doped CNDs to evaluate the antioxidant effect of as-prepared CNDs on two different cell lines. In contrast with N-doped CNDs, which have shown antioxidant properties in the same cells and with the same concentration [29], N, S-doped CNDs demonstrated oxidative stress in both mentioned cell lines, despite their antioxidant potential in the physicochemical environment [30]. In a photodynamic study, CNDs and NIR irradiation have been used as killing agents for U251MG cells. N, CNDs have been prepared from ethylenediaminetetraacetic acid (EDTA) as a direct source of Nitrogen by a single-step hydrothermal method. After exposure cells to N, CNDs, and NIR irradiation simultaneously, the generation of peroxide and superoxide radicals ($O_2^{-}$°) was inquired by the calorimetric method. As a result, ROS generation was detected upon incubation of the cells with N, and CNDs, and was induced upon the addition of NIR irradiation [31]. The ROS generation activity of N, CNDs is attributed to their electron donation properties. N, P-doped CNDs represented a multifunctional

anticancer activity in a study while B16F10 melanoma cancer cells have been exposed to them. Several involved simultaneous pathways were introduced to this multifunctional anticancer activity of as-prepared N, P doped CNDs, mainly based on ROS production in cells [32]. However, in some other studies, N, P doped CNDs have been safely used for cell imaging and measurement of ROS levels inside RAW264.7 cells [33], also for detection of $Fe^{3+}$ ion in human serum and living (T24) cells [34].

Furthermore, speaking of dopant elements, P and B have been used in CNDs' synthesis, making them antibacterial agents, cellular imaging, and detection probes for different metal ions. However, the anti/pro-oxidant effects of these CNDs in the chemical environment and cells have poorly been studied. CNDs utilization as novel nanodrugs toward a specific sub-cellular organelle is a promising treatment for many diseases.

In a few studies, the effect of CNDs with different functionalities has been studied on the oxidative stress-related gene expression levels in cells. For example, an upregulation of the superoxide dismutase gene was detected after CNDs treatment which confirmed the ROS scavenging ability of Fe-CNDs [35]. In another work, a regulated cell death gene expression was studied after the treatment of breast cancer cells with a special type of CNDs which along with photothermal therapy was used for induced apoptosis in cancer cells [36]. Based on what was discussed above, CNDs have demonstrated significant potential for the up/down-regulation of several genes, particularly those related to oxidative stress, which is crucial for the treatment of a wide variety of disorders.

As a fascinating attribute, the sensing ability of CNDs toward a range of materials has also been intensively researched. Many doped CNDs have been introduced as selective and sensitive On/Off sensors, especially for the detection of metal ions [37], [38]. This sensing capability could

be used along with the imaging ability of these CNDs in living cells as well [6]. As an important metal ion in water and in the body, Fe ions sensing using CNDs have been widely studied, but most research is devoted to $Fe^{3+}$. Only a few numbers of studies in the literature have reported the sensing ability of CNDs toward $Fe^{2+}$ [39], which are even combined with $Fe^{3+}$ detection, non-selectively [40]. This inspired us to evaluate the potential capability of our highly fluorescent N, B-doped CNDs for the detection of $Fe^{2+}$ in water samples and live cells.

Overall, per the recent prominent inconsistency discussed above, it appears that the effect of heteroatom doping of CNDs on their oxidative biological performance needs to be further investigated. This effect could be studied deeply in optical properties, oxidative stress effects, cellular behaviors, and even at gene levels. Finally, precise assessments are necessary to result in the best structural design for CNDs, safe for medical applications. In this study, our goal is to improve our knowledge of how these two heteroatoms - P as an element possessing more electrons than carbon, and B as an element containing fewer electrons than carbon- affect the oxidative stress features of CNDs, as well as their entrance pathway and subcellular localization.

# CHAPTER II: A REVIEW ON THE CELLULAR UPTAKE, SUB-CELLULAR LOCALIZATION, CYTOTOXICITY, AND OXIDATE STRESS EFFECTS OF CARBON NANODOTS IN CELLS

## Overview

Carbon nanodots (CNDs) are a class of carbon-based nanomaterials that have garnered considerable attention in the scientific community due to their unique physicochemical properties and potential applications in various fields. CNDs are typically synthesized using inexpensive and straightforward methods, and they possess excellent biocompatibility, low toxicity, and high-water solubility, making them highly versatile and promising candidates for biomedical applications. Moreover, their small size and inherent fluorescence properties make them ideal for biological imaging and diagnostics. However, the safe and effective use of CNDs in biomedical applications requires a thorough understanding of their cellular uptake, subcellular localization, and cytotoxicity. In this review, we provide a comprehensive overview of the current knowledge on these topics, including the factors that affect CND uptake and subcellular localization. We also discuss the factors that influence CND cytotoxicity, such as particle size, surface charge, and functionalization, and highlight the mechanisms by which CNDs can induce oxidative stress in cells. Overall, this review provides a critical analysis of the current state of knowledge on CNDs in cellular systems and highlights the potential of these nanomaterials for future biomedical applications.

## Introduction

As a novel class of spherical nanomaterials, CNDs were introduced in 2004 as a byproduct of purifying and separating single-wall carbon nanotubes [26]. Based on nuclear magnetic resonance measurement results, the hybridization of carbon of the inner sides is $SP^2$, while the outer sides have $SP^3$ hybridization [41]. CNDs offer superior benefits namely water solubility, biocompatibility, tunable emission, and resistance to photobleaching [2]. These properties enable their implementation in biological applications, as opposed to their counterparts, quantum dots, which have been found highly toxic [7]. Furthermore, functional groups containing hydrogen (such as hydroxyl and carboxylic acid) on CNDs allow easier functionalization with other organic groups. Given all of the previously stated characteristics of CNDs, it is thought that these entities have the potential to introduce novel opportunities for a range of therapies in the future. [1], [4]–[6].

A wide range of natural and chemical sources have been used for the synthesis of CNDs [17]. Generally, the functional groups and surface charge of CNDs dictate their chemical and biological characteristics. For example, functionalization with amino groups simplifies the subsequent modifications of CNDs [10]. Although it has been reported that even pristine CNDs could enter the cells and have some functionalities, in general, it is believed that pristine CNDs are challenging to monitor given the limited recognition groups on their surface. Additionally, unfunctionalized CNDs encompass lower quantum yields with limited capabilities to be used as probes in biological systems [42]. The ability to conjugate with various heteroatoms and functional groups furnishes CNDs as great tools for targeting diverse biomarkers [43].

In general, CNDs synthesis is usually carried out through two main procedures including top-down (such as arc-discharge method, laser ablation, electrochemical approach, chemical

exfoliation method, etc.) and bottom-up (such as thermal pyrolysis approach, hydrothermal method, microwave heating method, anchor/support-based approach, and template-based metal organic framework) methods [44]. Bottom-up approaches, which include oxidation of carbon sources, are likely low-cost and easier to handle because of the simplicity of the procedure, while these benefits may not apply to top-down approaches [18]–[20]. Template-based synthesis methods have also been suggested for the preparation of CNDs [45]. In this approach, CNDs confine in a hosting template such as silica nanorods [46], zeolite crystals [47], Covalent organic frameworks (COFs) [48], etc.

So far, myriads of applications for CNDs have been reported including their application as catalysts [49]–[51], bio-imaging agents [52]–[55], bactericidal agents [56], [57] drug carriers [5], [58], [59], targeting and antioxidant agents [27], and theragnostic agents [23], [60]. The earliest record on CNDs indexed by the Web of Science Core Collection (WoS) was published in 2006: "Direct immobilization of DNA on diamond-like carbon nanodots" [61]. It was only in 2018 that WoS indexed more than 1000 original research papers, where the number reached 1442 and 1460 in 2020 and 2021, respectively. The 2902 research manuscripts during these two years were analyzed bibliometrically applying VOSveiwer [62] for the 100 most-mentioned keywords (Illustration 1). In this scheme, the size of each circle/font is determined by the occurrence of that keyword, and thicker lines demonstrate a higher frequency of co-occurrence of the subjective pairs. Additionally, the items apart from each other have rarely co-occurred in the same articles.

This analysis identified three major clusters of research. The green cluster with 31 keywords focuses on the CNDs-affected metabolism of different cells as well as their pharmaceutics and diagnostics. The blue cluster with 22 keywords specifically looks at the fluorescence properties of CNDs. This keyword possesses the highest occurrence in bibliometric

analysis, indicating its key role in incorporating CNDs in different applications. The biggest chunk of this illustration is in the red cluster with 47 items that involves almost all non-biological applications of CNDs including inorganics, different other types of dots, as well as their physical properties and analysis techniques. Given the highest abundance of the keywords in this cluster, this analysis clearly shows that the CNDs are greatly intertwined in both the *in vivo* and the inorganic systems leveraging the use of different instruments for both systems.

**Illustration 1. VOSviewer Bibliometric Map of the 100 Most Frequent Keywords from 2902 Articles Published During 2020-2021 [63]. The Smallest Circle Represents 25 Articles that Mention the Keyword and the Size Correlates with the Number of Articles. Keywords with the Same Color Occur More Frequently in the Same Article. Lines from One Circle to Another Relate to Co-Citations Between the Articles. The Largest Cluster is the Red Cluster with 47 Keywords, Whereas the Most Abundant Keyword is Fluorescence in the Blue Cluster Which Has 22 Keywords. The Green Cluster hat Mainly Discusses Recent Studies on Different Tissues has 31 Keywords with the Highest Co-Citations.**

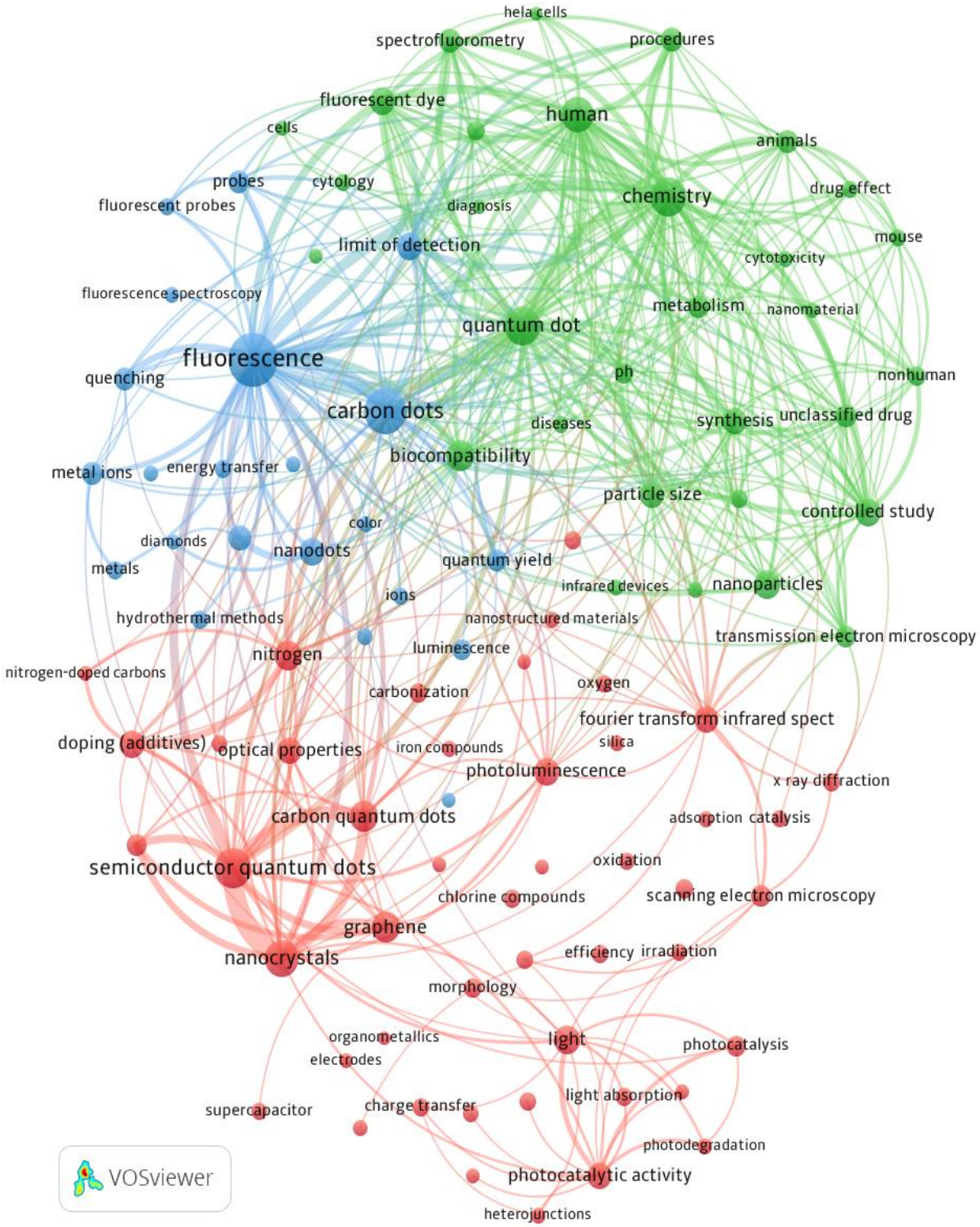
hela cells
spectrofluorometry
procedures
fluorescent dye
human
cells
animals
probes
cytology
chemistry
drug effect
fluorescent probes
diagnosis
mouse
limit of detection
cytotoxicity
fluorescence spectroscopy
metabolism
nanomaterial
quantum dot
fluorescence
quenching
ph
nonhuman
carbon dots
diseases
synthesis
unclassified drug
biocompatibility
metal ions
energy transfer
particle size
controlled study
color
diamonds
nanodots
quantum yield
metals
infrared devices
nanoparticles
ions
hydrothermal methods
nanostructured materials
transmission electron microscopy
nitrogen
luminescence
nitrogen-doped carbons
oxygen
carbonization
fourier transform infrared spect
doping (additives)
optical properties
iron compounds
silica
photoluminescence
x ray diffraction
carbon quantum dots
adsorption
catalysis
semiconductor quantum dots
oxidation
chlorine compounds
scanning electron microscopy
graphene
nanocrystals
efficiency
irradiation
morphology
organometallics
light
photocatalysis
electrodes
light absorption
supercapacitor
charge transfer
photodegradation
photocatalytic activity
heterojunctions
VOSviewer

## Cellular Uptake Mechanisms of CNDs

Cellular uptake includes the interplay between the nanoparticles (NPLs) and cell membrane which is accomplished via various pathways including active and passive transports [64], [65]. NPL entry to the cell can be carried out via several mechanisms (Figure 1) such as clathrin-mediated endocytosis, caveolae-mediated endocytosis, clathrin/caveolae- independent endocytosis, macropinocytosis, fast endophilin-mediated endocytosis, passive transport, etc. [66], [67]. It has also been reported that different cell types such as intestinal epithelial cells, pulmonary epithelial cells, renal tubular epithelial cells, etc. interact differently in response to the entrance of NPLs [68]. The adsorption of CNDs with an average size of 3.8 nm and zeta potential of -22.3±1.7 mV on the surface of NIH3T3 and MCF-7 cell lines was investigated using liposomes as cell membrane simulators [69]. The results showed that hyperpolarized cells attract more CNDs on their surface compared to both depolarized and polarized cells. This attachment was found to be affiliated with the cell trans-membrane potential.

The cellular uptake of CNDs in turn is determined by employed precursors, size distribution, morphological structure, surface charge, and functional groups [70], [71]. Functionalizing CNDs promotes their sensitivity and selectivity to attach to specific cells [72]. For example, the CNDs functionalized with folate receptors with an average size of 4nm were significantly more prone to Hela cancer cells rather than folate receptor (FR)-negative MCF-7 cells [73].

CNDs identical in functional groups but different in the local density of the functional groups can be wrapped differently by different serum proteins around the cells upon the cellular uptake [74]. Three types of CNDs with different chirality were synthesized and their cellular uptake was investigated using confocal microscopy and flow cytometry. Then the effect of

adsorption of three different serum proteins (human serum albumin (HSA), alpha microglobulin, and transferrin) on the cellular uptake of CNDs was monitored by measuring the protein concentration-dependent CNDs size changes. Since each CNDs possessed a different local density of the functional groups on the surface, the protein binding to these CNDs (which is quantified by measuring $K_D$ values), was finally different. Li et al. (2018) synthesized two different types of CNDs with positive and negative surface charges [75]. They have studied the effect of CND's surface charge on their HSA protein binding. The results showed that the intrinsic fluorescence of HSA is being quenched by both CNDs almost similarly, regardless of their charge. However, these CNDs showed different concentration-dependent effects in terms of changing the HSA secondary structure. Also, positively charged CNDs association was shown to occur dominantly via electrostatic forces, while negatively charged CNDs occurred via hydrophobic and van der Waals forces.

In many studies, the cellular uptake pattern on CNDs has been followed using various types of endocytic pathway blockers. Also, the outstanding fluorescence characteristics of CNDs facilitate their cellular uptake pathway to follow. To investigate the cellular uptake mechanisms of N-doped CNDs, Ji et al. (2020) synthesized CNDs with an average size of 2.4 nm and zeta potential of −36 ±3 mV, employing NaN3 as an endocytic pathway blocker [76]. They concluded that the cellular uptake of N-doped CNDs in both EA.hy 926 cells and A549 cells follow a temperature- and ATP-dependent pattern. Another type of CNDs was synthesized from citric acid and polyethyleneimine with an average size of 10.84 nm and zeta potential of +29.6 mV, and their cellular uptake mechanism was studied in ACC-2 cells [77]. These CNDs showed an energy-dependent cellular uptake via macropinocytosis endocytosis, which is in agreement with similar studies. Functionalizing folate ligands has created CNDs capable of binding to cancer cells with

overexpressed folate receptors on their surface. Figure 1 illustrates the different proposed pathways for CNDs' internalization to the cells.

**Figure 1: Various Proposed Endocytosis Patterns of CNDs [76].**

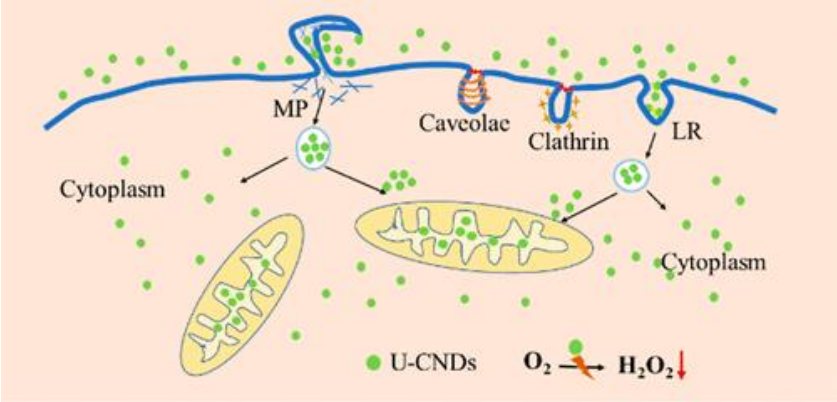


MP: Macropinocytosis Caveolae: Caveolae-mediated endocytosis
LR: Lipid raft-mediated endocytosis Clathrin: clathrin-mediated endocytosis

For a successful application of CNDs as drug carriers, or live cell imaging tools, it is necessary to evaluate optimized CNDs' concentrations while being incubated with cells. In a study, the effect of N, doped CNDs concentration and incubation time in the cellular uptake and more specifically, in the nuclear permeability of A549 cells were investigated using confocal microscopy. The light signals reflected by CNDs quantitatively determine that there is a concentration-dependent pattern of cellular uptake for these CNDs [78].

### Sub-cellular Localization of CNDs

One of the most critical biological features of NPLs is their distribution pattern in cells [79]. Not only targeting specific cells but also targeting specific subcellular organelles is taking into consideration recently to gain the most desirable biological benefits of different CNDs. As a powerful tool in many biological applications, the localization of CNDs inside the cells has been the focal point in literature. It has been shown that CNDs could distribute in various organelles in the cells [66]. Several types of CNDs have been applied in targeting different organelles including

the nucleus, mitochondria, lysosomes, endoplasmic reticulum, Golgi apparatus, and cytoplasm [80]. Functional groups are powerful tools that can boost the sub-cell organelle targeting of CNDs. Amino groups, mitochondrial targeting peptides, and sulfhydryl groups have been reported as functional groups which boosted the lysosome, mitochondria, and Golgi apparatus targeting of CNDs, respectively [81]. In a study, the uptake mechanism of CNDs synthesized from soybean oil was investigated and their accumulation loci in the MCF-7 cells as a function of treatment time duration was followed [82]. Since the prepared CNDs were functionalized with fatty acid groups, they accumulated on the cell surface after 5 minutes of incubation. Treatment of the cells with CNDs for 1 hour led to the accumulation in the cytoplasm. The effect of CNDs' surface charge in their sub-cellular localization is very important [75].

**Table 1. Different Synthesized CNDs Along with their Sub-Cellular Organelles Targeting Capabilities.**

| Precursor | Functional groups/ surface modification agents | Size (nm) | Zeta-potentials (mV) | Cell line | Targeted organelle | Ref. |
|---|---|---|---|---|---|---|
| Glucose, PEG | OH | 60.3 ± 7.0 | −12_8±1_0 | 16HBE | Cell Membrane | [83] |
| L-cysteine, EDA, Ruthenium chloride hydrate | Ru | 80 nm | 1.5 ± 0.4 | – | Lysosome | [84] |
| Garlic | -OH, -COOH | 3-5 | – | Macrophages | Cytoplasm | [85] |
| Melanin | N/ iRGD | 3.3 ± 0.57 | positive | | Nuclei | [86] |
| Urea, citric acid | PEG, Biotin | – | – | MDA-MB-231 | Nuclei | [87] |
| Urea, citric acid | PEG, Biotin | – | – | MCF7 | Cytosol inside endosomes | [87] |
| Citric acid, dicyandiamide | MLS, RGD | 10-30 | -6.41 | HepG2 (liver cancer cells) | Mitochondria | [88] |
| 1,2,4-triaminobenzene dihydrochloride | N/ CCA, TPP | 2.5 | +19.6 | RAW264.7 cells | Mitochondria | [89] |

| | | | | | | |
|---|---|---|---|---|---|---|
| Citric acid, ethylenediamine | Amine-based groups | 1-5 | +2.3 | PC12 and RSC96 | Golgi apparatus (major) Nucleus (minor) | [90] |
| Coriander leaves | C, N, O | 2.38 | −24.9 | A549 and L-132 cells | Cytoplasm | [91] |
| Metformin | C, N, O | 6–7 | +0.45 | Hek-293 cells, sea urchin animal model, SJGBM-2 cell | Mitochondria of cancer cells | [92] |
| Citric acid and EDA, modified with mitochondria targeting agent | Carboxyl and amino, modified with triphenyl-phosphonium | 4.5 | – | HeLa, HepG2, and A549 cells | Mitochondria | [93] |
| Citric acid, Au | – | 48 | –18.9 ± 2.1 | HUVEC | Cytoplasm | [94] |

In a study, it has been shown that in healthy cells, because of the highly negative mitochondria membrane potential (MMP) which is about −150 to −180 mV, the positively charged CNDs presented a high affinity to migrate to mitochondria [95]. This affinity decreased by manipulating the MMP and reserved when MMP levels were retained at their original value. Table 1 summarizes the information about different synthesized CNDs along with their sub-cellular organelles targeting capabilities.

**Cytotoxicity of CNDs**

So far, so many mechanisms have been carried out and proposed for the cytotoxicity of nanomaterials including CNDs [96], [97]. The chemical properties of the functional groups as well as the quantity of surface charge that these groups apply to the CNDs are the two key factors in defining their biological behavior while exposed to the living cells. While in many studies it has been proven that CNDs demonstrate no disruptive effects on healthy cells, in some cases, these species behave as cytotoxic agents at some concentration levels. CNDs enriched with OH groups on the surface, derived from Glucose and PEG was synthesized and exposed to human bronchial epithelial (16HBE) cells to evaluate their cytotoxicity effects [83]. These CNDs showed increasing cytotoxicity in the cells which was measured by lactate dehydrogenase (LDH) as a sign of cell membrane injury. This could happen because of the ultrasmall size of CNDs which leads to the penetration of CNDs into the cell membrane. Here, the DCFH-DA test showed the same results for the cytotoxicity of as-prepared CNDs. In contrast with these results, wool-derived N-doped CNDs presented a slight cytotoxic effect (more than 86% viability) at the concentration of 0.3 mg/ml toward Hela cells [98]. The preparation of Ionic liquid-modified CNDs (IL-CNDs) has been reported as a method to improve the biocompatibility of CNDs [99]. CNDs were derived from Glucosamine and functionalized with amide groups. Finally, using ionic liquid 1-carboxymethyl-

3-methyl imidazolium bromide, IL-CNDs were prepared via covalent conjunctions. The viability of Hela cells incubated with these CNDs remained at nearly 75% at the high concentration of 10 mg/ml, while the viability of the same cells dropped to 50% after the exposure to amide-CNDs as a control even at the concentration of 4 mg/ml. In another study, three differently charged groups of CNDs were synthesized and their cytotoxicity was investigated [72]. Based on the results of this study, neutral CNDs were the best option for being used in biomedical applications since they did not induce any abnormalities in cell morphology. The negatively charged CNDs showed some cytotoxic effects such as stimulating the proliferation and leading to higher oxidative stress although they have not entered the nuclei, whereas the positively charged CNDs entered the nucleus causing significant cytotoxicity effects on the G0/G1 cell cycle, even at low concentrations.

In terms of the precursors used for the synthesis, it is believed that natural precursors-originated CNDs as well as negatively charged CNDs, might cause less cytotoxicity in the body [66]. The anti-cancer therapeutic effect of asparagus roots-derived CNDs was analyzed against breast (MDA-MB-231) and cervical (SiHa) cancer cells [100]. Meanwhile, their cytotoxicity effects were analyzed by evaluating the histological parameters in different organs of Swiss albino mice. The results did not show any marks of cytotoxicity resulting from the mentioned CNDs. Similarly, in a study by Sachdev et al, the cytotoxicity of CNDs synthesized from coriander leaves in two different types of cells was investigated [91]. The exposure of A549 and L-132 cells to varying doses of CDs had no significant cytotoxic impact.

The most successful synthesized CNDs seem to be those showing toxicity in malignant cells, while still safe in healthy cells. Previously, it has been shown that the amount of superoxide or hydrogen peroxide generation in cells, depends on the concentration of electron donor substrate

in the cells' microenvironment and not on the respiration chain rate [101]. This is the main reason that the optimization of treated CNDs concentration is needed as well. Depending on each specific concentration, different levels of cytotoxicity have been observed. On the other hand, it has been shown that positively charged CNDs while used as probes, enter the cell's nucleus and cause cytotoxicity effects even in small concentrations [97]. It can be concluded that the carbon dots with more selectivity toward the cytoplasmic localization have less likelihood of toxic effects/mutagenicity in cells [3]. Nevertheless, the toxicity of CNDs is still a controversial issue. Although CNDs seem to have less toxicity in living cells in comparison with QDs, still some limited toxicity is considered for these carbon-based nanostructures [7].

**Oxidative Stress Effects of CNDs**

One of the most reported effects of CNDs in cells is their contribution to the oxidative stress pathways [102]. Reactive oxygen species (ROS) are referred to the chemical species resulting from the incomplete reduction of oxygen, such as hydroxyl radical ($OH^{\bullet}$), superoxide anion ($O_2^{\bullet-}$), and even a non-radical molecule such as hydrogen peroxide ($H_2O_2$) [103]. ROS, at low or moderate levels, plays a vital role in various cell activities such as growth, signaling homeostasis, and apoptosis [104]. In other words, there is a balance between the generation of ROS species in the cell and scavenging species such as enzymes or antioxidants. For instance, $O_2^{\bullet-}$ which is a necessary agent in a limited amount for muscle's proper functioning, is disruptive in higher levels [103], [105], [106]. This complicated behavior of ROS makes their biological role very difficult to interpret either in normal or cancerous cells [105]. It is believed that in cancer development, ROS demonstrates a dual role. Their role in tumor generation in cells is via many stages of tumorigenesis including transformation, cancer cell survival, cancer cell proliferation, and many other steps. Whereas ROS could influence cancer cell apoptosis by interfering with

cancer therapy treatments [107]. Interestingly, each type of ROS source could result in the improvement of different cancers with a different site of action[108]. Regarding the fact that CNDs could highly accumulate in mitochondria, it is expected that CNDs get involved with the electron transport chain (ETC) in mitochondria, hence affecting the oxidative stress in cells [109]. Figure 2 shows how different CNDs could contribute to cells as anti-cancer agents by either reducing or inducing oxidative stress effects. Mitochondria and the nucleus are the most probable locations which are involved with ROS generation in living cells. In mitochondria, the respiration chain produces ROS, and the enzymes accelerating this production are coded in the nucleus [110]. Mitochondria is the known place to generate various ROS sources such as nicotinamide adenine dinucleotide phosphate (NADPH), xanthine oxidase (XO), uncoupling of nitric oxide synthase (NOS) cytochrome P450, and mitochondrial ETC [111]. Also, mitochondria are the most endanger sub-cellular locations concerning ROS. Oxidative stress could cause defections in mitochondrial proteins, lipids, and mtDNA and deactivate these vital materials [109], [112]. However, there are some other sites in cell which contribute to ROS generation such as peroxisomes and endoplasmic Reticulum (ER) [113]. Overall, there are three main pathways in which ROS can contribute to the apoptosis including the mitochondrial pathway, death receptor pathway, and the ER pathway [104].

**Figure 2. Contribution of CNDs in Oxidative Stress in Cells by SOD and CAT Mimicking Mechanism and ROS Scavenging Effects [114] (a), or GSH Depletion and ROS Induction Mechanism [115](b).**

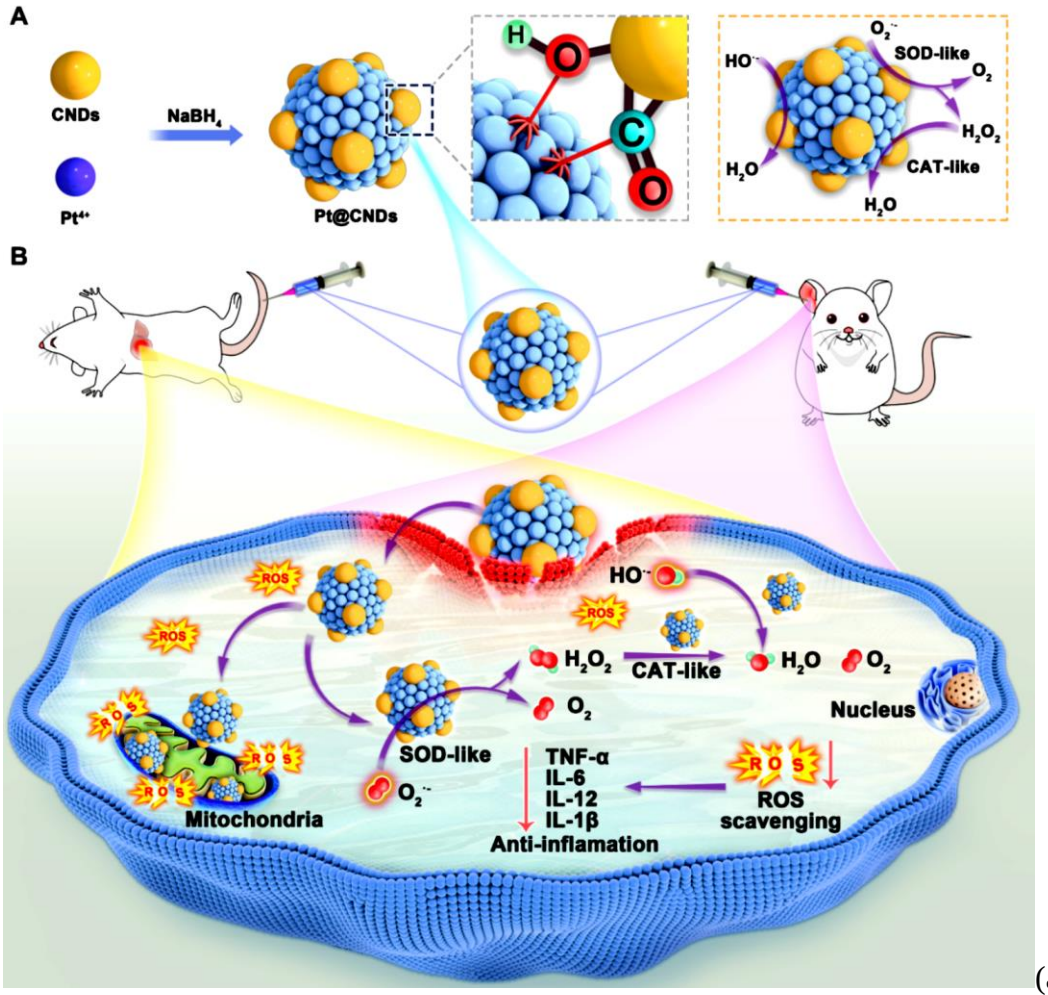


(a)

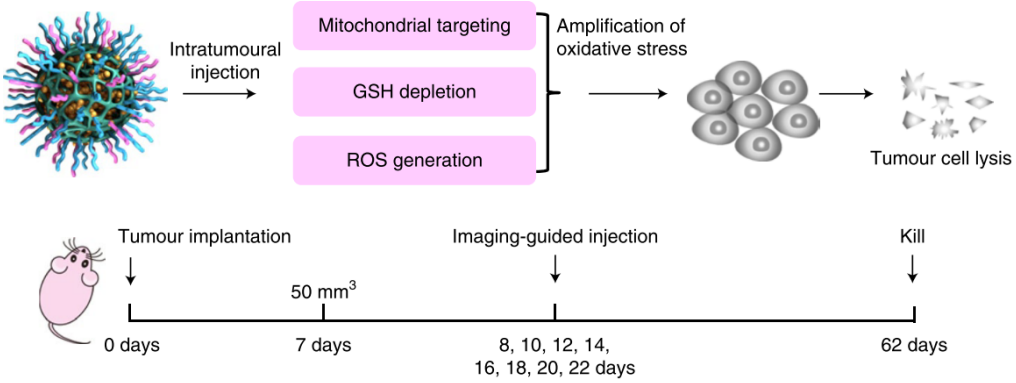


(b)

**Proposed Mechanisms of Anti-oxidation Effects**

CNDs have shown considerable antioxidant features in cells, in some cases even more than ascorbic acid which is known as a highly antioxidant agent [27]. In many studies, researchers have implied CNDs toward cancer cells directly, to evaluate their anti-cancer capabilities [102]. This is due to the scavenging effects CNDs toward various oxidant free radicals that are produced during several processes in cells. Studies show that the antioxidant activity of CNDs highly depends on the surface functional groups on CNDs' surface. These functional groups may include -COOH, amine, sulfide groups, etc. [116], [117]. A type of N-doped CNDs synthesized from sucrose was investigated for the anti-oxidation effects in response to the induced $H_2O_2$ in two different cell types [29]. In both SGC-7901 and GES-1 cells, an increase in cell viability was observed after incubation with $H_2O_2$ upon the addition of CNDs. The observed cell viability was dependent on the concentration of CNDs, as well as the cell type. The authors discussed that since the cellular metabolism is different in normal and cancer cells, their reaction to the induced ROS and anti-oxidation action of CNDs is also different. In another study, CNDs' anti-oxidation capabilities were confirmed via different assays [3]. $KMnO_4$ reduction assay, DCFH-DA assay, NBT assay, and DPPH free radical assay were conducted to evaluate the ROS scavenging ability of the CNDs on MG-63 cells. In all experiments, the EC50 values were calculated and compared with the ones of the reference materials. The comparable results of all experiments proved the high anti-oxidation effect of CNDs. In another study, a lysosome targeting morpholine, Se-doped CND was synthesized, and its ROS scavenging capability was evaluated toward OH radicals both in chemical media and *in vitro* in HeLa cells [118]. A $Fe^{3+}$/ $H_2O_2$ system was used to provide the induced OH radicals. The experiments proved the radical scavenging capability of the as-mentioned CNDs in the wet chemistry environment, also a favorable concentration-dependent

protection capability from oxidative stress effects in cells. CNDs have also been used in conjugated forms with metals to treat cancer cells via involving the oxidative stress in cells. These combinations have shown anti-cancer effects in different ways. A type of integrated CNDs with Pt has exhibited successful SOD- and CAT-like activities due to the synergistic effect of both Pt NPLs and CNDs [114]. This combined system was examined both *in vitro* (in RAW264.7 cells to evaluate their cytotoxicity, their targeting ability toward $H_2O_2$-induced high ROS-containing cells, and their ROS scavenging ability) and in vivo (in tumor-induced mice models). The results indicated the ROS scavenging features of this conjugated system which could successfully target the mitochondria in mentioned cells. Green fluorescent CNDs were synthesized from gynostemma [119]. The viability of embryonic zebrafish was evaluated as above 90% after treatment with CNDs. Also, CNDs' antioxidative stress properties were studied, and the presence of CNDs could enhance the mRNA expression of associated genes, resulting in more antioxidant proteins encoded in zebrafish.

In a study by Yang Li et al, dopamine-based CNDs, dispersing in water and combination with laser irradiation at 808 nm, were used against Hela cells and demonstrated a remarkable capability to kill tumor cells efficiently, which introduces these CNDs as powerful in combination with photothermal therapy for tumor healing [120]. Figure 3. provides a schematic overview of how the common functional groups on CNDs surface can contribute to their radical scavenging mechanisms.

**Figure 3. Proposed Antioxidant Roles and Mechanism of ROS Scavenging by CNDs in HeLa Cells [118] (a), and MG 63 Cells [3] (b).**

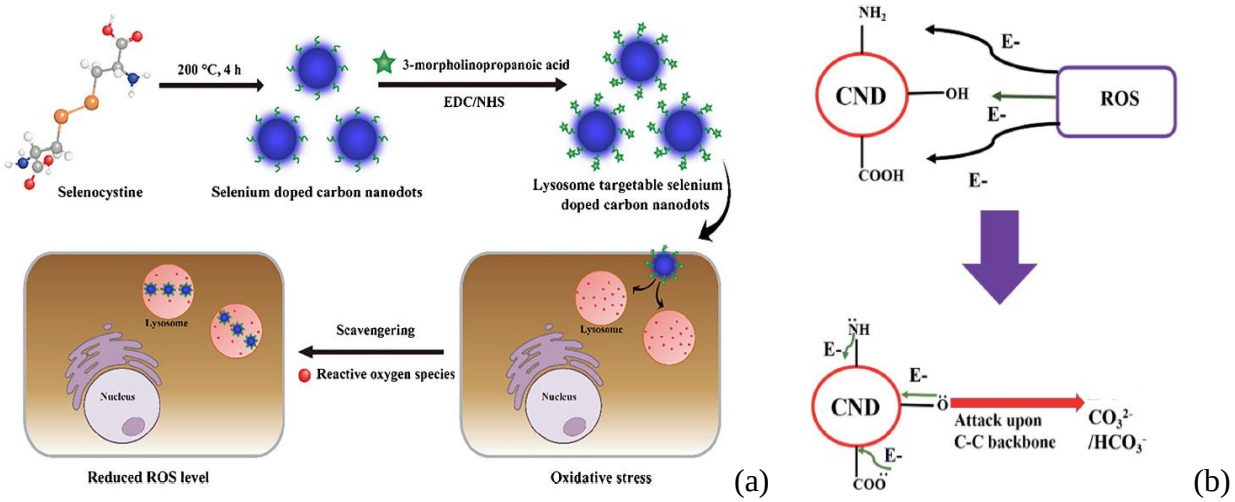


**Proposed Mechanisms of Pro-oxidation Effects**

From another perspective, CNDs have been used for controlled ROS production in cancer cells [121]. In many studies, CNDs have been used along with photothermal conversion techniques to enrich their anticancer properties by increasing the temperature in tumor sites using Near-infrared (NIR) laser irradiation. To target cancer cells with folate receptors, red emissive type CNDs were produced and covalently functionalized with folic acid ligand [122] (Figure 4a). Upon CNDs' cellular uptake, radiation (660 nm) was emitted, which could induce ROS production in cells. This approach was employed as an attempt to benefit from the theragnostic characteristics of the CNDs. In a photodynamic study, N-CNDs and NIR irradiation were used as killing agents for U251MG cells [31]. After exposure, the generation of peroxide and superoxide radicals was followed up using the calorimetric method. As the result, ROS generation was detected upon incubation of the cells with N-CNDs and induced upon the addition of NIR irradiation. As another interesting result, the lower doses of CNDs led to an increase in the population of necrotic cells,

while early apoptosis was observed with the increase in CNDs' concentration. It is discussed that the electron-donating feature of N-CNDs is responsible for their ROS-generating activity. A type of selenium-doped CNDs with mitochondrial targeting ability was prepared using Selenomethionine [123]. These CNDs were functionalized with triphenylphosphonium (TPP). First, $OH^{\bullet}$ and $O_2^{\bullet-}$ were produced through Fenton and an enzymatic reaction, respectively to evaluate the scavenging ability of TPP-SE, CNDs *in vitro*. Then, RAW264.7 and Hela cells have been incubated with these CNDs to follow their antioxidant capability in the presence of $H_2O_2$. Results showed the cytoprotective ability of the mentioned CNDs in these cells against the induced oxidative stress caused by adding $H_2O_2$. OH-doped CNDs were synthesized and exposed to rADSCs cells to evaluate their antioxidant activity [124]. The -OH and C=O content of CNDs were compared by X-ray photoelectron spectroscopy (XPS), before and after the exposure to the cells. The -OH level decreased from 97.93% to 90.96%, while C=O content showed an increase from 2.07% up to 9.04%. This result showed the radical scavenging ability of the OH-CNDs in the cells toward $OH^{\bullet}$ radicals.

**Figure 4. CNDs Covalently Functionalized with Folate and their Ability in Targeted Intracellular ROS Production [122] (a). Anti-Cancer and Photothermal Conversion Ability of CNDs Synthesized from Urea and Citric Acid in Breast Cancer Cell Lines [125] (b).**

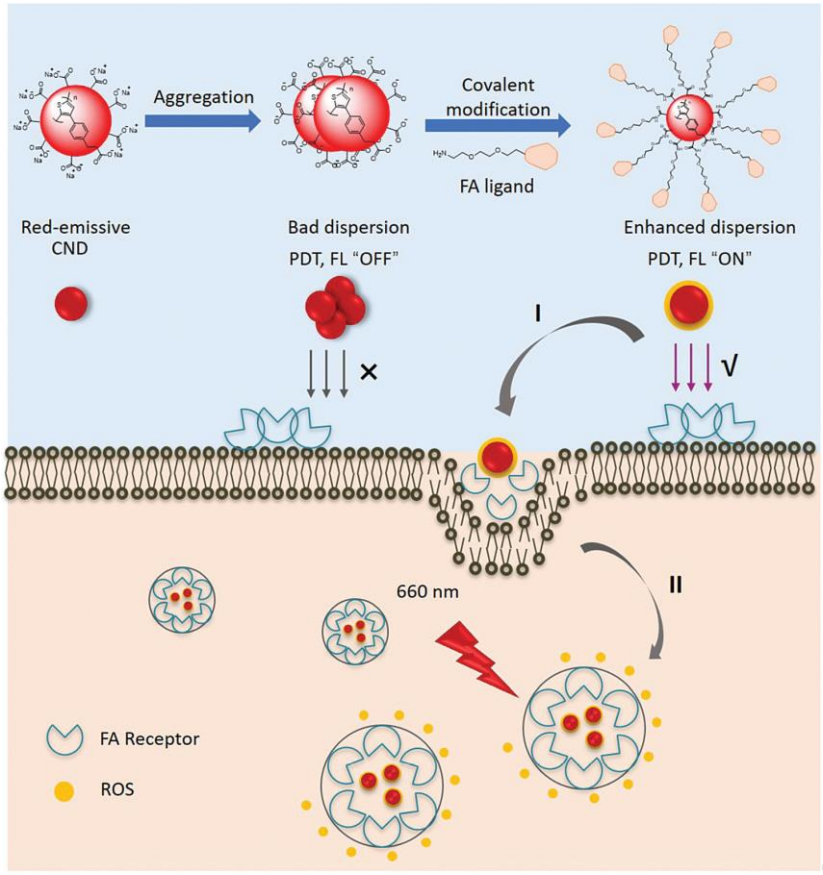


(a)

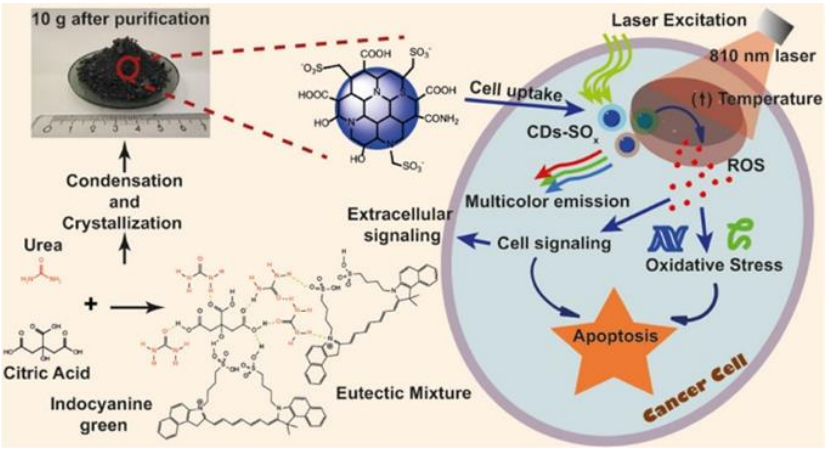


(b)

Mauro et al. synthesized CNDs from urea and citric acid conjugated with indocyanine which grants $SO_x$ functional groups to the CNDs' structure [125] (Figure 4b). They investigated the oxidative stress effects of these CNDs on different human breast cancer cell lines such as MDA-MB-231, MCF-7, and SKBr-3. The photothermal conversion ability of CNDs was also used to help reinforce the anticancer capabilities of CNDs. DCFH-DA was used as a probe to track the ROS production in the mentioned cell lines. As a result, CNDs had significantly higher cellular internalization and ROS production ability in cancer cells compared to healthy cells. Their toxic effect against cancer cells was also enriched by external NIR irradiation. In another study, a conjugation of CNDs with an atomically dispersed gold system was synthesized and examined for anti-cancer effects both *in vitro* and *in vivo* [115]. This combined system could specifically target the mitochondria, and glutathione (GSH) depletion, and serve as an oxidative stress amplifier, resulting in apoptosis in cancer cells as well as in tumor-induced mice models.

**Dual Behavior of CNDs Towards Oxidative Stress in Cells**

Similar to other nanomaterials, CNDs can act as a double edge sword in terms of their contribution to the oxidative stress pathways in cells. In a study, N, S doped CNDs synthesized from pomelo, have shown antioxidant properties toward $O_2^{\bullet-}$, $H_2O_2$, and DPPH radicals in the physicochemical environment [126]. In another study, Ji et al provided a more complete study to have a better understanding of N, S doped CNDs synthesized from urea, citric acid, and lipoic acid in both wet chemistry and cellular environments [30]. The mentioned N, S-doped CNDs demonstrated prooxidant effects in both mentioned cell lines, despite their antioxidant potential in the physicochemical environment. In a study, the prepared CNDs from Gum olibanum showed a dual behavior toward normal and cancer cells (B16F10 and MDA-MB-231, respectively) [127]. Surprisingly, while these CNDs had no cytotoxic effect on normal cells, they showed a significant

ROS induction in the cancer cells under similar conditions which introduce these CNDs as strong prooxidant agents in cancer therapy. In a comparative study, three types of CNDs, doped with N and S, but different in surface charges and functional groups have been synthesized and exposed to alveolar epithelial cells (A549) to evaluate their cytotoxicity, oxidative stress, and proinflammatory cytokines release [128]. The highly positive charged N-CNDs with amine functional groups and the neutral N-CNDs with amide, amino, and carboxylic acid functional groups showed no significant cytotoxicity, while the highly negative charged N, S-CNDs showed a minor decrease in cell viability-which was non-significant toward the positive control. No depletion in GSH was observed with the exposure of three types of CNDs. Also, the as-mentioned CNDs did not induce the release of studied proinflammatory markers such as TNF-α, IL-1β, and IL-8. This shows the effect of sulfur atoms on changing the CNDs features toward inducing intracellular ROS generations. Based on most research results, the low cytotoxicity of CNDs has been proven but there is still the issue of accumulation of CNDs in cells and their resistance to degradation. This accumulation could result in some unexpected metabolisms in living cells which must be taken into consideration seriously in biomedical applications of CNDs [7]. Table 2 provides a summary of the distinct oxidative stress behaviors of CNDs in various cell types, as well as the pathways by which CNDs contribute to these effects.

**Table 2. Different Oxidative Stress-Related Behaviors of CNDs Across Diverse Cell Types.**

| Precursor | Target cells | Observed oxidative stress effect | Proposed mechanism | Ref. |
|---|---|---|---|---|
| Glucose & lysine | HepG2 | Safe at low concentrations/ toxic at high concentrations | Interference of the glycolytic pathway | [129] |
| Green chili | mesenchymal stem cells (MSCs) | Antioxidant | Interacting with the superoxide dismutase (SOD) enzymatic system and enhancing its activity. | [130] |
| NaCl and the metal chelated EDTA | H9c2 cells | Anti-oxidant | SOD and CAT enzymes mimicking | [131] |
| EDTA | U251MG cells | Pro-oxidant | ROS generation in the presence of IR radiation | [31] |
| Chitosan, unsaturated amides /carboxylic acids | Zebrafish | Anti-oxidant | Inhibiting exogenous and endogenous ROS generation | [132] |
| Tris (hydroxymethyl) aminomethane, betaine hydrochloride salt | MCF-7 and HeLa | Pro-oxidant | ROS generation | [133] |
| Candle soot | NIH/3T3 cells | Pro-oxidant | Cell cycle abnormality | [97] |
| Citric acid , EDA | HMEC-1 | Anti-oxidant | Reduction of the expression of pro-inflammatory genes, (IL-8 and IL-1β) | [102] |
| Licorice root extract and $AlCl_3$ | RAW 264.7 | Anti-oxidant | Enhancement the production of TNFα and IL1β cytokines | [134] |

| | | | | |
|---|---|---|---|---|
| Citric acid and EDA , modified with mitochondria targeting agent | HeLa, HepG2, and A549 cells | Pro-oxidant | NO release, changes in mitochondrial membrane potential | [93] |

**Methods for Measuring the Antioxidant Activity of CNDs /Radical Scavenging Assay Methods.**

The antioxidant or prooxidant potential of CNDs is due to their ability to electron and proton transfer with free radicals in cells. Many different methods have been used for the measurement of the anti-oxidation activity of CNDs both *in vitro* and *in vivo* including $KMnO_4$ degradation assay utilizing l-ascorbic acid as control [3], the 2-2-diphenyl-1-picrylhydrazyl radical ($DPPH^{\bullet}$)–based assay based on hydrogen atom transfer (HAT) mechanism [116], [135], and lucigenin chemiluminescence (lucigenin-CL) assay [117]. Dihydroethidium (DHE) also has been used for measuring the $O_2^-$ amounts in cells. On the other hand, Mitochondrial membrane potential ($\Delta\Psi m$) which is associated with more generation of ROS in cells, could also be measured as a signal of ROS existence in cells. Utilizing oxidation-sensitive fluoroprobe (2′,7′-Dichlorofluorescin Diacetate) DCFH-DA is another method for quantification of ROS in cells. DCFH-DA itself has no Fluorescence but the ROS in cells could oxidize that into Dichlorofluorescin (DCF) which is Fluorescent and this Fluorescence intensity can be detected by microplate reader or confocal microscopy [30].

**In-vivo Studies on the Therapeutic Potential of CNDs**

In addition to examining the chemical properties of CNDs, and because the therapeutic potentials of CNDs have been extensively studied *in vitro*, researchers have recently shifted their focus to the therapeutic properties of CNDs *in vivo*. Using *in vivo* models, it has been demonstrated that CNDs are predominantly localized in the lungs and liver and only a few percentages make

their way to other organs such as the brain and heart [136]. It has been shown that CNDs are eliminated from the kidney and liver 8 hours after injection. Also, because the fluorescence of CNDs decreased drastically after a few hours, one could deduce that their metabolism happens within the body [137].

**Cancer**

As discussed earlier, the anticancer capabilities of CNDs are mostly reported to be affiliated with the ROS generation power of these moieties in cells which could affect different sub-cellular organelles, cell signaling, and consequently, the apoptosis of cancer cells. In a study, CNDs with glucose residues on the surface were used against tumors [138]. The idea was that since tumors possess elevated levels of glycolysis, blocking the glucose transporters on their surface will lead to a decrease in access to glucose and cell death. Figure 5a schematically represents the mechanism of inhibiting glucose uptake in tumor cells using the sugar-mediated CNDs. The induced decrease in the energy levels of the cells decreases tumor cells' size and activity, thereby reinforcing the chemotherapy treatments.

In another interesting study, L-arginine-derived CNDs were synthesized which presented the ability to produce NO in tumor cells enriched with $H_2O_2$. While being safe to human normal cell lines (BEAS-2B), these CNDs were able to deeply penetrate the tumor site, absorb $H_2O_2$, and effectively combine with chemotherapeutic drugs and cause cancer cell death (Figure 5b) [139].

**Figure 5. Mechanism of Inhibiting Glucose Uptake in Tumor Cells Using the Sugar-Mediated Carbon Dots (a) [138], and Mechanism of Cancer Cell Death by CNDs Penetrating the Tumors (b) [139].**

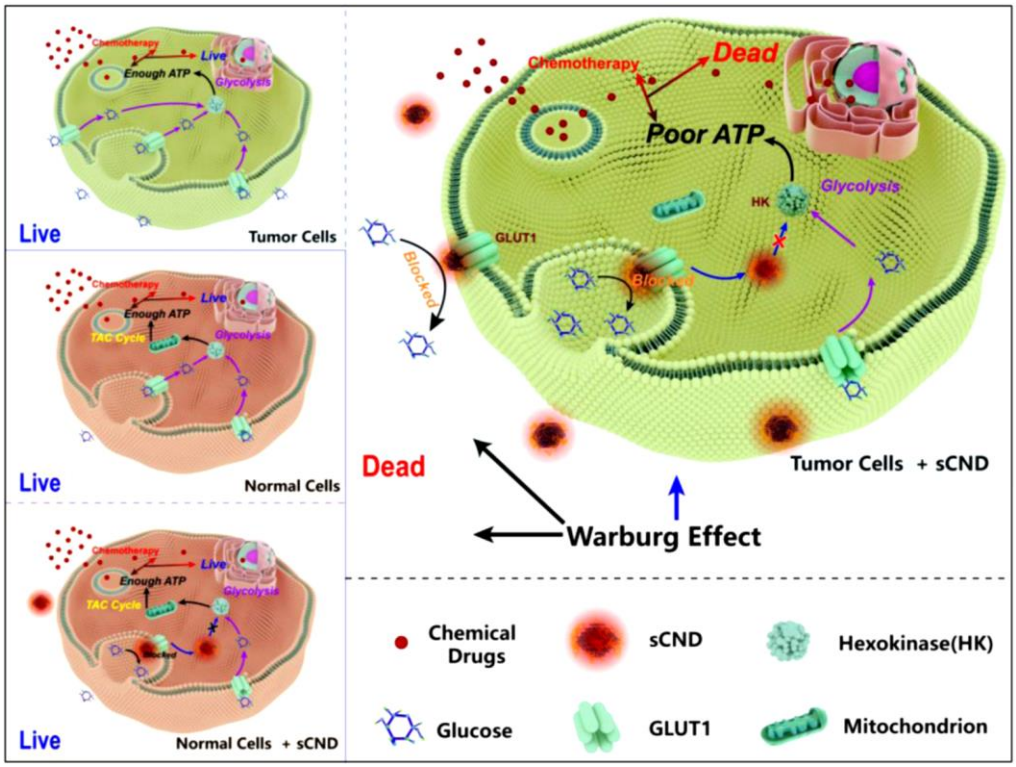


(a)

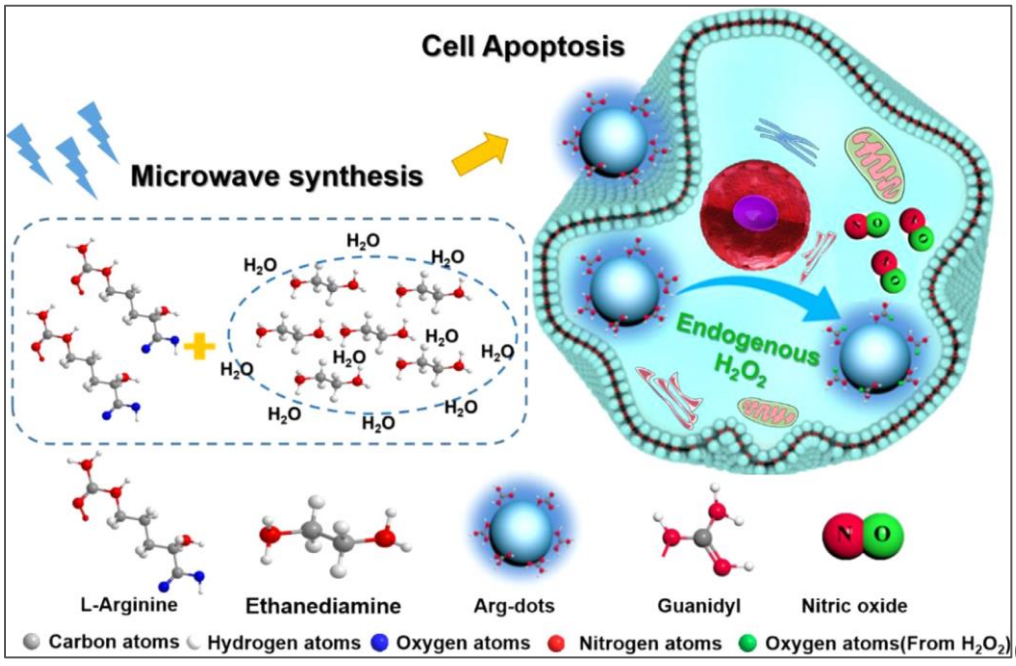


(b)

**Other Inflammatory Diseases**

CNDs have also been considered in the treatment of other diseases associated with elevated ROS levels. Figure 6a represents a study in which N-doped CNDs act as peroxidase (POD)-like, catalase (CAT)-like, and SOD-like moieties highly capable of scavenging free radicals [140]. To investigate the *in vivo* anti-inflammatory characteristics of the CNDs, they have been tail-injected into mice models with liver inflammation. The reduction of ROS production and the proinflammatory cytokines were successfully confirmed. The abovementioned study highlights the vital role of CNDs, as potent radical scavengers, in the prevention of inflammatory diseases in their early stages (Figure 6b).

**Figure 6. POD-Like, CAT-Like, and SOD-Like Activities Lead to Anti-Inflammatory Characteristics of the CNDs [140] (a); and In Vivo Anti-Inflammatory Characteristics of the CNDs After Tail-Injection to Mice Models with Liver Inflammation [118] (b).**

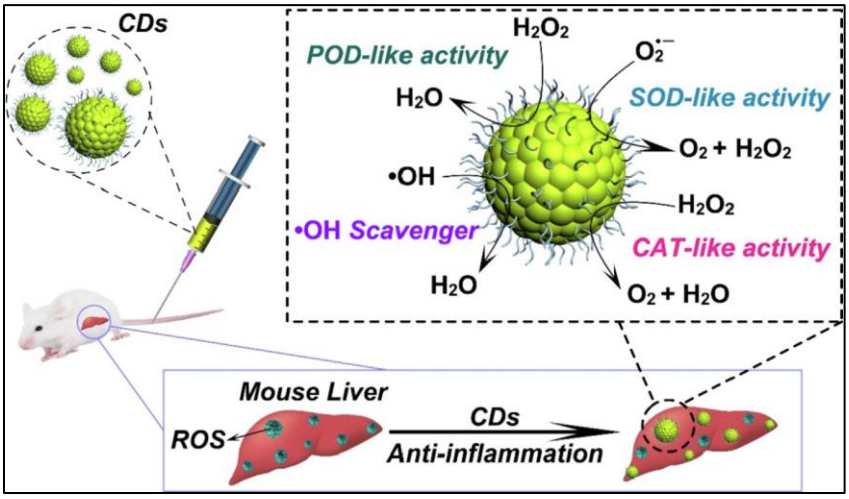

(a)

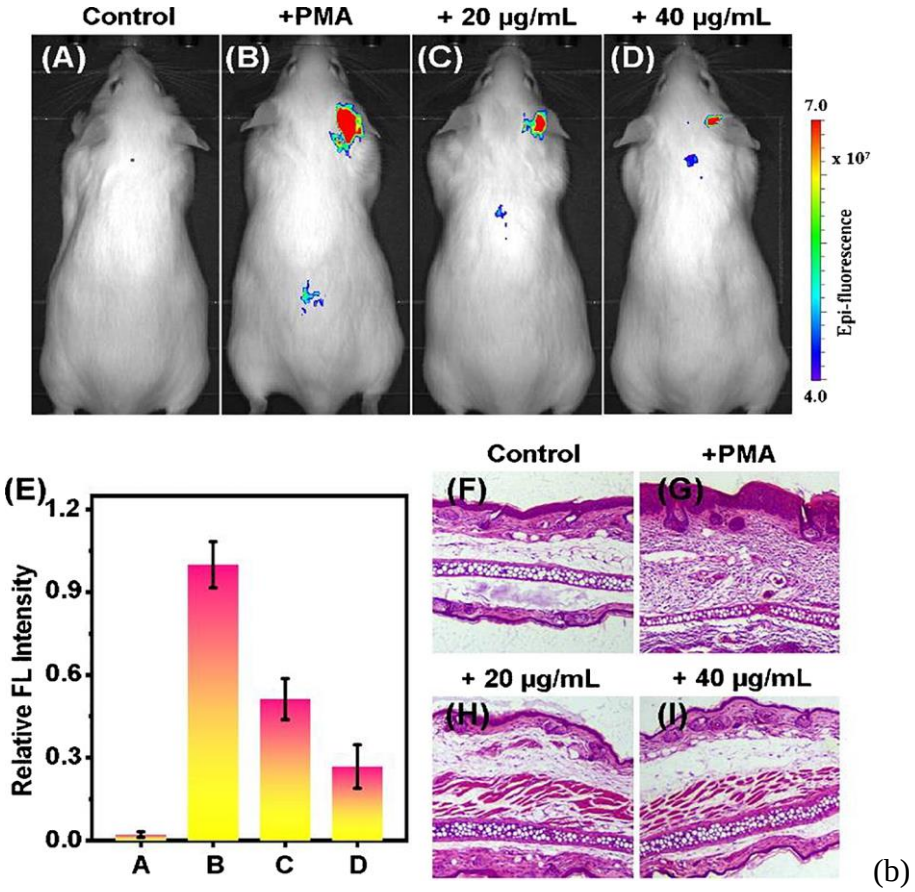


(b)

Han et al synthesized ultra-small CNDs which were able to successfully penetrate the dept of tumor sites in tumor-induced mice models. These CNDs could reach the tumor site selectively and increase the temperature of the area upon NIR radiation, resulting in cancer cell fatality. As an important feature, these CNDs got removed from the body through the liver and lungs [136].

In another case study, m-phenylenediamine-based CNDs were successfully used for the pharmacological treatment of acute kidney injury (AKI) due to their robust proven radical scavenging characteristics [141]. Table 3 gives information about diseases in which CNDs have shown therapeutic effects along with their proposed mechanism of action.

**Table 3. Recent *In Vivo* Studies Using CNDs as Therapeutic Agents.**

| Source of Synthesis | Focused Disease | Proposed Mechanism of action | Ref. |
|---|---|---|---|
| TAPP and CA | Breast cancer (HCC827 and MDA-MB-231cells) | modification with Cetuximab/ ROS production | [142] |
| Ginger | Human hepatocellular carcinoma cells (HepG2) | Up-regulation of the expression of p53 protein/ elevated ROS production | [143] |
| Citric acid and urea | H22 tumors | NIR photothermal conversion efficiency | [144] |

## Conclusions

It is undeniable that CNDs have recently attracted the researchers' interest due to their low cost of production, exhibiting intrinsic fluorescence, tunable functional groups, high water dispersity, and less harm to living cells, compared to heavy metal-based quantum dots. CNDs could be used as drug carriers or even be applied independently for the treatment of many illnesses correlated with ROS generation in cells. Different types of CNDs with a variety of functional groups have demonstrated a significant capacity for free radical scavenging. On the other hand, in many cases, the toxicity of CNDs towards healthy cells has been reported in some cases which might limit the utilization of these promising moieties in biological applications. The dual behavior of CNDs in terms of oxidative stress effects could result from different functional groups and electrical charges on their surfaces. The utilized precursors for CNDs' synthesis might lead to different levels of biocompatibility as well. Putting all these aspects of CNDs' effects together, several precise assessments are necessary to obtain the best structure for CNDs, safely applicable in medical applications.

Overall, it is concluded that CNDs can penetrate the cell membrane through different mechanisms. Also, they are able to localize in many subcellular organelles such as mitochondria, nucleus, cell membrane, etc. The biological fate of CNDs is highly dependent on their size, surface

charge, surface functional groups, and also the cell type which were discussed in detail. In several studies, the anti- and pro-oxidation features of CNDs have been investigated and both turned out to be beneficial. However, in terms of utilizing the pro-oxidation effects, in many cases, CNDs have been used along with the NIR irradiation to maximize the ability to kill cancer cells. Finally, due to increasing the number of *in-vivo* studies focusing on the therapeutic application of CNDs, these moieties are turning into promising tools for medical treatments, specifically with potential uses in the treatment of oxidative stress-related problems.

# CHAPTER III: EFFECT OF DOPING HETEROATOMS ON THE OPTICAL BEHAVIORS AND RADICAL SCAVENGING PROPERTIES OF CNDS

## Overview

Heteroatom doping is regarded as a promising method for controlling the optoelectronic properties of carbon nanodots (CNDs), notably their fluorescence and anti-oxidation activities. In this study, phosphorous (P) and boron (B) are used at different quantities in the CNDs structures to investigate their effects on the optical and anti-oxidation properties. Both the dopants can enhance light absorption and fluorescence, yet via different approaches. After doping, the UV-Vis absorption of high P%-CNDs demonstrated a slight blue shift (348 to 345nm), while the high B%-CNDs showed a minor redshift (348 to 351 nm), respectively. The fluorescence emission wavelength of doped CNDs changes marginally while the intensity increases significantly. The structural and composition characterizations show elevated levels of C═O on the surface of high P%-CND compared to low P%-CNDs. In B-doped CNDs, more $NO_3^-$ functional groups and O–C═O bonds, and fewer C–C bonds form at the surface of high B%-CNDs compared to the low B%-CNDs. A radical scavenging study using 2,2-diphenyl-1-picrylhydrazyl (DPPH) was carried out for all CNDs. It was found the high B%-CNDs exhibited the highest scavenging capacity. The effects of the atomic properties of dopants and the resulting structures of CNDs, including atomic radius, electronegativity, and bond lengths with carbon, on the optoelectronic property and antioxidative reactions of CNDs are comprehensively discussed. It suggests that the effect of P-doping has a major impact on the carbogenic structure of the CNDs, while the B-doping mainly impacts the surface functionalities.

## Introduction

Carbon nanodots (CNDs) are zero-dimensional carbon nanoparticles typically less than 10 nm in size [9]. CNDs have piqued the interest of researchers owing to their tunable optoelectronic features, especially high intrinsic fluorescence, along with their biosafety, making these moieties promising candidates for a wide range of applications, including biomedical [145], [146] electrocatalysis, and energy storage [147]. The optical behavior of CNDs is affected by a combination of variables, i.e., precursors, synthesis procedures [148], final particle size [149] surface functional groups, and doping with various heteroatoms [150]. Among these, surface chemistry appears to have a significant impact on the optical properties of CNDs. The fluorescence of CNDs stems from photon absorption in their carbonaceous core, which then incorporates with the charge recombination at the surface [151]. Although the role of the amorphous carbonaceous core of CNDs in their optical performance is not negligible, it has been demonstrated that surface manipulation of CNDs may induce more significant changes in the emissive patterns, thereby promoting the fluorescence features [150]. The effect of surrounding functional groups also seems to be complicated. Forming dipole moments resulting from functional groups on the CNDs' surface could affect the properties of CNDs by not only the intrinsic dipole moment of functional groups but also the induced dipole formed between the functional groups and the carbogenic core edges [152]. Although it is difficult to predict, it is generally believed that functionalization—especially with groups containing oxygen and nitrogen—can affect the $\pi$–$\pi^*$ and n–$\pi^*$ electronic transitions more than the others outlined in CNDs (e.g., $\sigma$–$\sigma^*$, $\sigma$–$\pi^*$, and n–$\sigma^*$) [153]–[155]. As one of the optoelectronic features, the anti-oxidation properties of CNDs can also be altered by manipulating the functional groups. CNDs are usually known as n-type (electron donor) moieties since they may donate electrons to other materials. This feature of CNDs, which is primarily the result of surface

functional groups, is the basis of their anti-oxidation characteristics, allowing them to function as radical scavengers. For example, Ji et al. studied the individual effect of COOH and $NH_2$ surface functional groups on the radical scavenging potential of CNDs, through which the direct or indirect hydrogen atom transfer could be the possible mechanism engaging these functional groups in the radical scavenging reactions [116].

Doping CNDs with heteroatom elements is one of the effective ways to modify their optical properties since it can create changed electronic states in their carbonic framework structures and influence their surface chemistry as well [156]. Doping can alter the highest occupied molecular orbital (HOMO) and lowest unoccupied molecular orbital (LUMO) levels. Monitoring variations of the band-gap energy levels driven by doping allows for analyzing the function of these dopants on the structure and, as a result, modifying the optical characteristics of CNDs [157].

Nitrogen (N), phosphor (P), boron (B), and sulfur (S) are the closest neighbors to carbon (C) in the periodic table, which have been applied widely for doping different types of CNDs, converting them to practical tools for a broader range of applications [158]–[161]. The anti-oxidation potency of CNDs is also influenced by the dopant elements. For instance, N and S have been demonstrated to regulate the anti-oxidation potential of CNDs through several proposed mechanisms, such as hydrogen atom transfer or proton-coupled electron transfer, in various acidic media [135], [162]. Zhang et al. conducted a study of the radical scavenging potential of N, S co-doped CNDs employing various techniques, including UV-Vis-based and electrochemical assays. They concluded that a synergistic effect of both N and S as dopant elements could promote the radical scavenging abilities of these CNDs by providing greater electronegativity difference and defect production, respectively [117].

Doping with P, given its greater atomic size than that of C, could alter the electronic structure of CNDs [41]. In a study by Li et al., an aggregation-induced red shift was observed in the fluorescence emission wavelength of P-doped CNDs [163]. This phenomenon was explained by the fact that P atoms—as n-type donors—can enrich the electron density of the CNDs, and in combination with the size increment after aggregation, led to a π–π conjugation increment [163]. The effect of B-doping, however, has been going through extensive controversies. Some studies have shown a reducing effect on the fluorescence intensity [24]; while there are reports indicating the opposite [164]. Some researchers believe that the difference between the size of B–C, and C–C bonds can be considered a disorder that affects fluorescence [165]. The charge transfer changes in the structure of N-doped CNDs upon doping them with P and B have been studied by attaching nickel (II) phthalocyanine to their surfaces [166]. It was discovered that adding P to the CNDs accelerates the charge transfer process from carbon dots to phthalocyanine. B doping, on the other hand, has the opposite impact since the coupled hole transport is a slower process than electron transfer. Nonetheless, B-doping has been proven to promote charge transfer in other studies [167] driving more research in this area.

Despite the influence of heteroatoms on the optical properties of carbon nanomaterials having been extensively studied, some key aspects of these effects on fluorescence emission and UV-Vis absorption remain unclear. In the present work, we specifically investigate the effect of different levels of doped P and B on the optoelectronic and anti-oxidation properties of CNDs, which is known little and less studied previously. Finding a clear relationship among the electronic states, optical behavior, and radical scavenging capability of CNDs allows us to design superior CNDs, particularly for reactive oxygen species (ROS) scavenging applications.

## Materials and Methods

### Materials

Citric acid (CA), boric acid (BA), ethylenediamine (EDA), phosphoric acid (PA), quinine sulfate (QS), sulfuric acid (SA), 2,2-diphenyl-1-picrylhydrazyl (DPPH), and methanol were purchased from Sigma-Aldrich Chemie GmbH (Munich, Germany) and were used as received. All aqueous solutions were prepared using fresh deionized water. Dialysis bags were purchased from Sigma-Aldrich Chemie GmbH (Munich, Germany) and used for CND purification.

### Synthesis of CNDs

Based on the employed dopant element and the associated concentrations, five different CNDs were designed and synthesized, as summarized in Table 4. A one-step closed-vessel microwave method with similar conditions was used to synthesize all CNDs. Microwave method is a proven approach that prevents the formation of undesirable side products [168]. Also, using EDA results in higher yields than other N-source precursors [169]. Based on Table 4, the required quantities of each precursor were dissolved in deionized water and stirred until a clear solution was obtained. The solution was then transferred to the microwave synthesizer and heated up with proper setpoints (Temperature = 180°C, Power = 300 watts, and Pressure = 100 Psi) for 30 minutes. After 30 minutes, the obtained brown solution was centrifuged at 4000 rpm for 20 minutes to precipitate large particles. The supernatant was further filtered using a 1 kDa dialysis membrane in deionized water for 48 hours. Afterward, the product was freeze-dried, and the brown CND powder was collected, which was stored at room temperature for later use.

**Table 4. Synthesis Design of Different CND Samples**

| Sample Name | CNDs Type | P/B Level | Precursors | | | |
|---|---|---|---|---|---|---|
| | | | CA (gr) | EDA (mL) | PA (mL) x 21.92 N* | BA (gr) |
| E-CNDs | N, CNDs | 0 | 1 | 1 | 0 | 0 |
| Low P%-CNDs | N, P CNDs | Low P | 1 | 1 | 0.5 | 0 |
| High P%-CNDs | N, P CNDs | High P | 1 | 1 | 2 | 0 |
| Low B%-CNDs | N, B CNDs | Low B | 1 | 1 | 0 | 0.23 |
| High B%-CNDs | N, B CNDs | High B | 1 | 1 | 0 | 0.95 |

* Normality

**Characterization**

The size measurement was conducted using atomic force microscopy (AFM, MFP-3D Origin, Asylum) by the height profiles [170]. A 0.002 mg/mL solution of each CND sample was prepared in deionized water, sonicated for 20 minutes, drop-casted on a mica surface, and set aside to dry for AFM imaging. Fourier transform infrared spectroscopy (670 FTIR, Varian) was carried out to identify the formation of functional groups on the CNDs' surface. Further elemental data analysis was carried out using X-ray photoelectron spectroscopy (ESCALAB 250Xi XPS, Thermo-Fisher). Solutions of 10 mg/mL of all CND samples were prepared, drop-casted, and dried out for XPS analysis. Dynamic light scattering (DLS, Malvern Instruments ZEN3600) was used to measure the zeta potential of CND samples with a concentration of 0.005 mg/mL. A spectrophotometer (XploRA ONE, Horiba) equipped with a coupled-charged device (CCD) camera was used to perform the Raman spectroscopy of CNDs, and a laser with 532 nm was used as the excitation light. The UV-Vis absorption and the fluorescence spectrum of CND samples were measured using a UV-Vis spectrophotometer (UV-Vis-NIR, Agilent) and a fluorometer (Fluoro-Max 4 fluorometer, Horiba), respectively.

## Optical Features Studies of CNDs

### *UV-Vis Studies*

All CND samples of 0.025 mg/mL solutions were prepared, and their UV-Vis spectra were obtained and plotted to investigate the effect of added dopant heteroatoms on the absorbance. Also, to further evaluate the impact of doping on the band-gap energy, Tauc plots were studied using Eq. 1 [171].

$$(\alpha . h\nu)^{\frac{1}{\gamma}} = B\ (h\nu - E_g) \qquad \textbf{Eq. 1}$$

where $\alpha$, $h$, $\nu$, $E_g$, and $B$ are the absorption coefficient, Planck constant, photon frequency, band-gap energy, and proportionality constant, respectively. In the calculation of the band-gap energy, we assumed that, due to the amorphous structure of CNDs, the direct electronic transition takes place upon the emission of UV light; therefore, the γ factor was considered 0.5. Once plotted, a tangent line was drawn on the curve in the area of 3 to 4 eV on the X-axis. The intersection point is considered as the apparent band-gap energy, which could be originating from molecular-like HOMO and LUMO of the carbogenic core of CNDs [171]–[173].

### *Fluorescence Study and Quantum Yield (QY) Measurement*

A 0.025 mg/mL solution of each CND sample was prepared, and the fluorescence emission spectrum was monitored at a wide range of excitation wavelengths. The effect of dopant heteroatoms on fluorescence emission intensity and the maximum wavelength shifts were investigated. Also, the relative quantum yield (QY) was calculated with reference to QS as a standard at the excitation wavelength of 360 nm. A 0.1 mg/mL solution of QS in $H_2SO_4$ (0.1 M) was used as the reference. The integrated fluorescence of the CNDs at the excitation wavelength of 360 nm was calculated. The slope of fluorescence intensity over the maximum UV absorbance of each CND sample was calculated and compared to QS using Eq. 2 [6].

$$\Phi_C = \Phi_{QS}\left(\frac{K_C}{K_{QS}}\right) \times \left(\frac{\eta_C}{\eta_{QS}}\right) \quad \textbf{Eq. 2}$$

where $\Phi$ is the QY, $K$ is the slope determined from the curves, and $\eta$ is the refractive index. The subscripts $C$ and $QS$ represent the CNDs and QS, respectively. It is noted that $\Phi_{QS}$ and $\frac{\eta_C}{\eta_{QS}}$ are considered to be 0.54 and 1, respectively [6].

**Radical Scavenging Measurement of CNDs**

As an established method of evaluating the anti-oxidation capability of CNDs, DPPH radical scavenging assay was used in which the UV-Vis absorbance change of DPPH radical solution was monitored at 517 nm upon the addition of CNDs [91], [174]. Different CND concentrations were prepared in deionized water, incubated with a solution of DPPH (0.02 mg/mL in methanol), and mixed simultaneously at a dark condition for 2 h. Finally, the UV-Vis absorbance of each solution was measured at 517 nm. The anti-oxidation activity% of CND samples was calculated using Eq. 3 [135], [162].

$$Antioxidation\ activity\ (\%) = \frac{A_0 - A_c}{A_0} \times 100 \quad \textbf{Eq. 3}$$

where $A_0$ and $A_c$ are the absorbances of DPPH radical at 517 nm in the absence and presence of CNDs, respectively.

## Results and Discussions

**Synthesis and Characterization of CNDs**

The closed-vessel microwave approach was chosen for the synthesis to obtain a satisfactory B-doped product. Once the synthesis process for producing B-doped CNDs was optimized, the synthesis procedures of other CNDs were adjusted accordingly. The yield of synthesis reactions of E-CNDs, Low P%-CNDs, High P%-CNDs, Low B%-CNDs, and High B%-CNDs were 2.5%, 4.42%, 1.73%, 5.38%, and 3.38%, respectively.

AFM results showed that all CNDs were spherical with an average size of 2.31 ± 0.28 nm for E-CNDs, 0.43 ± 0.04 nm for Low P%-CNDs, 0.75 ± 0.07 nm for High P%-CNDs, 0.2 ± 0.01 nm for Low B%-CNDs, and 0.81 ± 0.11 nm for High B%-CNDs (Figure S1.1).

Figure 7 shows the FTIR spectra of the synthesized CNDs. The C═O stretch at 1650 $cm^{-1}$ and the O–H stretch at 3100 $cm^{-1}$ in the FTIR spectra confirm the presence of COOH group in all CNDs except the High P%-CNDs [134]. The observed peak around 1550 $cm^{-1}$ can be attributed to C═C of the graphitic structure of CNDs core [70]. In all CNDs, the N–H bonds appeared around 3300-3350 $cm^{-1}$ (amine N–H). In both P-doped CNDs, the peaks that appear at 1040 and 2330 $cm^{-1}$ are assigned to P–$H_2$ and P–H bonds, respectively [161]. In the case of B-doped CNDs, the band that appears at 1000 $cm^{-1}$ is assigned to B–C chemical bonds and the band that appears at 3268 $cm^{-1}$ is assigned to B–OH bonds [175]. However, the broad peak at 2600–3400 $cm^{-1}$ corresponding to O–H and N–H bonds, observed in E-CNDs, Low P%-CNDs, Low B%-CNDs, and High B%-CNDs, was not shown in the High P%-CNDs' FTIR spectrum. This can be explained by the dehydration effect of the high concentration of phosphoric acid used in the synthesis of High P%-CNDs.

**Figure 7. FTIR Results of E-CNDs, Low P%-CNDs, and High P%-CNDs (a); Low B%-CNDs and High B%-CNDs (b).**

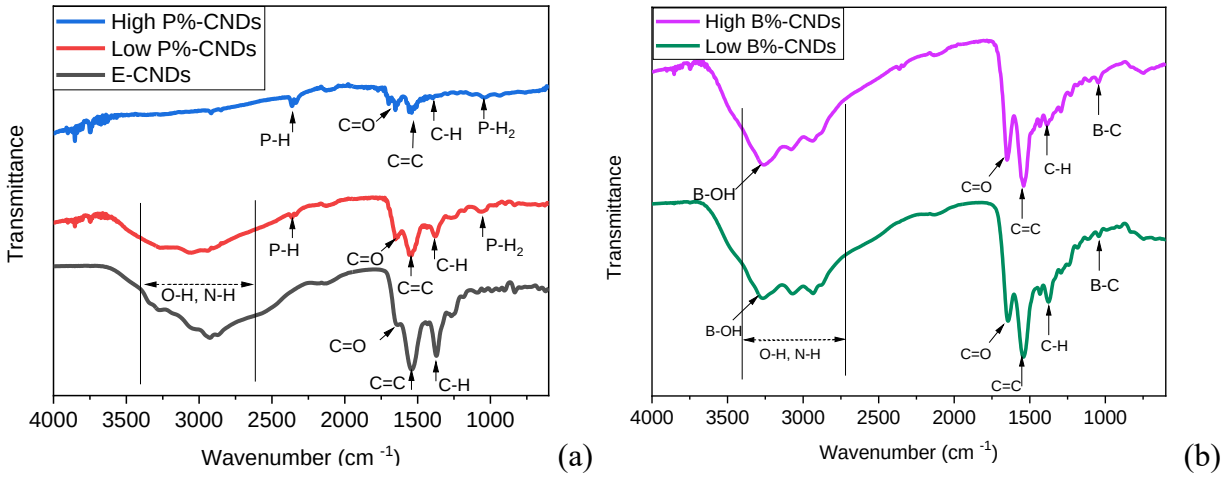


The XPS results of all CND samples are presented in Figure S1.2 of the full survey, Figure 8 for C 1s, Figure S1.3a-g for P 2p, B 1s, and N 1s. Table S1.1 summarizes the XPS data analysis for the breakdown atomic percentage of P and B for each CND sample. In the analysis of E-CNDs, the P and B quantities were detected as trace levels of 0.04% and zero, respectively. The Low and High P%-CNDs contain 0.38% and 4.47% phosphorus while the Low and High B%-CNDs have 0.5% and 1.95% boron, respectively. The analysis of C 1s scan of CND types (see Figure 8 and Table 5) shows that C–C and C═O chemical bonds have been detected in all CNDs types, with the highest percentage belonging to High-P% CNDs for both bonds. On the other hand, O–C═O chemical bond has not been detected in High-P% CNDs [176], while detected in B-CNDs [167]. C–O–C chemical bond has only been detected in the structure of E-CND. Only in the case of High-B% CNDs, peaks assigned to the metallic bonds of C have been observed.

**Table 5. Percent of Detected Carbonic Chemical Bonds by XPS.**

| Assigned chemical bond (%) | E-CNDs | Low P%-CNDs | High P%-CNDs | Low B%-CNDs | High B%-CNDs |
|---|---|---|---|---|---|
| C–C | 28.61 | 32.93 | 43.99 | 4.43 | 3.66 |
| O–C═O | 20.31 | 23.35 | – | 32.91 | 59.87 |
| C–O–C | 18.09 | – | – | – | – |
| C═O | 33 | 43.72 | 53.82 | 43.44 | 23.92 |
| Metallic bonds with carbon | – | – | – | 19.22 | 12.56 |

**Figure 8. C 1s Scan of E-CNDs (a), Low P%-CNDs (b), High P%-CNDs (c), Low B%-CNDs (d), and High B%-CNDs (e).**

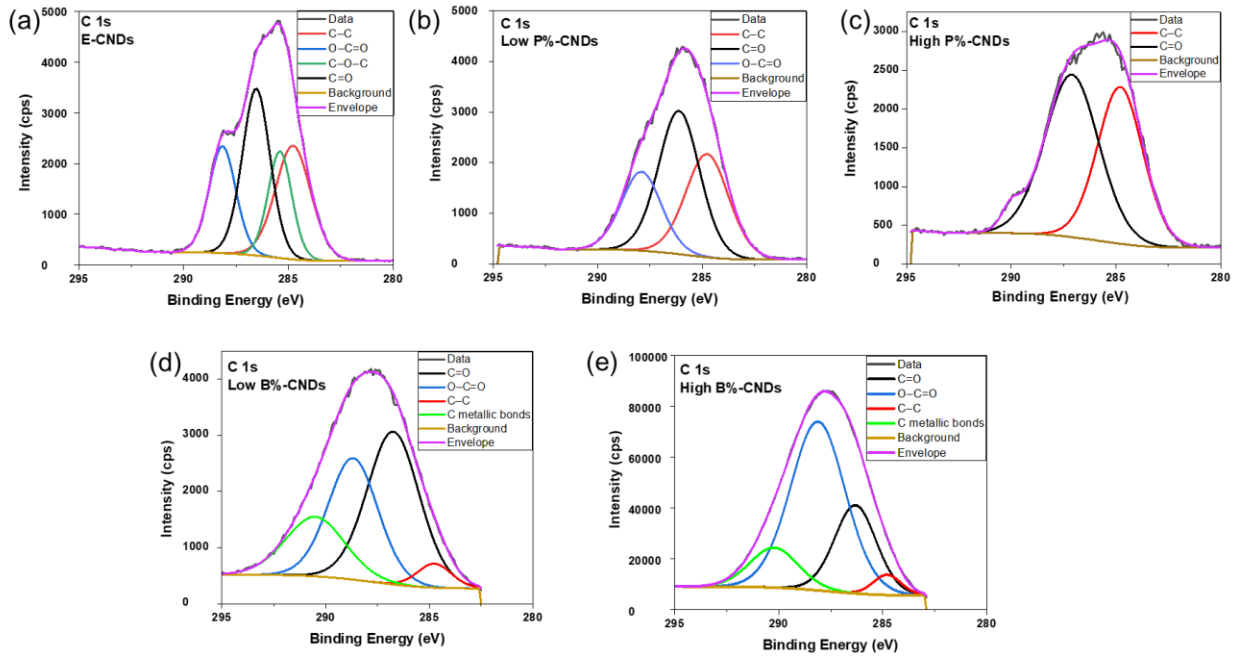


From Figure S1.3a,b and Table S1.2, one can find that in Low P%- CNDs, all P atoms are present in the form of P–C bonds, while the P–O and P–N bonds in addition to P–C bond begin to form in High P%-CNDs [166], [177], [178]. From Figure S1.3c,d and Table S1.3, it can be seen that in Low B%-CNDs, the primary presence of B is mainly binding with the functional groups of the C, i.e., –COO. In High B%-CNDs, B is more likely to form chemical bonds with CND's surface

carbon atoms as well [25], [164], [166], [167], [175], suggesting that B atoms might have less penetration capability to the carbogenic core of CNDs. In the B doping C 1s scans, two additional peaks also appeared at around 290 eV which can be assigned to metal carbonates [179].

**DLS Results**

DLS was conducted to further investigate the effect of doping on the surface zeta potential (ζ) of CNDs and the results are shown in Figure S1.4a–e and Figure S1.5a. The carboxylic acid group is known to be the dominant source of negative charge on the surface of CNDs [180]. In P dopant CNDs, positive surface charge shift was found where the High P%-CNDs (ζ= -9.8 mV) and Low-P%-CNDs (ζ= -21.1 mV) present fewer negative charges compared to E-CNDs (ζ=-27.6 mV). In contrast, more negative surface charge of the B dopant CNDs was found as ζ=-34.1 mV for High B%-CNDs and ζ= -28.1 mV for Low B%-CNDs which can be attributed to the high percentage of O–C═O chemical bonds (59.87%). With the decrease of O–C═O chemical bond portion, the surface charge of Low B%-CNDs and High P%-CNDs tend to have less accumulated negative charge. The results are corroborated by the percentage of O–C═O bonds found in different dopant CNDs in Table 5.

**Raman Spectroscopy of the CNDs**

To further evaluate the potential effect of doping on the internal graphitic structure of CNDs, Raman spectroscopy was carried out. The G-band represents the $sp^2$ hybridization of C atoms in their planer geometry, while the D-band represents the presence of dangling C atoms with the $sp^3$ hybridization [181]. After baseline subtraction, the Raman spectra were plotted for E-CNDs, High P%-CNDs, and High B%-CNDs (Figure S1.6). As expected, the D and G bands were observed at 1332 and 1585 $cm^{-1}$, respectively. The degree of disorder—induced by P and B doping—was calculated using the $I_D/I_G$ ratio and was found to be 0.91, 0.73, and 0.69 for E-CNDs,

High P%-CNDs, and High B%-CNDs, respectively (Figure S1.5b). It was observed that E-CNDs possess the highest $I_D/I_G$ ratio among all samples, which is due to the presence of defective moieties in their structure [182]. The High P%-CNDs and High B%-CNDs, on the other hand, have lower $I_D/I_G$ ratios. The observed difference in this parameter can be attributed to the interference of N, P, and B in the carbogenic structure of CNDs during synthesis. As summarized in Table S1.4, the bond length of C–N is much different (17.46%) than C–C while the lengths of C–P (9.85%) and C–B (4.92%) are less different. Therefore, the effect of C–B defects on the carbonic core of CNDs is less than those from C–P and C–N while the C–N has the largest effect on forming defective structures [183].

**Optical Features of CNDs**

***UV-Vis Studies and Energy Band Gap***

CNDs usually exhibit two significant UV-Vis absorbance peaks [116]. The first is a shoulder peak near 240 nm related to π–π* transitions of C═C bonds originating from the carbogenic cores. The second one is a strong, broad peak near 345 nm, attributed to n–π* transitions of non-binding orbitals mostly belonging to C═O bonds on the surface of CNDs. Hence, the latter is more affected by the functional groups and dopant heteroatoms [161]. Figure 9a exhibits the UV-Vis spectrum of all synthesized CNDs at 0.025 mg/mL. Both B and P dopants and doping level increase UV-Vis absorbance. This can be explained by the formation of abundant functional groups on the surface of CNDs, i.e., P–O and P–H of P-CNDs, and B–N and B–OH of B-CNDs (see Figure 7). Since N has larger electronegativity (3.04) than P (2.19) and B (2.04), electrons of functional groups involving N are less likely to get excited compared to the electrons of functional groups involving P or B. Based on this, one could conclude that the availability and feasibility of n–π* transitions would be in the order of B-CNDs > P-CNDs > E-CNDs.

**Figure 9. UV-Vis Spectra (a) and Calculated Band-Gap Energies (b) of CND Samples.**

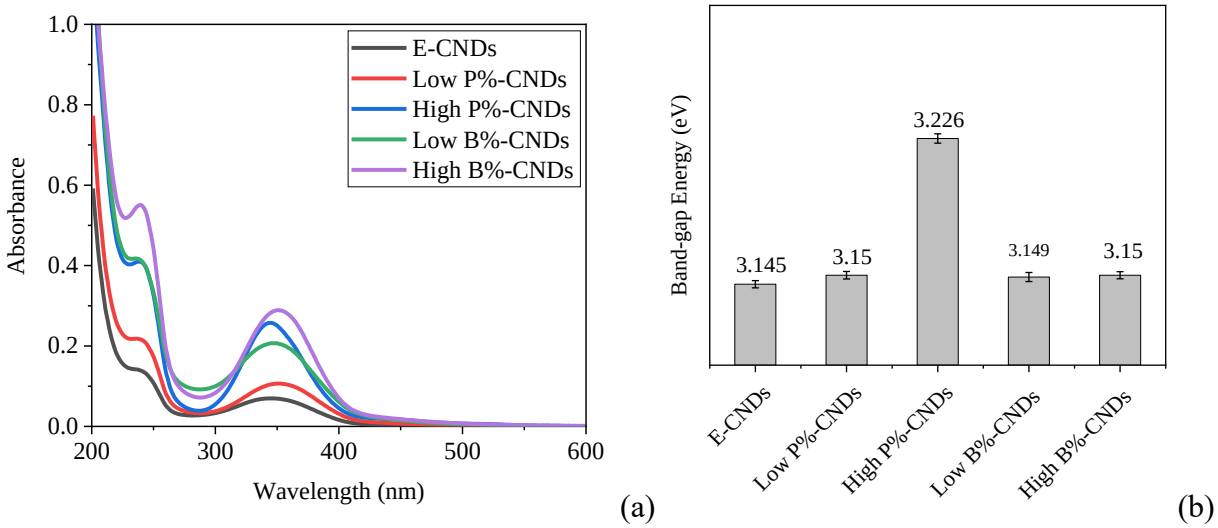


From the UV-vis absorbance spectra, Tauc plots were obtained to estimate the energy band gap (Figure S1.7). It was found only the High P%-CNDs has a significant increase of band gap to 3.23 eV from around 3.15 eV of all other types of CNDs. It is expected to observe a lower energy band gap in High P%-CNDs, while surprisingly, it increased significantly. A similar observation was reported by Sekar, et al [184]. This can be attributed to the presence of more C═O chemical bonds (Table 5) which play a key role in strengthening the n–π* transition. Higher electronegativity of P compared to B causes an increase in the n–π* transitions energy gap, which is also apparent as a shift in the XPS peak (287.1 eV vs. 286 eV for C═O in High P%-CNDs and High B%-CNDs, respectively).

In the case of B dopant, the energy gap change is insignificant, a good agreement with the fact that the effect of B doping on the functional groups is more dominant compared to that on penetration discussed earlier. It is consistent with the effect of functional groups on decreasing the HOMO and LUMO [185]. As a result, the maximum absorption of High P%-CNDs has blue-

shifted. This blue shift is due to the higher energy required for the electron transition between HOMO and LUMO [171].

***Fluorescence, Quantum Yield, and Deconvolution of Fluorescence Peaks***

The fluorescence spectra of all CND samples were examined at different excitation wavelengths (Figure 10). The most significant fluorescence emission was observed at the wavelength of 360 nm in all samples. Unlike the emission intensity— which varied considerably across all samples—the maximum emission wavelength variation was insignificant (443 nm for E-CNDs and B-doped CNDs, 447 nm for P-doped CNDs). Also, in all cases, excitation-independent fluorescence emission was observed. The addition of P boosted the fluorescence intensity by providing additional electrons as an n-type donor, as seen in Figure S1.8. However, compared to P, the addition of B dopant led to a more significant enhancement in the fluorescence intensity. It is believed that higher fluorescence usually originates from fewer defects, while low/medium fluorescence originates from having more defects in CNDs [186]. Since the B dopant has shown less penetration to the core, B-doped CNDs are assumed to have a more ordered core than P dopant CNDs, thus higher fluorescence yield. This analysis is in good agreement with the measured fluorescence and Raman results, i.e., the higher fluorescence intensity of B-doped CNDs over others.

**Figure 10. The Fluorescence Spectra of E-CNDs (a), Low P%-CNDs (b), High P%-CNDs (c), Low B%-CNDs(d), and High B%-CNDs (e).**

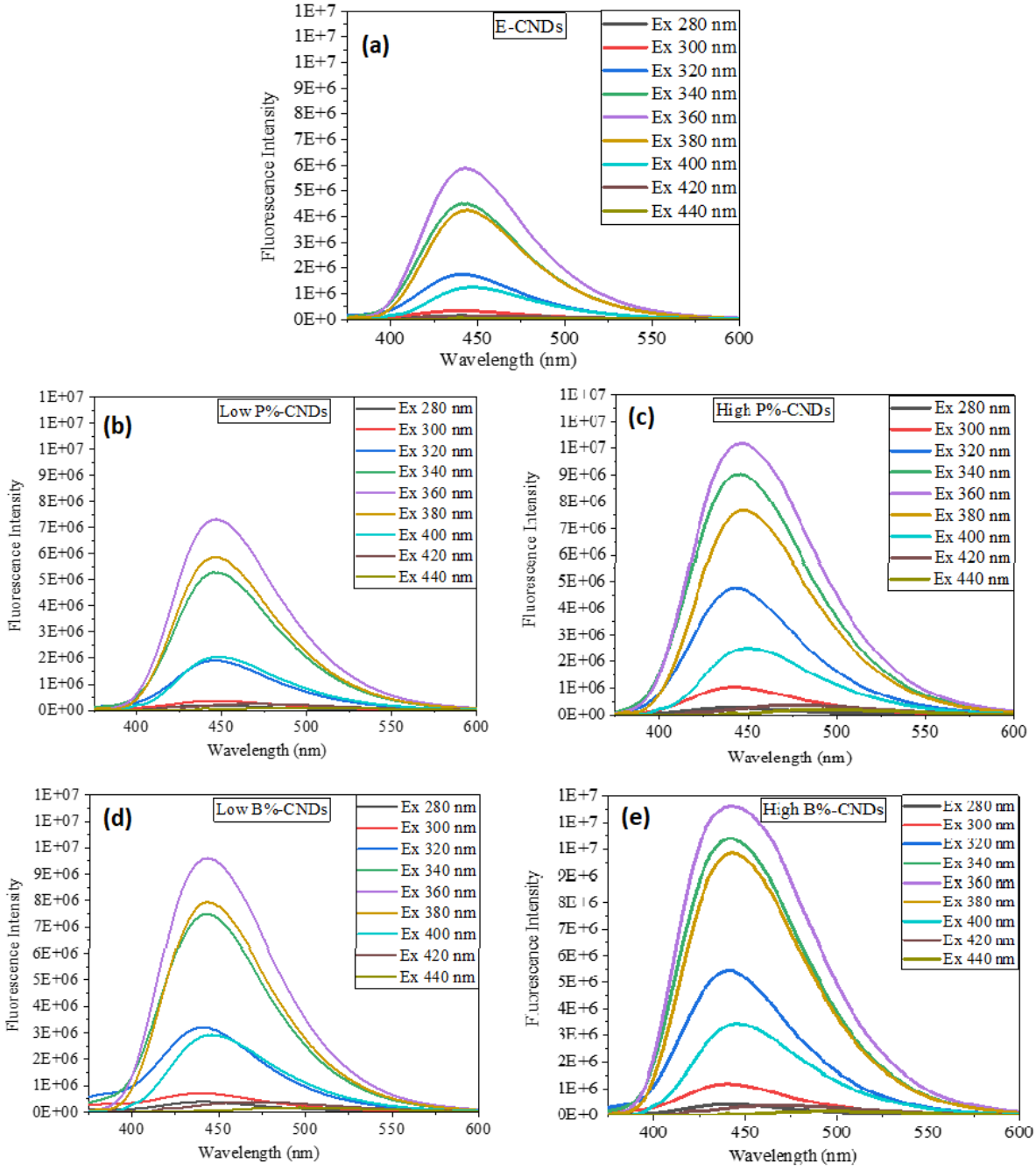

The QY of all CNDs was calculated using QS as a reference (Figure S1.9a). Figure S1.9b shows the QYs of all synthesized CNDs. Although co-doping is expected to enhance the QY of CNDs due to the synergistic impact of trapped electron-hole pairs of dopants [156], such a trend was not observed in P and B dopants. Surprisingly, the calculated QY trend of CNDs did not match their fluorescence intensity order. With the addition of P to CNDs, the QY was observed to decline, with similar observation in the case of B doping. This can be explained by the fact that QY is calculated using both the light absorbances and emission intensities of each CND. Because doping affects the UV-Vis absorption properties of CNDs differently than fluorescence, it is not surprising that the QY fluctuated. Another plausible explanation for the QY results is that the attained QY is dependent on the balance of the surface –COOH and –OH groups. This balance may have been disrupted in various ways during doping CNDs with P and B due to the formation of additional functional groups on the surface [186].

Deconvoluting the fluorescence peaks of CNDs is a technique that aids in determining the origin of the fluorescence. The emission peak of CNDs is deconvoluted into two Gaussian sub-peaks, namely, fit peak 1 and fit peak 2, that reflect the fluorescence caused by $sp^2$ defects and the surrounding functional groups, respectively [187], [188]. Figure 11a-c and Table S1.5 demonstrate the relative dominance of the sub-peaks as well as their full width–half maximum (FWHM) ratios. Figure 11a shows that in the High P%-CNDs, fit peak 1 is dominant, indicating that $sp^2$ defects have more impact on the fluorescence than the functional groups.

**Figure 11. Fluorescence Deconvolution Graphs for High P%-CNDs (a), High B%-CNDs (b), and E-CNDs (c) Samples.**

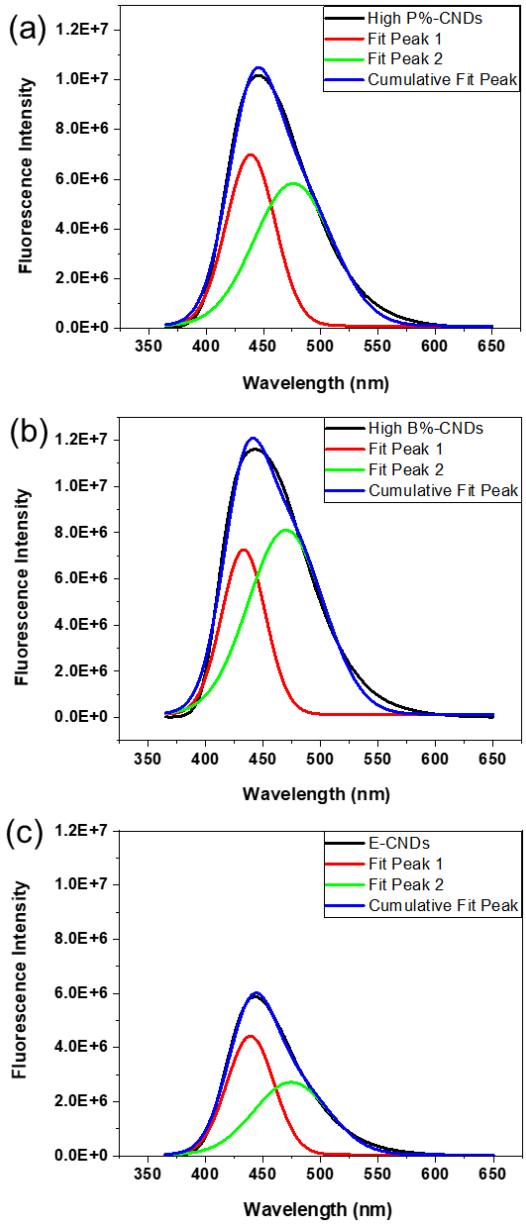


The reverse effect is seen in High B%-CNDs, where fit peak 2 has a more considerable dominance, corresponding to the stronger effects of functional groups on fluorescence. In addition, the FWHM ratio (Table S1.5) of fit peak 1 to fit peak 2 is calculated as 0.62 and 0.58 for High P%-CNDs and High B%-CNDs, corresponding to the dominance of $sp^2$ defects or surface

functional groups, respectively. In E-CNDs with N as the dopant heteroatom, the fit peak 1 dominates the fit peak 2, and the ratio of FWHM of $\frac{fit\ peak\ 1}{fit\ peak\ 2}$ is larger than the high P% and high B% CNDs. This outcome agrees with the Raman data which indicates that N plays a significant role in causing defects in the carbonic core due to the length of the N–C bond.

On the other hand, the different effects of P and B dopants on the surface functional groups to some extent account for the fluorescence intensity. Since the pKa of phosphoric acid [189] is lower than boric acid [190], it is more likely that the OH groups of phosphoric acid undergo deprotonation than the OH groups of boric acid. Hence, there could be more OH groups available on the surface of B-doped CNDs during the synthesis. As electron donors, the OH groups can suppress non-radiative processes and improve the integrity of the π conjugated system [191], [192]. This can contribute to the increased fluorescence of B-doped CNDs. Furthermore, as discussed above, the surface states primarily cause the fluorescence of B-doped CNDs, and their fluorescence was observed to be higher than P-doped CNDs, one can conclude that the surface chemistry of CNDs plays a more significant role in the origin of fluorescence than the defects induced in their graphitic core to the P and B doped CNDs.

Further analysis of XPS data corroborates the observation of high fluorescence in high B% CNDs. In the N 1s XPS scan of E-CNDs and High P%-CNDs (Figure S1.3e,f), only one peak was observed at ~400.2 eV which is attributed to $–NH_2$ bonding. In the N 1s XPS scan of High B%-CNDs (Figure S1.3g), another peak appeared at ~403 eV, which can be assigned to $NO_3^-$ bonding. It has been shown that CNDs with fewer amino groups on the surface have higher fluorescence than amino-rich CNDs because of the surface passivation with the presence of $NH_2$ groups [41], [193]. On the other hand, $NO_3^-$ functional group is capable of strengthening the fluorescence by providing π–π conjugations through the electron resonance among N–O bond in its structure [194].

**Radical Scavenging Measurement of the Synthesized CNDs**

CNDs showed as promising candidates for ROS scavenging in cellular studies [76]. The UV-Vis absorbance spectra of DPPH radicals (0.02 mg/mL) at different concentrations of CNDs were obtained and shown in Figure 12a-e. As the concentration of CNDs increases, the absorbance intensity falls, showing their radical scavenging capabilities. Figure 12f illustrates the anti-oxidation activity (%) of different CNDs vs. their concentration calculated by Eq. 3. Compared to E-CNDs, the P or B-doped CNDs presented higher levels of anti-oxidation activities. Specifically, the anti-oxidation activity (%) increased with the increase of the P or B where the High B%-CNDs performed 78.68 % anti-oxidation activity, being superior to the other CNDs. The order of the anti-oxidation capability was found to be High B% > High P% > Low B% > Low P% > E-CNDs.

This performance can be attributed to the transfer of both electrons (induced by n-type N doping) and holes (related to boron p-type doping) during the interactions between DPPH and CNDs. According to XPS analysis, High B%-CNDs have the highest percentage of O–C═O in their structure, which can act as a hydrogen donor, donating a hydrogen ion to a free radical species and neutralizing it [195]. Additionally, compared to P-doped CNDs, XPS data confirmed that by adding more B to the CNDs' structure, the percentage of C–C ($sp^3$ hybridization) decreased significantly. As a result, it is expected that there is a higher probability of carbon $SP^2$ hybridization and thus a high possibility of electron transfer between the High B%-CNDs and DPPH. As a summary, Illustration 2 depicts the discussed radical scavenging mechanisms of the P and B-doped CNDs and the enhanced scavenging capacity of High B%-CNDs.

**Figure 12. The UV-Vis Absorbance Spectra of DPPH Radicals (0.02 mg/mL) at Different Concentrations of CNDs for (a) E-CNDs, (b) Low P%, (c) High P%, (d) Low B%, (e) High P%, and (f) the Percentage of Anti-Oxidation Activities of CND Samples.**

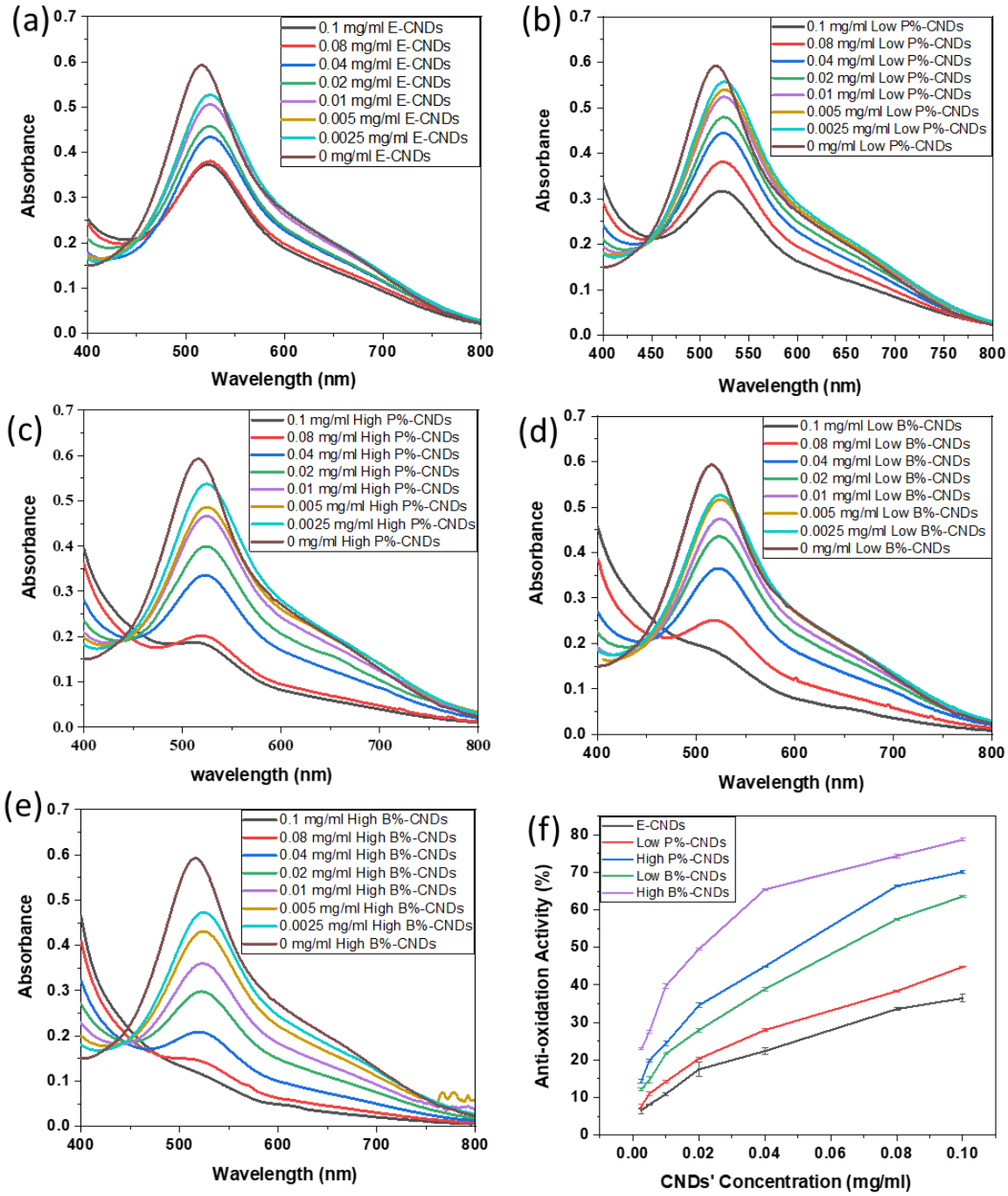

**Illustration 2. Proposed DPPH Radical Scavenging Mechanism for the P and B doped CNDs, and the Enhanced Scavenging Capability of High B%-CNDs.**

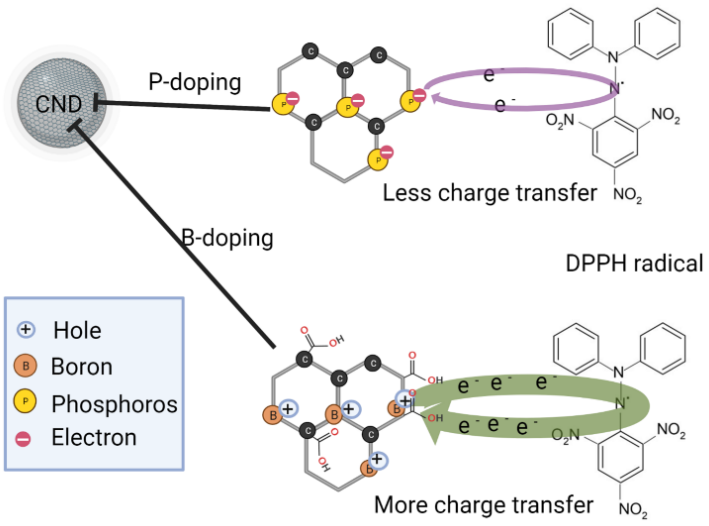


## Conclusion

This research focuses on the changes in optical characteristics of different CNDs with varied levels of P and B as dopant heteroatoms. Analysis of DLS, Raman, and XPS data combined with UV-Vis absorbance and fluorescence of the CNDs demonstrate that both P and B affected the optoelectronic properties of CNDs, albeit in different respects. XPS results showed that P, although in trace quantities, showed a higher penetration ability into the carbonic core of CNDs. In contrast, B predominantly formed chemical bonds at the surfaces of CNDs, and it was only after raising the B level that additional chemical bonds involving the carbonic core were likely developed. The findings were further confirmed by Raman data analysis, which showed that the $I_D/I_G$ for High P%-CNDs was greater than that of High B%-CNDs. In terms of the band-gap analysis, however, High P%-CNDs turned out unexpectedly to be larger than the other CNDs. This result was attributed to the presence of C═O chemical bond, which may intensify n–π* transitions

and thus increase the band-gap energy. Further deconvolution of the fluorescence spectrum found that the dominant emission originating from the carbogenic core of High P%-CNDs was more significant than that in High B%-CNDs. In conclusion, the P dopant as an n-type donor can boost the fluorescence of CNDs by influencing the carbonic core and electron-hole radiative recombination, while the B dopant as a p-type donor can improve the fluorescence by more significant interference to the surface functional groups of more emissive trap states. The DPPH radical scavenging study suggests that B dopant had a greater influence on the scavenging capability of CNDs than P dopant, most likely due to more O–C═O bonds and fewer C–C bonds in High B% CNDs, which promotes favorable charge transfer between the CNDs and DPPH. This research may offer guidance in designing the structures of CNDs in the core and surface functional groups as an effective method for tuning their optoelectronic properties for photoluminescence and anti-oxidation applications.

# CHAPTER IV: EFFECT OF CARBON NANODOTS DOPED WITH DIFFERENT HETEROATOMS ON THE OXIDATIVE STRESS IN CELLS AND THE PATTERN OF THE OXIDATIVE STRESS-RELATED GENE'S EXPRESSION

## Overview

Oxidative stress is associated with the occurrence and development of a wide range of human diseases. The development of methodologies to alleviate oxidative stress-mediated diseases could be beneficial in a medical context. This study aimed to evaluate the impact of two types of CNDs—doped with N, P, and B—on the oxidative stress and antioxidant-related gene expression patterns in two different human cell lines, EA.hy926 and A549 cells. The results from reactive oxygen species (ROS) scavenging experiments in wet chemistry showed that the NP-CNDs and NB-CNDs could reduce the ROS levels by up to 20 and 30%, respectively. The DCFH-DA ROS measurement assay showed that in EA.hy926 cells, none of these CNDs could induce ROS levels. However, in A549 cells a significant ROS induction was observed after CNDs treatment. On the other hand, the expression of three antioxidant genes, GSTP1, PON1, and GPx3, was examined both before and after cells were exposed to CNDs. The RT-qPCR results demonstrated that both CNDs downregulated the expression of selected genes in EA.hy926 cells. In A549 cells, both CNDs caused a highly significant upregulation in PON1 expression. Despite the non-toxicity and the lack of ROS induction in EA.hy926 cells after the treatment with both CNDs, our results from the genetic study suggest cancer's early stages seem to be mimicked upon the exposure of both CNDs to healthy cells.

## Introduction

Different cellular processes and environmental stimuli can lead to the production of reactive oxygen species (ROS) which may result in oxidative stress in extreme and unbalanced scenarios [196]. Excessive storage of ROS is a hallmark of numerous illnesses, including chronic inflammation, diabetes, neurodegeneration, and cancer [123], [132].

Carbon nanodots (CNDs), as zero-dimensional carbon nanomaterials, have garnered considerable interest among researchers due to their strong fluorescence, anti-oxidation properties, and biosafety for use in biological applications [7], [197].

Numerous studies have evaluated the oxidative stress effects of various types of CNDs—with different functional groups and dopant heteroatoms—in cells. Engagement of CNDs in the metabolic pathways of oxidative stress in cells could manifest as either antioxidant [114], [198], or pro-oxidant [115] effects. Notably, these characteristics of CNDs have been shown to aid the therapeutic strategies for cancer and neurological disorders, which are strongly related to cellular oxidative stress [137], [138], [140]. It has also been demonstrated that CNDs could impact the genetic materials of the cells by entering the nucleus [130]. Das et al.(2022) showed the downregulation effect of biomass-derived CNDs on the ROS-scavenging enzyme gene expressions (superoxide dismutase, glutathione peroxidase, and NADPH quinone oxidoreductase) both *in-vitro* and *in-vivo* [130]. Belperain et al. (2021) explored the capability of CNDs to reduce Tumor necrosis factor alpha (TNF-α)-induced inflammation in human microvascular endothelial cells [102]. They studied the expression of pro-inflammatory genes including Interleukin-8 (IL-8), interleukin 1 beta (IL-1β), ICAM, and MCP1 after treating with non-toxic doses of N-doped CNDs. They concluded that CNDs could suppress the production of the above-mentioned pro-inflammatory genes, particularly (IL-8) and (IL-1).

Numerous enzymes have been identified that can convert ROS into non-toxic moieties to reduce oxidative stress [199]. Paraoxonase-1 (PON1) enzyme exhibits cardiovascular disease protection characteristics via the decomposition of hydrogen peroxide and lipid peroxides [200]. Although PON1 gene expression predominantly occurs in the liver, this enzyme can be transported to other tissues such as the endothelium lining of the lungs, brain, and kidneys [201]. Glutathione S-transferase Pi (GSTP1) is a member of the glutathione-S transferase (GST) enzymes family which includes a set of isoenzymes that can contribute to oxidative stress and cancer via different functionalities. GSTP1 gene regulates oxidative stress and cell signaling, and also defends cells against carcinogens, oxidants, and electrophilic genomic damages [202], [203] which is expressed in most tissues including the lung, helping normal and cancer lung cells remove carcinogens and toxins as well [204]. Glutathione peroxidase (GPx) is regarded as one of the first line defense antioxidants in cells due to its ability to convert hydrogen peroxide to water and prevent lipid peroxidation [205]. GPx3, can eradicate all complex hydroperoxides among all known GPxs. In addition to its function in cytosol and mitochondria, it circulates in plasma [206]. Although GPx3 is predominantly expressed in the kidney, it is also present at lesser levels in other tissues, such as the lung [207].

In this study, we designed and synthesized three distinct CNDs co-doped with nitrogen (N), phosphorus (P), and boron (B) and assessed their effects on oxidative stress in human endothelium (EAhy.926) and lung epithelial (A549) cells. In addition, we have chosen the three aforementioned antioxidant genes (PON1, GSTP1, and GPx3) to investigate their expression pattern in the selected healthy and cancerous cells before and following treatment with two types of NP- and NB-CNDs. In some of the cell-based assays, N-CNDs were used as the basis of the

comparison. The results of this study could help elucidate the therapeutic potential of co-doped CNDs as highly fluorescent agents in the treatment of disorders associated with oxidative stress.

## Experimental

### Synthesis of CNDs

Three types of CNDs including N-CNDs, NP-CNDs, and NB-CNDs, were synthesized using a one-step closed vessel microwave synthesis method. Citric acid, ethylenediamine, phosphoric acid, and boric acid were used as the carbon, nitrogen, phosphorus, and boron sources, respectively. To synthesize NB-CNDs, a solution of 1 g citric acid, 1 mL ethylenediamine, 0.95 g boric acid, and 1 mL deionized water was transferred to a microwave synthesizer and heated at 180°C for 30 minutes at 100 psi and 300 Watt power. After centrifugation, dialysis, and freeze drying, a brown powder was obtained, which can be stored at room temperature. The same procedure was used for NP-CNDs synthesis, except for the use of 2 mL of phosphoric acid as the phosphorus source.

### CNDs Characterization

To investigate the structural and optical characteristics of CNDs, various characterization techniques were employed. A 0.002 mg/mL solution of each CND in deionized water was sonicated for 20 minutes, drop-cast on mica, and allowed drying. Afterward, the size was measured using Atomic Force Microscopy (AFM; Asylum MFP-3D Origin+). Fourier Transform Infrared Spectroscopy (FTIR; Varian 670) and X-ray photoelectron spectroscopy (XPS; Thermo Fisher ESCALAB 250Xi) were performed to analyze the formation of functional groups on the surface of CNDs and elemental data analysis, respectively. For XPS analysis, a solution of 10 mg/mL of all CND types was prepared, drop-casted, and dried. A 0.005 mg/mL of each CNDs type was used for surface charge measurement using a Zetasizer (Malvern Instruments Ltd.).

**Lucigenin Experiments**

A reaction mixture containing 0.1 mM of diethylenetriaminepentaacetic acid, 100 μM xanthine (99%, Aldrich), and 10 mM XO (grade I, Aldrich) was prepared in PBS. Then the mixture was split into a 96-well plate and different concentrations (0, 0.005, 0.02, 0.04, 0.08, and 0.1) of each CNDs type were added to the wells. As the enzymatic reaction initiator, 5 μL of lucigenin (5 μM) was added to each well. The plate was kept in a microplate reader (BioTek Synergy Mx) at 37 0C for 30 mins and the chemiluminescence was monitored to evaluate the superoxide scavenging capability of the CNDs.

**Cell Culture Procedure and Viability Assay**

Human endothelial cells (EA.hy926, ATCC, CRL-2922) and human lung epithelial cells (A549, ATCC CCL-185) were purchased from ATCC. DMEM (ATCC Cat# 30-2002), and F-12K (ATCC® 30-2004™) medium enriched with 1% streptomycin-penicillin (Fisher Scientific) and 10% fetal bovine serum (Sigma-Aldrich) were employed to culture the EA hy926 and A549 cells, respectively. Cells were cultured in T25 cell culture flasks at 37 °C, in a humidified incubator with 5% CO2. To determine the cytotoxicity of CNDs, the alamar blue cell viability assay was employed. In a 96-well plate, cells were plated at a density of $1*10^4$. Following 24 hours of incubation, the medium was discarded and 100 μL of CNDs of different doses were added to each well. Following 24 hours, each well received 10 μL of alamar blue reagent. The plate was kept for one hour in the incubator. The fluorescence was then measured using a plate reader ($\lambda_{ex}/\lambda_{em}$ at 560/580 nm).

### *In Vitro* ROS Scavenging Assay

Dichloro-dihydro-fluorescein diacetate (DCFH-DA) assay was used to evaluate the ROS scavenging capability of CNDs in cells. Briefly, cells were plated in a 96-wells plate with a density of $1*10^4$ and were incubated for 24 hours. Then, the media was removed, cells were treated with different concentrations of CNDs, and the plate was kept in the incubator for 24 hours. After 24 hours, cells were washed twice with PBS, and 100 μL of DCFH-DA was added to the cells (10 μM and 40 μM for EA.hy926 and A549 cells, respectively). Cells were incubated for 30 minutes and were washed twice with PBS. Afterward, the fluorescence was read using a plate reader ($\frac{\lambda_{ex}}{\lambda_{em}}$ at $\frac{485nm}{528nm}$). In parallel, wells with cells and CNDs were considered as the positive control. Cells with CNDs, DCFH-DA, and different concentrations of ascorbic acid (AA) were considered negative control.

### Glucose-Induced ROS Scavenging Capability of N, P-doped CNDs and N, B-doped CNDs

EA.hy926 cells were seeded in a 96-well plate and glucose in different concentrations (5, 15, and 50 mg/mL) was added to the wells and incubated with cells for 24 hours. Then, the DCFH-DA assay was conducted as described above. In the next experiment, a mixture of 15 mg/mL of glucose and different concentration of N-CNDs, NP-CNDs, NB-CNDs, and ascorbic acid was added to EA.hy926 cells and DCFH-DA experiment was carried out to monitor the changes in ROS levels.

### Cellular Uptake and Sub-Cellular Localization

In separate experiments, EAhy.926 and A549 cells were cultivated for 24 hours on glass coverslips in 12-well plates. Then cells were treated with NP-CNDs (0.1 mg/mL) and NB-CNDs (0.1 mg/mL). After 24 hours, cells were washed twice with PBS and were fixed using Paraformaldehyde 4% (Alfa Aesar) for 30 mins at room temperature. MitoTracker Red CMXRos

(0.1 μM, 10 min, 37 °C, Molecular Probes, $\lambda_{ex}/\lambda_{em}$ at 579/599 nm, Fisher Scientific) was used to stain the mitochondria. Using a fluorescence confocal microscope (Zeiss Z1 Spinning Disk Confocal), Cellular uptake and Sub-cellular localization of CNDs were investigated. ROHD and DAPI channels were used for mitochondria and CNDs imaging, respectively.

**RNA Extraction, cDNA Synthesis, and Quantitative Real-Time PCR**

Total RNA was extracted from the cultured cells including non-treated control cells and treated cells with 0.005 or 0.1 mg/ml of NP-CNDs or NB-CNDs using Monarch Total RNA Miniprep Kit (NEB #T2010S) according to manufacturer's instructions. The quantity and purity of the extracted RNAs were assessed using spectrophotometric measurement (NanoDrop™; Thermo Scientific 2000). Pure RNA should have OD260/280 and OD260/230 ratios above 1.8 to 2.2. The quality of the RNAs was checked by running 1% agarose gel electrophoresis. Extracted RNA reverse transcribed to cDNA using SuperScript™ IV First-Strand Synthesis system kit (Invitrogen™ #18091050) by adding oligo d(T)20 and random hexamer primers according to the kit instructions. Quantitative real-time PCR was performed for the genes of interest (GSTP1, PON1, and $GP_X3$) and TATA box-binding protein (TBP) as the housekeeping gene using Maxima SYBR Green/ROX qPCR Master Mix (2X) (Thermo Scientific™, #K0252) kit using the Applied Biosystem (7500 Fast Real-Time PCR System) thermal cycler. Primer pairs for the genes of interest were designed specifically for mRNA using AlleleID version 7.5 software (PREMIER Biosoft, Palo Alto, CA, USA). Primers for TBP amplifications were borrowed from a reference [208]. Detailed information on the primers is listed in Table 6. The amplification thermal program included enzyme activation at 95°C for 10 minutes followed by 40 cycles of denaturation at 95°C for 15 seconds and annealing/extension at 60°C for 60 seconds. Melting curve analysis was performed by ramping from 75-95°C with +1°C/cycle to confirm the accuracy of the PCR reaction.

RT-negative reactions and non-template control (NTC) reactions were run as two negative controls in each round of real-time PCR. The relative expression of mRNA for the genes of interest was calculated using the $2^{-\Delta\Delta Ct}$ method.

**Table 6. Primer Sequences, Annealing Temperatures, and Amplicon Sizes.**

| Primer name | sequence 5' to 3' | $T_a$* | Product size (bp) |
|---|---|---|---|
| GSTP-F | AAGCCTCCTGCCTATACGG | 63.4 | 116 |
| GSTP-R | GTCCTTCCCATAGAGCCCA | | |
| PON1-F | CCAGTCTTCTTACCAAACAC | 57.1 | 126 |
| PON1-R | AGTCCATTAGGCAGTATCTC | | |
| GPX3-F | CCGCCAGATGGGCAATCCC | 61.8 | 76 |
| GPX3-R | GGTGAGGGCTCCGTACTCG | | |
| TBP-F | CCCGAAACGCCGAATATAATC | 60.4 | 134 |
| TBP-R | TCTGGACTGTTCTTCACTCTTG | | |

* $T_a$: annealing temperature

### Statistical Analysis

Data presented are means ± standard error (SE) of at least three independent experiments ($n = 3$). The statistical analyses between groups were performed using a one-way analysis of variance (ANOVA). Statistical analysis was conducted using GraphPad Prism version 8.2.1 for windows. A probability of $P < 0.05$ was considered statistically significant.

## Results and Discussions

### Synthesis and Characterization of CNDs

N-CNDs, NP-CNDs, and NB-CNDs were synthesized using a closed-vessel microwave synthesis method. AFM results showed that all CND particles were spherical with an average size of 2.6 ± 0.14 nm, 0.8 ± 0.05 nm, and 0.77 ± 0.04 nm for N-CNDs, NP-CNDs, and NB-CNDs, respectively (Figure S2.1). The zeta potential ($\zeta$) for N-CNDs, NP-CNDs, and NB-CNDs was

found as -29.7 ± 1.1, -13 ± 3, and -34.5 ± 1.2 mV, respectively (Figure S2.2). Based on the FTIR spectra (Figure 13a), formation of the COOH group is confirmed in all CNDs due to the presence of C═O stretch at 1650 $cm^{-1}$ and the O–H stretch at 3100 $cm^{-1}$ [134]. The peak around 1550 $cm^{-1}$ can be assigned to C═C of the graphitic structure of CNDs core [70]. In all CNDs, the amine N–H bonds appeared around 3300-3350 $cm^{-1}$. The peaks at 1040 and 2330 $cm^{-1}$ in NP-CNDs correspond to P–$H_2$ and P–H bonds, respectively [161]. In NB-CNDS, the bands at 1000 $cm^{-1}$ correspond to B–C chemical bonds, whereas the bands at 3268 $cm^{-1}$ correspond to B–OH chemical bonds [175]. Figure S2.3 represents the full XPS survey results for all CND samples and Table S2.1 summarizes the XPS data analysis for the breakdown atomic percentage of P and B for each CND sample.

The UV-Vis absorbance spectra of all CNDs (0.025 mg/mL) are presented in Figure 13a, with a shoulder near 240 nm related to π–π* transitions of C═C bonds and a broad peak near 345 nm, attributed to n–π* transitions of non-binding orbitals mostly belonging to C═O bonds [116].

Multiple excitation wavelengths were used to analyze the CND samples' fluorescence spectra (Figure 13a). In all samples, fluorescence emission was maximum at the excitation wavelength 360 nm, and the highest fluorescence intensity belongs to NB-CNDs.

**Figure 13. FTIR (a), and UV-Vis Absorbance (b) Spectra of all CNDs. Fluorescence Spectrum of N-CNDs (c), NP-CNDs (d), and NB-CNDs (e).**

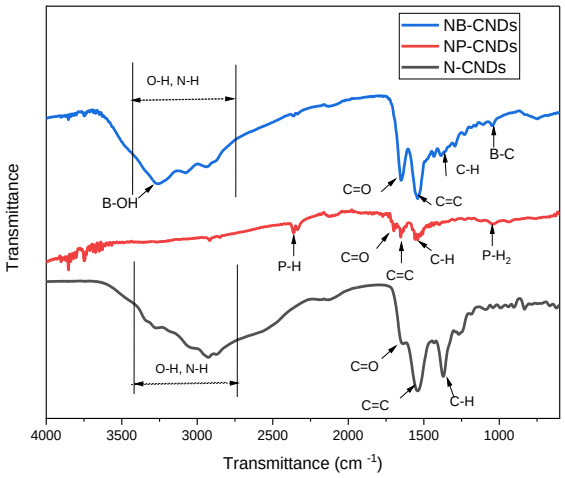


(a)

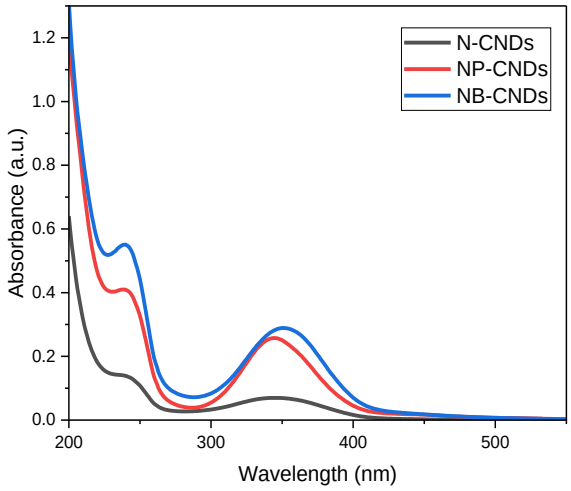


(b)

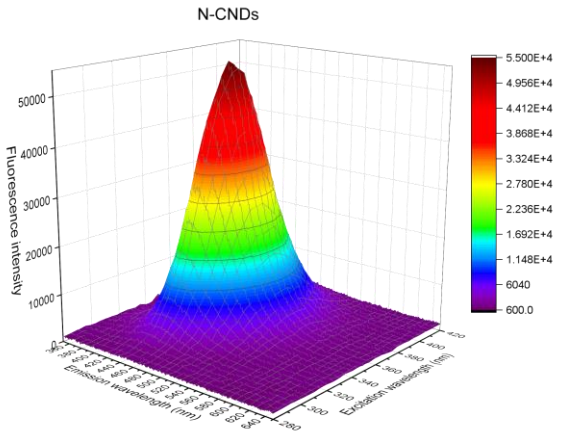


(c)

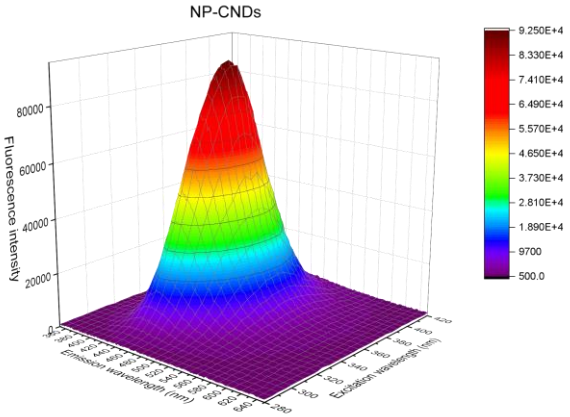


(d)

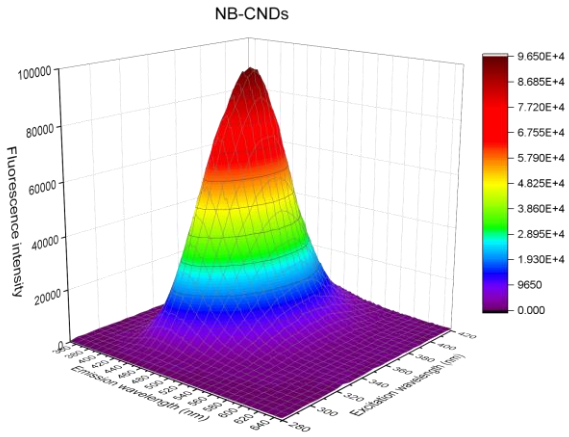


(e)

**Lucigenin Assay Results**

As an acridine-based chemiluminescence probe, lucigenin has been widely used for monitoring superoxide formation [209]. Lucigenin chemiluminescence assay is designed and frequently employed in biological and enzyme assays for *in vitro* and in vivo superoxide detection [117]. In this assay, xanthine oxidase is used as a source for the production of ROS in the system. Adding varying concentrations of CNDs to the reaction mixture allows us to assess the ROS scavenging capabilities of CNDs. The results reveal that the detected levels of reactive oxygen species (ROS) decrease when the concentrations of both NP-CNDs and NB-CNDs increase Figure 14a. The ROS scavenging capability(%) for NB and NP-CNDs was found to be ~30% and ~20, respectively (Figure 14b).

**Figure 14. Lucigenin-Derived Chemiluminescence After Exposure to Different Concentrations of NP- and NB-CNDs Measured by Xanthine/XO System-Induced Lucigenin-CL (a), and Calculated Superoxide Scavenging Activity Versus CNDs' Concentration (b).**

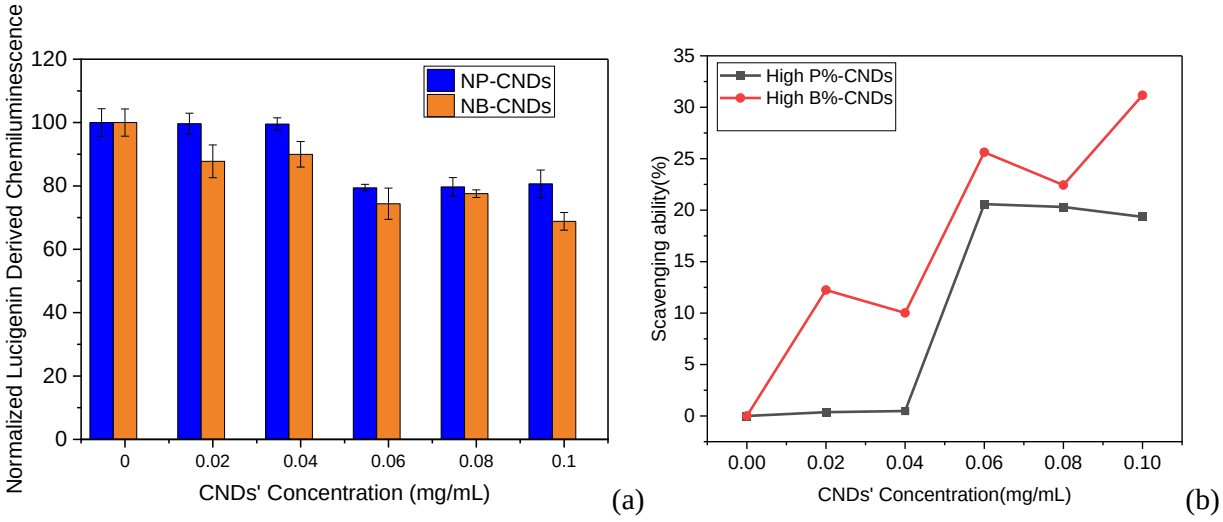

**Cell Viability Results**

Two distinct CND concentration ranges were compared and selected to estimate the safe range of CNDs for future applications: a lower range (0, 0.005, 0.01, 0.02, 0.04, and 0.08 mg/mL) and a higher range (0, 0.1, 0.5, and 0.8 mg/mL). Figure 15a,b, and Figure 15c,d represents the alamar blue assay results for EA.hy926 and A549 cells at the above-mentioned ranges of CNDs, respectively. No significant decrease in the viability of EA.hy926 cells was found following treatment with any of the three forms of CNDs. The same results were observed for the A549 cells. The higher concentration range of N-CNDs and NB-CNDs was found to significantly reduce the viability of A549 cells. NP-CNDs had the same effect only at the concentration of 0.8 mg/mL. When exposed to NB-CNDs at concentrations of 0.5 and 0.8 mg/mL, EA.hy926 cell viability was significantly reduced.

**Figure 15. Viability of EA.hy926 Cells (a, b), and A549 Cells (c, d) After 24-h Exposure to Different Concentrations of CNDs Evaluated by Alamar Blue Assay.**

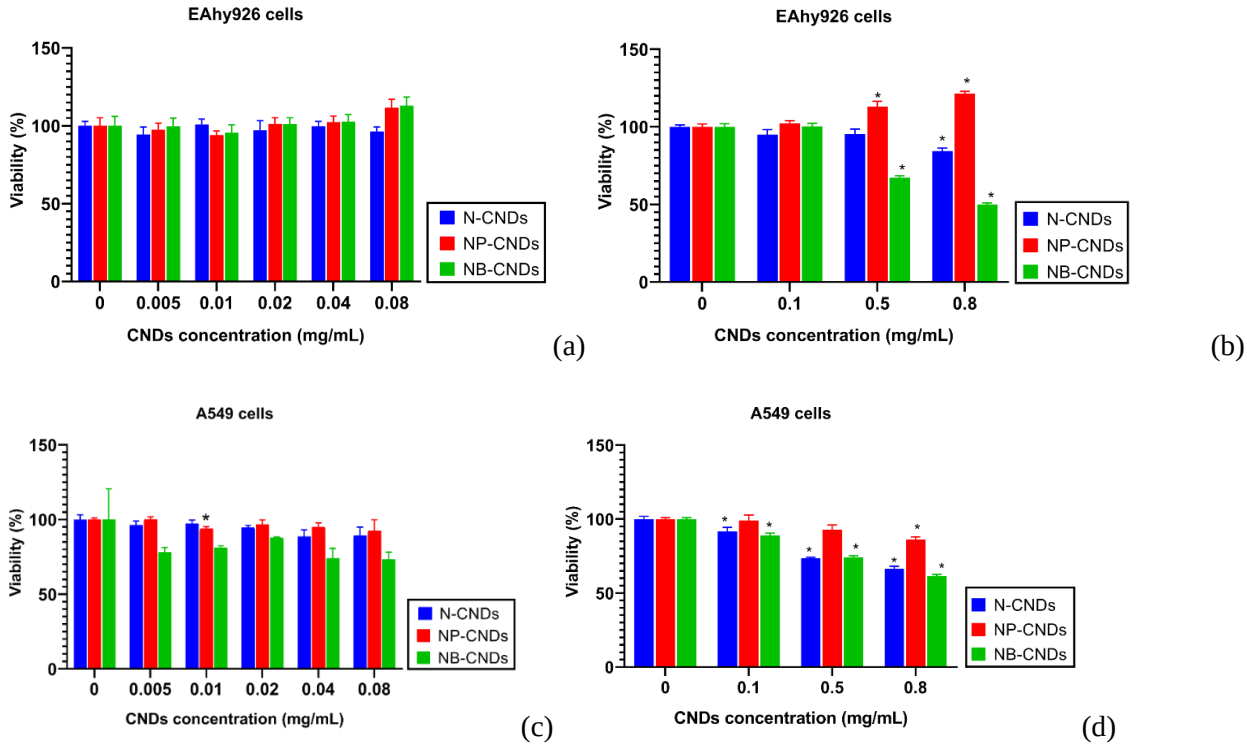

**DCFH-DA Assay Results**

In our study, we investigated whether the CNDs with differently doped heteroatoms could be considered anti/prooxidant agents with anticancer therapeutic capabilities. Here, we employed two different types of CNDs doped with N, P, and B (NP- and NB-CNDs) which in our previous studies performed as highly radical scavengers in chemical reactions. We intended to extend our knowledge of these CNDs' oxidative stress effects in cells and evaluate their potential therapeutic capabilities in terms of contributing to ROS effects in A549 cells as cancerous cells. Simultaneously, we conducted the same experiments in EA.hy926 cells to understand the same effects on healthy cells. N-CNDs were considered only for comparison purposes and evaluation of the P and B doping effects. The DCFH-DA assay is a commonly used method to measure the level of ROS in cells [210]. In this assay, cells are treated with the non-fluorescent probe DCFH-DA, which is converted into the highly fluorescent molecule 2',7'-dichlorofluorescein (DCF) in the presence of ROS. The fluorescence intensity of DCF is proportional to the amount of ROS in the cells and can be used to quantify oxidative stress. The DCFH-DA assay outcomes for both cell lines are shown in Figure 16. There was no increase in ROS levels in EA.hy926 cells following treatment with any of the CNDs (except for 0.02 mg/mL of NP-CNDs) and AA. In A549 cells, the levels of detected ROS increased with the NP-CNDs treatment (with a small fluctuation), while significantly elevated after NB-CNDs treatment. Overall, a significant increase in ROS amounts is observed in the case of A459 cells with co-doped CNDs treatment. A decrease in ROS level was observed in the A549 cells after treatment with AA.

**Figure 16. Effects of CNDs on Intracellular ROS Generation in EA.hy926 (a), and A549 Cells (b) Treated with CNDs and AA for 24 h, Monitored by the Addition of DCFH-DA Probe.**

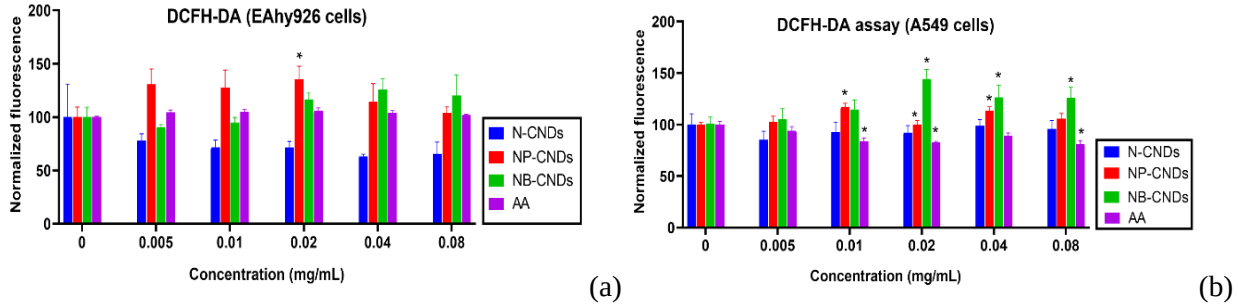


(a) (b)

**Glucose-Induced ROS Scavenging Capability of NP-CNDs and NB-CNDs**

It has been shown that high levels of glucose in healthy cells can induce ROS production [211], [212]. EAhy.926 cells were incubated with different levels of glucose and as can be seen in Figure 17a, the detected ROS levels in cells were increased with the increment of incubated glucose. In the next experiments, CNDs were added to cells along with 15 mg/mL of glucose to determine whether any of the CNDs could diminish the glucose-induced ROS levels. As shown in Figure 17b, both NP-CNDs and NB-CNDs could inhibit the glucose-induced production of ROS. Surprisingly, with the same concentration range, Ascorbic acid (used as control) did not show superior ROS scavenging characteristics. The inhibitory effect of NP and NB-CNDs has started to manifest at the concentration of 0.08 mg/mL. At the same concentration of AA, a significant increase is observed in detected ROS quantities. Incubation with N-CNDs did not result in any significant changes in ROS levels.

**Figure 17. Effects of Different Concentrations of Glucose on Intracellular ROS Generation in EA.hy926 Cells (a), and Effects of Different Concentrations of CNDs and AA on Intracellular Glucose-Induced ROS Generation in EA.hy926 Cells(b) Monitored by the Addition of DCFH-DA Probe.**

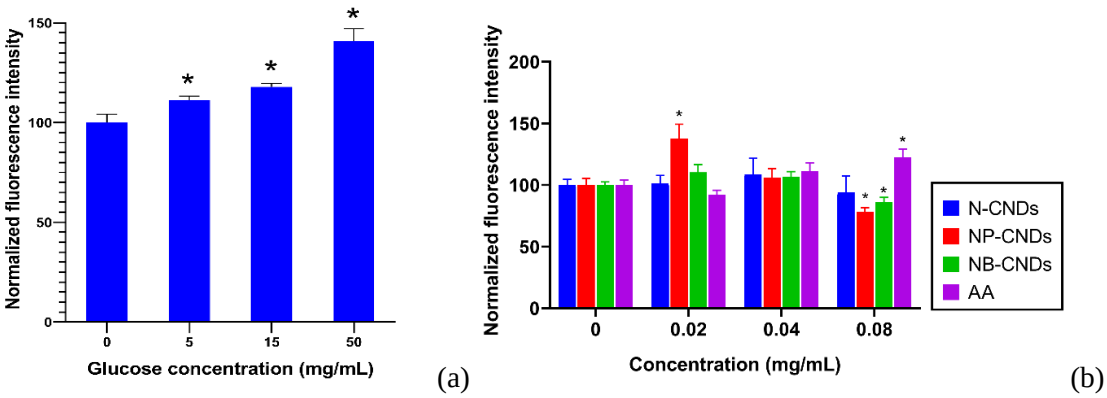


## Cellular Uptake and Sub-Cellular Localization

Despite the undesirable interaction between the negatively charged nanoparticles and the negatively charged cell membrane, it has been found that negatively charged nanoparticles can be taken in by cells [213]. According to research, probable oxidative stress to the cell membrane —caused by the presence of nanoparticles— can drastically reduce the number of negative ions on the surface of the cells [214], resulting in more uptake of negatively charged particles by cells. CNDs can target various organelles in the cells including the nucleus, mitochondria, lysosomes, endoplasmic reticulum, or remaining in the cytoplasm [30], [80]. Based on characterization results, both NB-CNDs and NP-CNDs exhibit high fluorescence, allowing the internalization of CNDs into cells to be monitored using a confocal microscope under the DAPI channel. As shown in Figure 18a–d both CNDs could internalize and localize in the mitochondria and nucleus of both cells. These results show that NP-CNDs and NB-CNDs both can get involved in the respiratory transfer chain in the mitochondria through which they can cause oxidative stress effects. They also

could enter the nucleus and interact with the cells' genomic materials. On the other hand, their localization in the nucleus makes them promising candidates for gene delivery purposes regarding their higher fluorescence as well.

**Figure 18. Subcellular Localization of NP-CNDs in EA.hy926 Cells (a) NB-CNDs in EA.hy926 Cells (b), NP-CNDs in A549 Cells (c), and NB-CNDs in A549 Cells(d); All CNDs were used at the Concentration of 0.1 mg/mL.**

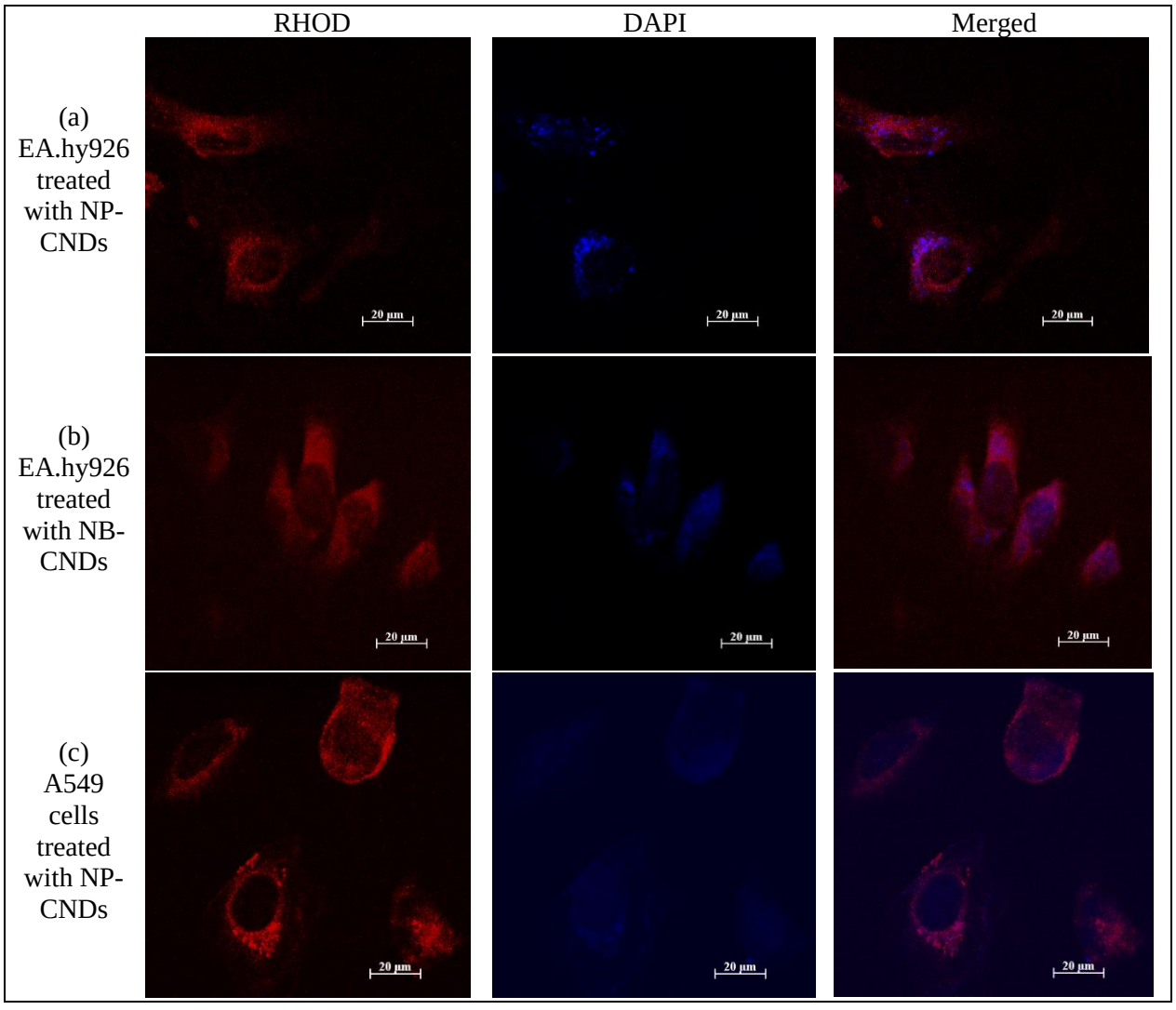

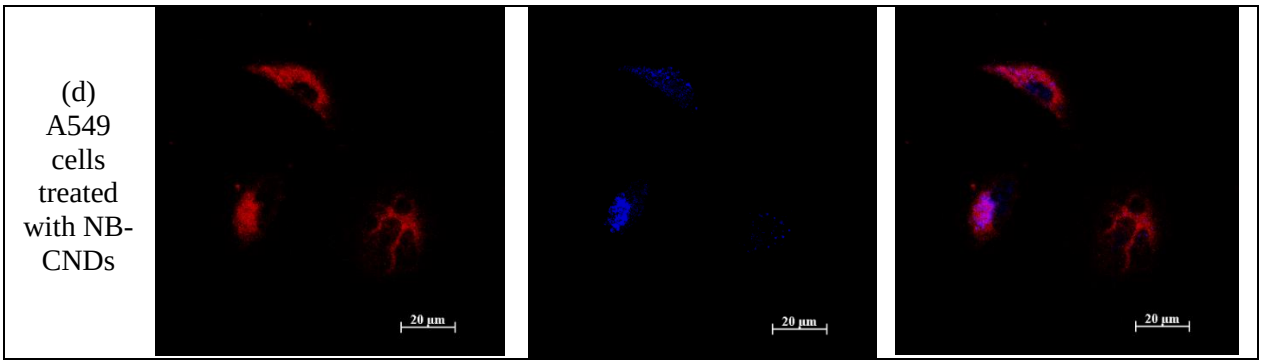


**Antioxidant Gene Expression Studies**

Cancer is a multifactorial disease resulting from complex molecular and cellular changes interacting with non-genetic factors [215]. Oxidative stress (OS) is a major pathological pathway contributing to the development of many human conditions such as kidney diseases [216], autoimmune diseases [217], cardiovascular diseases [102], and cancers [111]. An excessive generation or deficient scavenging of ROS in cells leads to oxidative stress with the potential for oxidative damage to DNA, proteins, and lipids. Endogenously, ROS are generated in response to inflammatory or infectious agents, immune cell activation, stress, or as by-products of cellular respiration. However, exposure to radiation, air pollution substances, heavy metals, and specific drugs or chemicals are the exogenous sources of ROS generation [218]. The increased ROS in vivo shows dual functions, given that, plays a role as tumor suppressive or tumor promotive. High levels of ROS may recruit intracellular signaling pathways to promote cell proliferation and suppress apoptosis, and chromatin remodeling by altering the expression of specific ROS-sensitive genes. These cells are prone to initiate cancer by producing pre-neoplastic lesions. On the other hand, elevated levels of ROS may induce apoptosis, autophagy, or necrosis to eliminate cancer cells. The latter is the basis for newly emerged pro-oxidant therapy for cancer treatment [121]. We selected two different doses of each CNDs within the safe cytotoxicity range for the treatment of healthy cells. To determine whether carbon nanodots influence the oxidative stress pathway, we

evaluated the mRNA levels of the three antioxidant enzyme genes (GSTP, PON1, and GPX3) before and after treating cells with low dose (0.005 mg/mL) and high dose (0.1 mg/mL) of CNDs in separate reactions. As shown in Figure 19a, the treatment of healthy cells with a high concentration of NB-CNDs resulted in the downregulation of GSTP and PON1 genes. There is no statistically significant alteration in the gene expression in the treatment group with a low concentration of NB-CNDs. Regarding the EA.hy926 cell line, three targeted genes (GSTP, PON1, and GPX3) were downregulated in response to the low concentration of NP-CNDs Figure 19b. However, expression levels of the genes in response to high concentrations of NP-CNDs did not differ between groups. PON1 expression is upregulated in A549 cells in reaction to high concentrations of NB-CND, while there is no significant change in response to low concentrations of NB-CND (Figure 19c). On the other hand, overexpression of the PON1 gene in response to both low and high concentrations of the NP-CND was observed in A549 cells (Figure 19d). After treatment with various quantities of NB-CNDs and NP-CNDs, neither GSTP1 nor $GP_{X3}$ mRNA levels were significantly altered in A549 cells.

**Figure 19. The RT-qPCR Results Representing the Selected Gene's Expression Level in EA.hy926 Cells after Treatment with NB-CNDs (a), EA.hy926 Cells after Treatment with NP-CNDs (b), A549 Cells after Treatment with NB-CNDs (c), and A549 Cells after Treatment with NP-CNDs (d).**

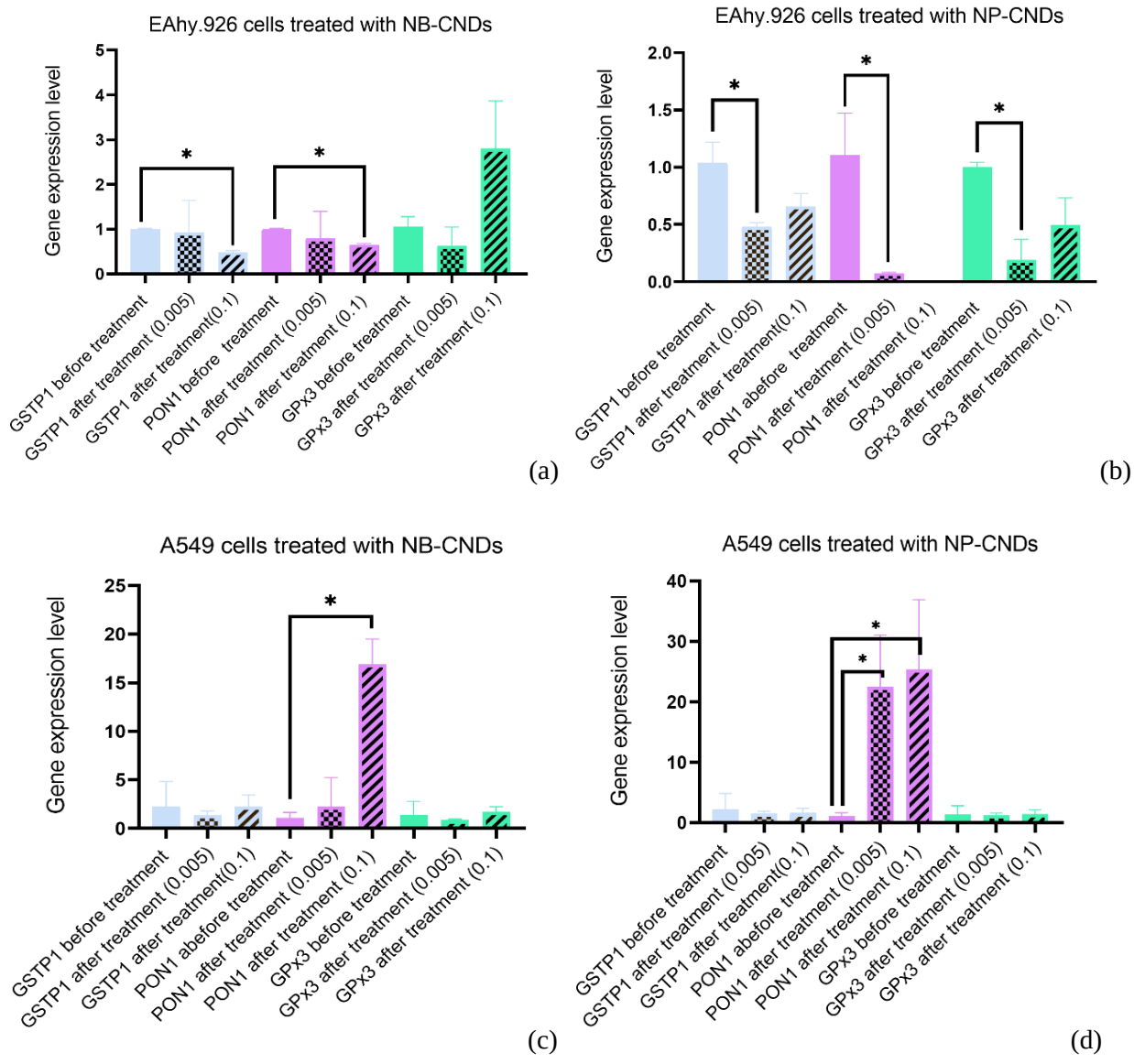


High throughput whole genome gene expression analysis in human embryonic lung fibroblast has revealed the effect of negatively charged carbon dots on cell proliferation, apoptosis, oxidative stress, and cell cycle pathways by deregulation of the related genes [219]. The number

of differentially expressed genes responding to negatively charged carbon dots proportionally increases by exposure time and dose [130]. Based on our results, in the A549 lung cancer cell line, PON1 was the only gene overexpressed following treatment with CNDs. Comparative analysis showed higher mRNA levels of PON1 in the A549 cell line than in EAhy.926 cells after treatment with CNDs. Aldonza et al. have shown the potential of PON1 as a biomarker for lung cancer and they reported the same results for PON1 expression in both mRNA and protein levels in the lung epithelial cell line (L132) and in some lung cancer cell lines such as A549 and H358 [220]. The overexpression of PON1 in lung cancer cells contributes to oncogenesis by inducing cell proliferation, and colony expansion, and decreasing the G1/S ratio, quick proliferation index in cancer cells [221], and cellular senescence [220]. In our study, the DCFH-DA assay accounted for a significantly higher amount of ROS in the A549 cells which is supposed to inductive oxidative stress effects of CNDs. The cancer cells, in turn, increase the expression of the PON1 gene as an adaptive response mechanism to oxidative stress (Illustration 3a). If considering PON1 overexpression as a kind of forced gene expression alteration, both prooxidant and antioxidant activity would be expected from the PON1 gene. As an antioxidant activity, PON1 involves in the superoxide ion scavenging in the cell or induces the production of hydrogen peroxide to exert its prooxidant activity [220]. Taken together, increased ROS generation, overexpression of PON1, and low cell viability in the A549 lung cancer cells treated with NB-CNDs strengthen the probable prooxidant activity of these CNDs in cancer therapy. However, it is hard to explain cellular death from the molecular perspective in exposure to CNDs. Contrary to previous studies that mentioned the overall reduced apoptosis in PON1 overexpressed cancer cells, here we observed lower viability. On the other hand, after NP-CNDs treatment in A549 cells, overexpression of PON1 seems to suppress caspase 3 and 7 to inhibit apoptosis and involve tumor survival [220].

**Illustration 3. Proposed Mechanism Representing the Probable Pathway of CNDs' Oxidative Stress Effects on the Selected Antioxidant Genes Expression in A549 Cells (a), and EA.hy926 Cells (b).**

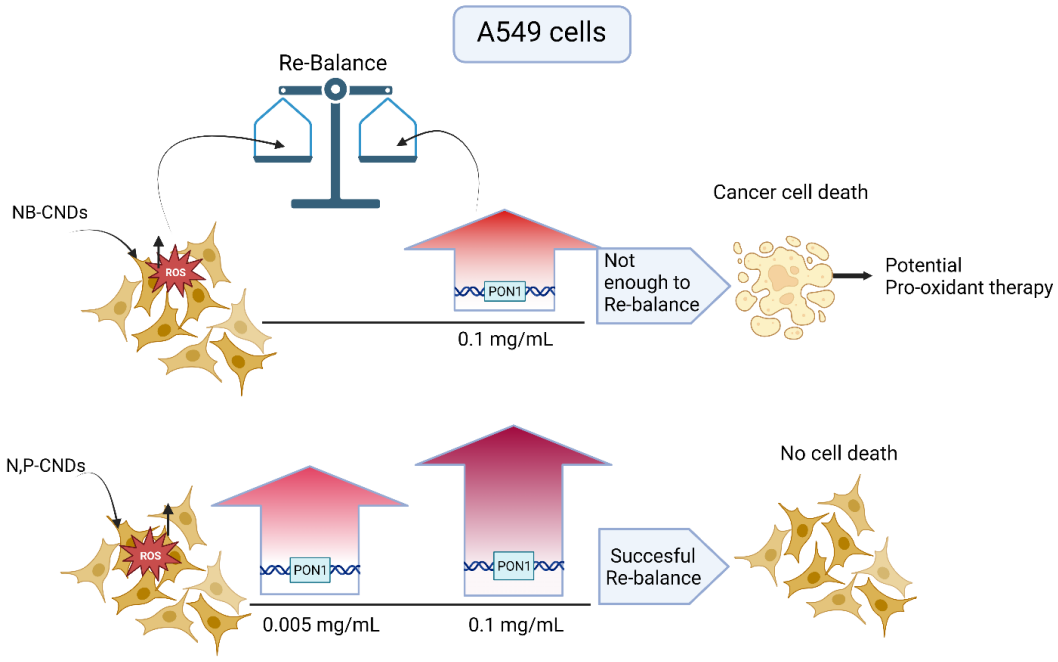


(a)

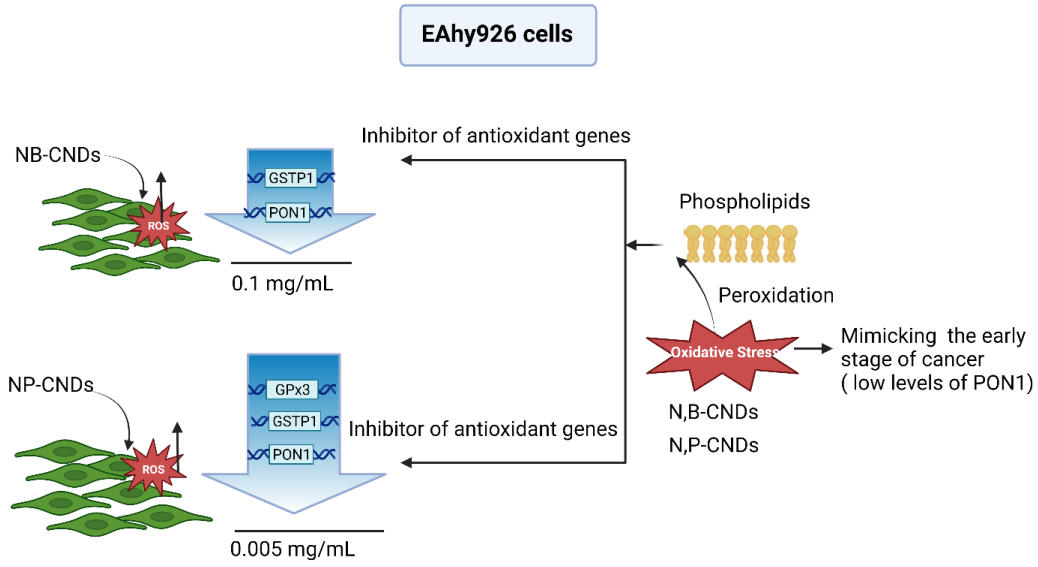


(b)

On the other hand, the discussion on the observation from the same experiment sets on the EA.hy926 cells is different (Illustration 3b). This decrease in PON1 level may be the result of lipid

peroxidation caused by oxidative stress, which inhibits PON1 expression [222], [223]. The expression and activity of the PON1 gene and its products have been implicated in the development and progression of several types of cancer [224]. PON1 and aryl esterase are esterase enzymes with antioxidant properties that are found in human serum. It has been shown that serum PON1 levels were lower in patients with newly diagnosed lung cancer, according to research. Since the antioxidant gene expression in Ea.hy926 cells decreased following incubation with both CNDs, we may be able to conclude that both CNDs with prooxidant properties triggered lipoprotein peroxidation, which in turn inhibits PON1 expression. It might be concluded that these CNDs are mimicking the early stages of cancer in which genetic alteration starts to occur [222]. However, despite the downregulation of all three genes upon treatment with both CNDs, EA.hy926 cells did not undergo apoptosis. This may be because non-enzymatic mechanisms are functioning and can regulate the ROS overload in these cells. The decline in antioxidant enzymes is likely insufficient to render this ROS generation effective for cell death. The other reason might be due to the exposure time which was only 24 hours and might not be long enough to cause any cell death yet.

## Conclusion

In this study, the oxidative stress impact of two co-doped CNDs in EA.hy926 and A549 cells was investigated. The results from chemical reactions showed the radical scavenging capabilities of NP- and NB-CNDs using the lucigenin chemiluminescence assay. At the cell level, no oxidative stress effect was observed in healthy cells, but a significant increase was observed in cancer cells after incubation with CNDs. At the genetic level, however, the results were more complicated to discuss. In cancer cells, the high association of PON1 gene expression was confirmed by a significant upregulation after treatment with CNDs. This upregulation was justified by the fact that in cancer cells, both CNDs have inducted the generation of ROS, from which there

might have been an imbalance in the ROS levels in cells. To dominate this change, the cells have increased the expression of PON1 which in the case of NB-CNDs was not enough and caused cancer cell death(at the dose of 0.1 mg/mL). However, in the case of NP-CNDs, this endeavor for re-balancing the ROS levels seems to be successful so there was no cancer cell death at any of the employed doses. Antioxidant genes can also regulate signaling pathways that are involved in the regulation of autophagy. For example, oxidative stress can activate the AMP-activated protein kinase (AMPK), which then stimulates autophagy [225]. On the other hand, both CNDs in healthy cells caused a significant downregulation in the antioxidant genes. Despite no cell death observation, this downregulation could be described as a sign of early stages of cancer. That means even with the anticipated prooxidant therapy capabilities for NB-CNDs, there should be optimization of the experiment parameters to avoid the toxic effects in healthy cells. This might result in designing improved CNDs for safer biological applications. Understanding these pathways can lead to designing CNDs with strong targeting abilities, which will be helpful in the treatment of organelle-related oxidative stress defects such as mitochondrial problems in cancer.

# CHAPTER V: HIGHLY FLUORESCENT N, B-DOPED CNDS PERFORMING AS $FE^{2+}$ DETECTION TURN-OFF SENSORS

## Overview

Fluorescent probes are valuable tools for determining the subcellular concentrations of $Fe^{2+}$ ions in water and living cells. Co-doped carbon nanodots (CNDs) have demonstrated the capacity to optically detect a wide variety of targets, including metal ions. In this work, the quenching of highly fluorescent N, B-doped CNDs by $Fe^{2+}$ ions were employed to detect $Fe^{2+}$ in water samples and live cells. The fluorescence of CNDs was quenched in a concentration-dependent pattern, and CNDs show high selectivity towards $Fe^{2+}$ ions relative to other metal ions within the first 30 seconds of the reaction. The limit of detection (LOD) was calculated as 1.8 nM and the linear response range was 7 nM to 1 μM. The recovery percentage was determined to be 97%, 101%, and 103% for spiked $Fe^{2+}$ concentrations of 31, 125, and 1000 nM, respectively. CNDs were able to monitor the presence of $Fe^{2+}$ in living cells during the optical imaging sensing of $Fe^{2+}$ ions, and the quenching in cells was almost completed within one hour. To discuss the quenching mechanism, the photoinduced electron transfer (PET) procedure is proposed. Overall, as sensors for the detection of $Fe^{2+}$ in both water samples and living cells, N, B-doped CNDs demonstrated a satisfactory level of sensitivity and selectivity.

## Introduction

Metal ion detection is essential in a variety of scientific disciplines, including water treatment, medicine, ecology, and chemistry [226]. Determining the concentration levels of heavy metals and evaluating their health issues is vital in safeguarding potable water quality [38]. Iron concentration in municipal water is regulated to 0.3 mg/L by U.S. regulations [227] and the world health organization [228]. Numerous biological activities in the body need iron in different oxidation states ($Fe^{2+}$ and $Fe^{3+}$), including energy generation, oxygen delivery, DNA synthesis, etc. [229]. $Fe^{2+}$ has been known as an essential nutrient for many cellular processes, and changes in its levels can disrupt cellular homeostasis and lead to disease [8]. This ion also participates in redox reactions and contributes to oxidative stress in cells [9], therefore monitoring $Fe^{2+}$ levels can help understand the toxic mechanisms of these compounds and aid in the development of potential therapeutic strategies [10]. So far, many traditional techniques such as atomic absorption/emission spectrometry, ion chromatography, calorimetry, inductively-coupled plasma spectrometry, and spectrophotometry, have been applied to identify metal ions [39]. However, many of these detection methods—although possessing high sensitivity and accuracy—rely on the utilization of complex sample preparation and instrumentation [230].

Among emerging detection methods, "On-Off" fluorescence-based probes have gained the interest of researchers due to their facile synthesis, excellent selectivity, and sensitivity towards ions detection [231], [232], including $Fe^{2+}$ and $Fe^{3+}$ [229], [233]. To this end, CNDs have recently been identified as an ideal candidate for ion detection [234], [235]. Radhakrishnan et al., have synthesized surface-passivated fluorescent carbon quantum dots to use them as promising turn-off fluorescence sensors for the detection of multiple analytes [236]. These surface-passivated CNDs were able to detect $Cu^{2+}$, $Pb^{2+}$, and $Fe^{3+}$ ions in aqueous systems owing to their different binding

abilities. CNDs have also been successfully used in $Fe^{3+}$ detection. For instance, Arvapalli et al. synthesized highly fluorescent N-doped CNDs for the detection of $Fe^{3+}$ in water, human plasma, and living cells [6]. The proposed mechanism was based on the charge transfer quenching between $Fe^{3+}$ and CNDs. Wei et al designed and synthesized non-functionalized carbon nanodots and employed them for the detection of $Fe^{2+}$ in water, bovine serum albumin, and live cells. In their sensor, the red fluorescence diminished after $Fe^{2+}$ interaction and the LOD turned out to be as low as 51 nM [237]. Nevertheless, reports on the detection of $Fe^{2+}$ due to its high oxidation potential are rare. Monitoring Fe2+ levels help understand the critical role of this metal ion in oxidative stress-related diseases and informs potential therapeutic strategies [238], [239].

This work investigates the use of N, B-doped CNDs as a "Turn-Off" fluorescence probe for the detection of $Fe^{2+}$ in water and living cells. We used a simple one-step closed vessel microwave synthesis method to prepare the N, B-doped CNDs and assessed its performance over $Fe^{2+}$ detection. The proposed probe utilizes the intrinsic fluorescence properties of N, B-doped CNDs, which can be effectively quenched in the presence of $Fe^{2+}$ ions. We believe that our study will provide a valuable tool for the detection of this ion in environmental and biological samples and can potentially find applications in various fields such as water quality monitoring, biomedical imaging, and disease diagnosis.

## Materials and Methods

### Materials

Citric acid (CA), boric acid (BA), ethylenediamine (EDA), and phosphoric acid (PA) were purchased from Sigma-Aldrich Chemie GmbH (Munich, Germany) and were used as received without further purification. KCl (ACROS Organics), $CoCl_2$, $FeCl_2$ (Alfa Aesar), $FeCl_3$, $CrCl_3$, $AgNO_3$, $CuCl_2$, $CaCl_2$, $MgCl_2$, dialysis bags, gold electrode, Ag/AgCl reference electrode,

platinum electrode (Fisher Scientific), Dulbecco's Modified Eagle's Medium (DMEM) media, EA.hy926 cell line (ATCC), pen/strep solution, and fetal bovine serum (Sigma Aldrich) were also used as received.

**Synthesis of CNDs**

N,B-doped and N,P-doped CNDs were synthesized via a one-step closed-vessel microwave synthesis method. CA, EDA, PA, and BA were used as the carbon, nitrogen (N), phosphorus (P), and boron (B) sources, respectively. To synthesize N, B-doped CNDs, briefly, 1 g CA and 1 mL EDA were dissolved in 1 mL deionized water (DW) and mixed to achieve a uniform solution. The solution was then transferred into a microwave synthesizer with the set points of temperature= 180 °C, time= 30 min, pressure= 100 Psi, and power= 300 Watts. Once the reaction was complete, the brownish semi-liquid product was centrifuged at 4000 rpm for 20 mins to separate large particles. The supernatant was then transferred into a 1 kDa dialysis membrane and was dialyzed in DW for 48 h to further purify. After freeze-drying the retentate, a brown powder was obtained as N, B-doped CND product which was stored at room temperature for later use. The same procedure was repeated for the synthesis of N, P-doped CNDs, using 2 mL of PA (22 N).

**Characterization of CNDs**

Different characterization techniques were used to determine the structural and optical features of CNDs. The size of the synthesized CNDs was measured using atomic force microscopy (AFM, MFP-3D Origin, Asylum). To prepare the AFM samples, a 0.002 mg/mL solution of each sample in DW was sonicated for 20 minutes and then drop-casted on a mica surface. To evaluate the formation of functional groups on the CNDs' surface and elemental data analysis, Fourier Transform Infrared Spectroscopy (FTIR – Varian 670) and X-ray photoelectron spectroscopy

(XPS – Thermo Fisher ESCALAB 250Xi) were carried out. A solution of 10 mg/mL of CNDs was drop-casted and dried out for XPS analysis.

**Initial Screening of the Sensing Capability of N, B-doped and N, P-doped CNDs for $Fe^{2+}$ and $Fe^{3+}$ Detection**

A simple experimental design was established to evaluate the detection selectivity and fluorescence quenching differences between N, B-doped and N, P-doped CNDs as $Fe^{2+}$ and $Fe^{3+}$ sensors. Solutions of 0.01 mg/mL N, B-doped and N, P-doped CNDs, respectively, were prepared and incubated with 50 μM solutions of $Fe^{2+}$ and $Fe^{3+}$ separately. $FeCl_2$ and $FeCl_3$ were used for the preparation of $Fe^{2+}$ and $Fe^{3+}$ solutions, respectively. For each of these experiments, the quenching ability (*QA%*) was calculated using Eq. 4.

$$QA(\%) = \frac{F_0 - F}{F_0} \times 100 \qquad \textbf{Eq. 4}$$

where $F_0$ and $F$ are the fluorescence of CNDs samples at the excitation wavelength of 360 nm before and after incubation, respectively. The decrease in the fluorescence intensity of the CNDs with the addition of $Fe^{2+}$ or $Fe^{3+}$ ions was monitored at different time intervals of 0.5, 1, 2, 3, 4, 5, 6, 7, 8, 9, and 10 min. A 10 μL aliquot of each type of CNDs (0.01 mg/mL) was added to 100 μL of the desired metal ion and 890 μL of DW. As a control, a solution of 10 μL of CNDs (0.01 mg/mL) in 990 μL of DW was prepared, and the fluorescence was measured at the same time intervals as described.

**Selectivity Assessment Experiments**

Several metal ions including $Fe^{3+}$, $Mg^{2+}$, $Ca^{2+}$, $Co^{2+}$, $Cu^{2+}$, $Zn^{2+}$, and $Ag^{2+}$ were selected and 100 μL of each at 50 μM was treated with 10 μL of N, B-doped CNDs (0.01 mg/mL). The *QA%* for each metal ion was calculated using Eq. 4. Meanwhile, the fluorescence changes in the

presence of these metal ions with $Fe^{2+}$ were tested to evaluate the competitive interference of each metal ion on the detection of $Fe^{2+}$ by the CNDs.

**Concentration Dependency Experiments**

A 30µL aliquot of N, B-doped CNDs (0.01 mg/mL) was incubated with different concentrations of $Fe^{2+}$ solution to investigate the concentration-dependent quenching efficiency of $Fe^{2+}$ ions. The required volume of $Fe^{2+}$ solution was taken and added to the 30µL CNDs solutions to achieve 7, 15, 31, 62.5, 125, 250, 500, and 1000 nM of $Fe^{2+}$ in samples with the final volume of 3 mL for each experiment. Afterward, the QA% was calculated according to Eq. 4. Further, to analyze the efficiency of CNDs for $Fe^{2+}$ detection in a real sample, tap water was spiked with known concentrations of $Fe^{2+}$. The $Fe^{2+}$ recovery rates were calculated using the standard curves.

**UV-Vis and Band-Gap Energy Assessment**

To further evaluate the effect of doping on the band-gap energy, Tauc plots were sketched using Eq. 5 [240].

$$(\alpha . h\nu)^{\frac{1}{\gamma}} = B\ (h\nu - E_g) \qquad \textbf{Eq. 5}$$

where $\alpha$, $h$, $\nu$, $E_g$, and $B$ are the absorption coefficient, Planck's constant, photon frequency, band-gap energy, and the proportionality constant, respectively. In this equation, $\gamma = 2$ due to direct allowed transitions. Due to the amorphous structure of CNDs, the $\gamma$ factor was considered 0.5. Once plotted, a tangent line was drawn on the curve in the area of 3 to 4 eV on the X-axis. The intersection point is considered the apparent band-gap energy [171], [173].

**Electrochemical Study**

A three-electrode electrochemical cell system including a working gold electrode, 3M Ag/AgCl reference electrode, and platinum counter electrode was used to conduct the cyclic voltammetry (CV). To run the experiment, different concentrations of nitrogen-purged CNDs

solutions were added to the electrolyte solution (10 mM $Fe^{2+}$). The samples were run at the scan rate of 20 mV $s^{-1}$ at room temperature. The potential range was set between -0.2 and 0.9 V.

**Detection of $Fe^{2+}$ in Living Cells**

Human endothelial cells (EA.hy926) were cultured in DMEM supplemented with 10% fetal bovine serum and 1% pen/strep antibiotic solution. Cells were seeded on coverslips in a 12-well plate with a concentration of $10^4$ cells per well and incubated for 24 h (37 °C and 5% CO2). Then the media was removed, and the incubation was continued with N, B-doped CNDs (0.5 mg/ml) for an additional 8 h. Then the cells were washed twice with PBS and the treatment was continued with 10μM $Fe^{2+}$ solution (dissolved in DMEM) for different time intervals of 10 minutes and 1 h. The cells were washed twice with 1x PBS and then fixed with 4% paraformaldehyde for 12 minutes. The cells were washed twice with 1x PBS and stained with MitoTracker green for 30 minutes (actin-staining). The coverslips were mounted to the glass slides and the imaging was conducted at 20X magnification using a confocal microscope (Zeiss Z1 Spinning Disk Confocal Microscope).

## Results and Discussions

**Characterization of CNDs**

The AFM scans reveal a uniform distribution of both CNDs with an average height of 0.95±0.05 nm and 0.66±0.03 nm for N, B-doped and N, P-doped, respectively (Figure 20a,b).

**Figure 20. AFM Results of N, B-doped (a), and N, P-doped (b) CNDs.**

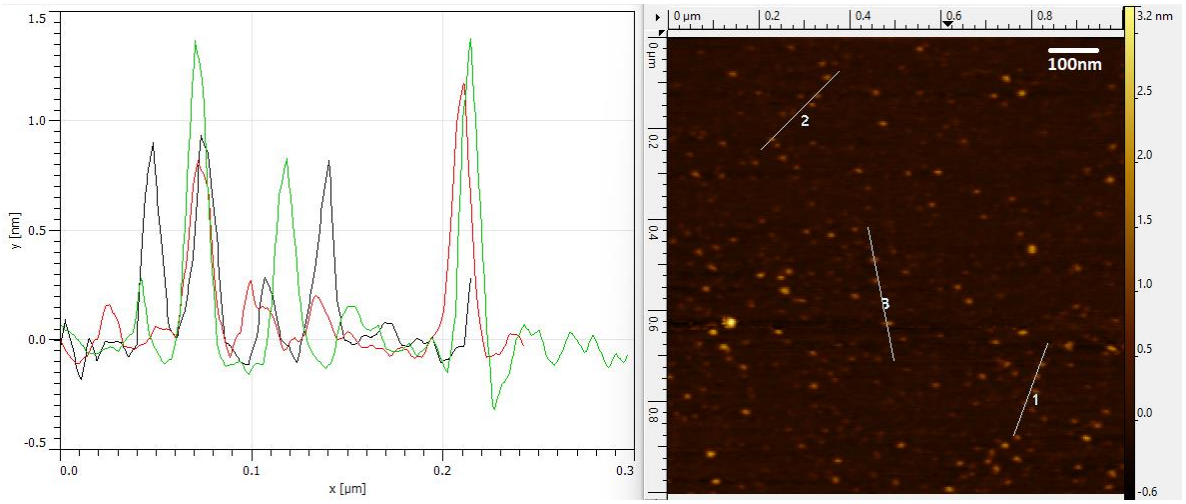


(a)

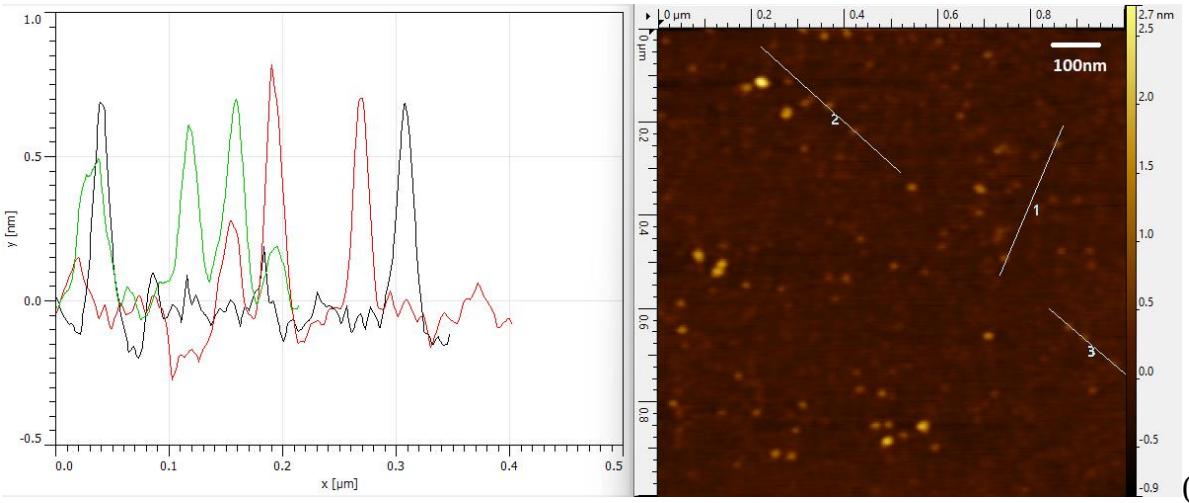


(b)

Figure 21a,b represent the fluorescence counterplots of CND samples (0.025 mg/mL) at different excitation wavelengths. Both CNDs exhibit significant excitation–dependent fluorescence intensities and the highest emission peak was observed for both at the excitation wavelength of 360 nm. In the FTIR spectrum of N, B-doped CNDs (Figure 21c) the appeared peaks at 1035, 1381, 1540, 1651, and 3258 $cm^{-1}$ are assigned to B–C, C–H, C=C, C=O, and B–OH, respectively, and the N–H and O–H bending appeared in the range of 2800–3500 $cm^{-1}$ [134]. In the N, P-doped CNDs' FTIR spectrum (Figure 21d), the peaks that appeared at 940, 1390, 1545,

1657, and 2350 are assigned to P–H bending, C–H, C=C, C=O, and P–H, respectively [161]. The XPS full survey of N, B-doped and N, P-doped CNDs confirm the incorporation of B (peak at 189 eV for B 1s) and P (peaks at 189 eV for P 2s and 133 eV for P 2p) in the CNDs structures (Figure 21e,f).

**Figure 21. Counterplot of Fluorescence Results in Terms of Emission and Excitation Wavelengths for N, B-doped (a) and N, P-doped (b) CNDs. FTIR Results of N, B-doped (c) and N, P-doped (b) CNDs. XPS Survey Results of N, B-doped (e) and N, P-doped (f) CNDs.**

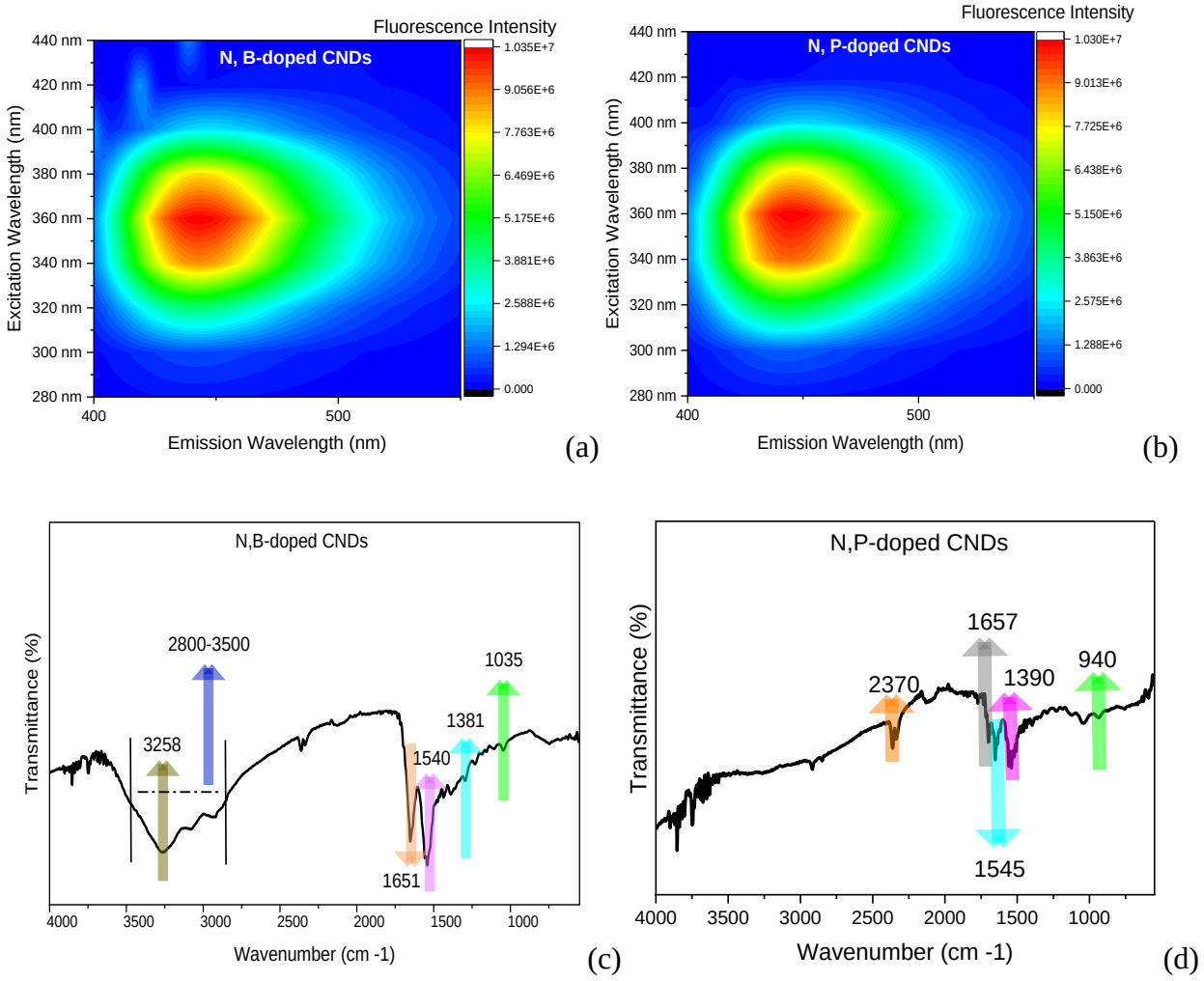

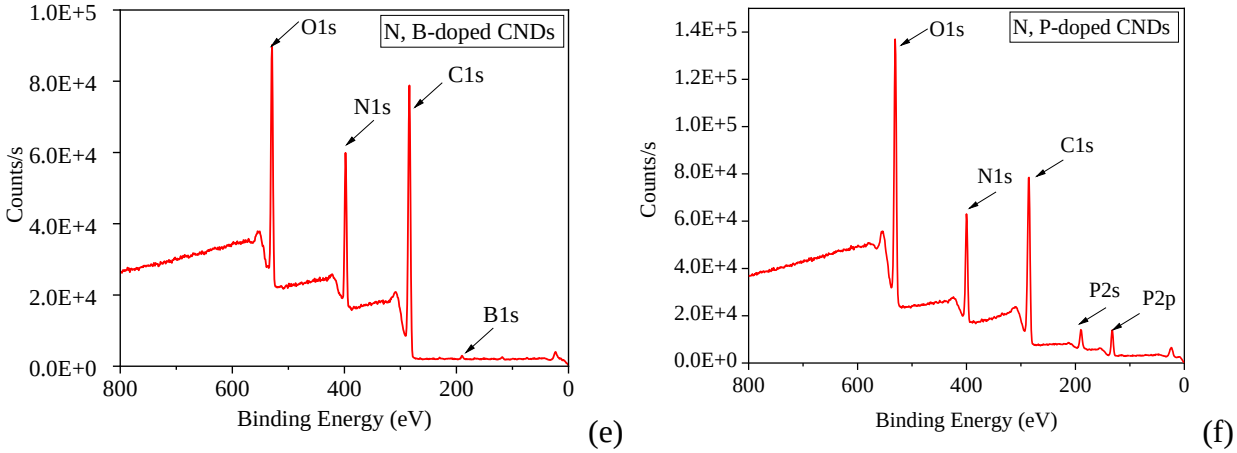


**Time Dependency and Selectivity Experiments**

The changes in the fluorescence intensities of N, B-doped and N, P-doped CNDs upon the addition of $Fe^{2+}$ and $Fe^{3+}$ ions are monitored at 0.5, 1, 2, 3, 4, 5, 6, 7, 8, 9, and 10 min intervals. As can be seen in Figure 22a, the quenching reaction in both CNDs solutions is completed within the first 30 seconds upon the addition of $Fe^{2+}$. No significant changes in fluorescence were observed after the first 30 seconds. Therefore, in all experiments, fluorescence measurements were performed considering 30 seconds as the required time for complete quenching. Comparing two CNDs (Figure 22b) reveals that although the *QA%* of both $Fe^{2+}$ and $Fe^{3+}$ with N, P-doped CNDs is higher than that of N, B-doped CNDs, the latter exhibits a greater selectivity between $Fe^{2+}$ and $Fe^{3+}$.

It was reported that $Fe^{2+}$ has a higher affinity for complex formation than $Fe^{3+}$ due to the electron configuration [241]. $Fe^{2+}$ has an empty orbital that can accommodate an electron pair from a ligand, making complex formation more energetically favorable. $Fe^{3+}$ on the other hand has a full orbital and less affinity for complex formation. This may explain why CNDs have a greater affinity for complex formation with $Fe^{2+}$ than $Fe^{3+}$ [242].

**Figure 22. Fluorescence Intensities of N, B-doped and N, P-doped CNDs Upon the Addition of $Fe^{2+}$ and $Fe^{3+}$ ions at Different Time Intervals (a), and QA (%) of N, B-doped and N, P-doped CNDs for Detection of $Fe^{2+}$ and $Fe^{3+}$ Ions (b).**

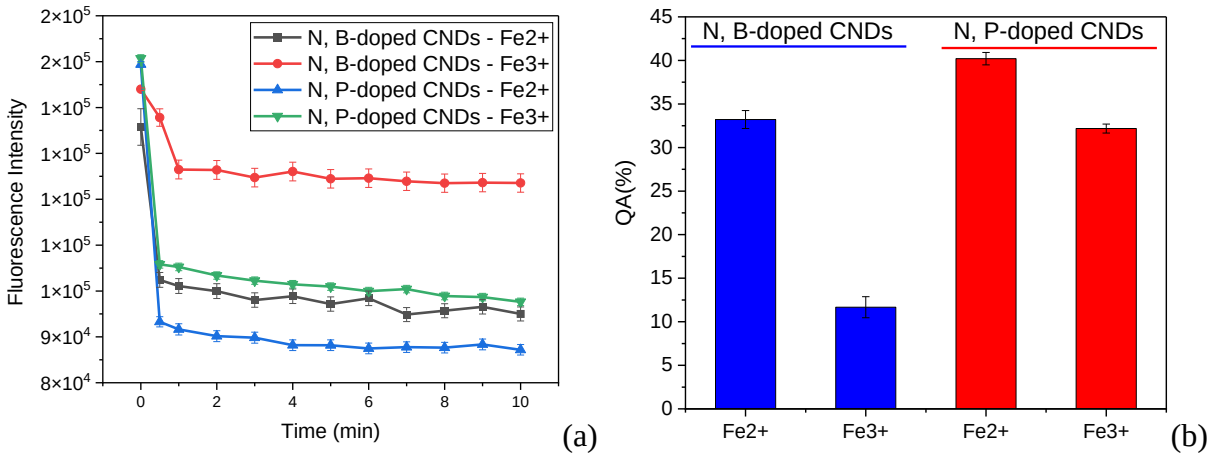


**Selectivity of N, B-doped CNDs Toward $Fe^{2+}$ Detection**

To assess the selectivity of N, B-doped CNDs toward the $Fe^{2+}$ ions among other metal ions, several metal ions were selected and incubated with the CNDs. The changes in the fluorescence intensity of N, B-doped CNDs were monitored upon the addition of different metal ions (Figure 23a). As shown in Figure 23b, the maximum fluorescence quenching occurred upon the addition of $Fe^{2+}$ (~42%) compared to the other metal ions (15% or lower). The interference of the same competitive metal ions in the $Fe^{2+}$ ions detection was also investigated (Figure 23c). Fluorescence quenching of CNDs is evident in the presence of $Fe^{2+}$ ions where the presence of other metal ions has mildly affected the quenching. Also, the last column of this figure refers to the fluorescence intensity of $Fe^{2+}$ ions without any CNDs.

**Figure 23. Fluorescence Intensity of N, B-doped CNDs in the Presence of Different Metal Ions (a), QA(%) (Averaged) of Fluorescence of N, B-doped CNDs in Presence of Different**

**Metal Ions (b); Interference of N, B-doped CNDs Fluorescence Intensity with $Fe^{2+}$ in the Presence of Competitive Metal Ions (c).**

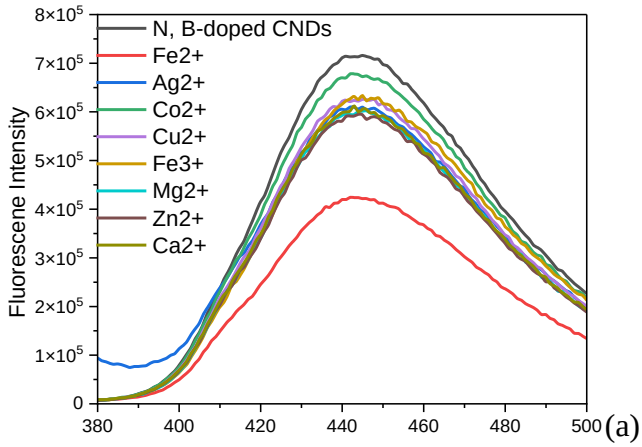

(a)

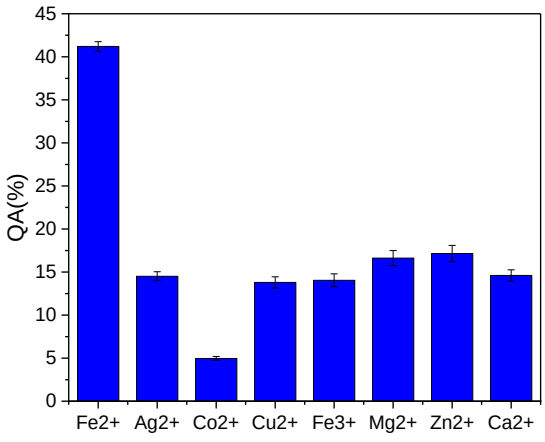

(b)

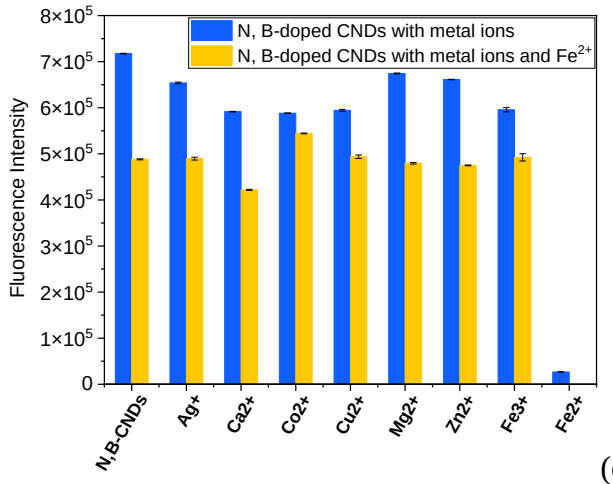

(c)

## Kinetics of Quenching

Figure 24a presents the fluorescence at different concentrations of $Fe^{2+}$ with N, B-doped CNDs. A decrease in the fluorescence of CNDs is observed which is attributed to the quenching effect that occurs upon the addition of $Fe^{2+}$. To investigate the kinetic mechanism of the quenching reaction the *Stern-Volmer* equation (Eq. 6) was used [243].

$$\frac{F_0}{F} = 1 + K_{sv}\ [Q] \qquad \textbf{Eq. 6}$$

where $K_{sv}$ is the quenching constant and $Q$ is the concentration of the quencher ($Fe^{2+}$).

This equation was re-arranged and $\frac{F_0-F}{F}$ has the correlation to follow a logarithmic model. Plotting the $\frac{F_0-F}{F}$ ratio versus the log [$Fe^{2+}$] helps calculate the LOD (Figure 24b), which is 1.8 nM (S/N = 3) within the detection range of 7 – 1000 nM. This linear relationship suggests an affinity reaction mechanism in which the quencher and the fluorescing molecule interact through a specific binding interaction [244]. Next, the logarithmic plot was split into two linear segments (Figure 24c,d), and $K_{sv}$ values calculated for lower and higher concentration linear segments were obtained to be $3.3\times10^6$ and $2\times10^5$ $M^{-1}$, respectively. At lower $Fe^{2+}$ concentrations (the first segment), the greater constant $K_{sv}$ value indicates faster kinetics of the binding of CNDs to $Fe^{2+}$ and a strong quenching effect due to a reaction between the fluorescing molecule and the quencher. The second segment of the plot with the lower $K_{sv}$ indicates a weaker quenching effect. Based on this observation, it is possible that static quenching is occurring in this reaction in which an adduct is formed between the fluorescent material and the quencher. Fluorescing molecules are surrounded by the quencher at greater concentrations of the target ion (in the second segment), and additional quencher molecules have a diminished effect on quenching kinetics [245].

The interactions between the CNDs and the target ion allow for sensitive and selective detection. Different binding interactions, such as coordination, electrostatic effects, and oxidation-reduction processes, may be the basis of $Fe^{2+}$ detection by CNDs [38].

**Figure 24. Fluorescence Intensity of N, B-doped CNDs (0.01 mg/mL) upon Addition of Different Concentrations of $Fe^{2+}$ (a). Linear Plot of $\frac{F_0-F}{F}$ Versus Log [$Fe^{2+}$] (b). The Linear Plot of $\frac{F_0-F}{F}$ Versus $Fe^{2+}$ Concentration in the Lower (b) and Higher Segment (d).**

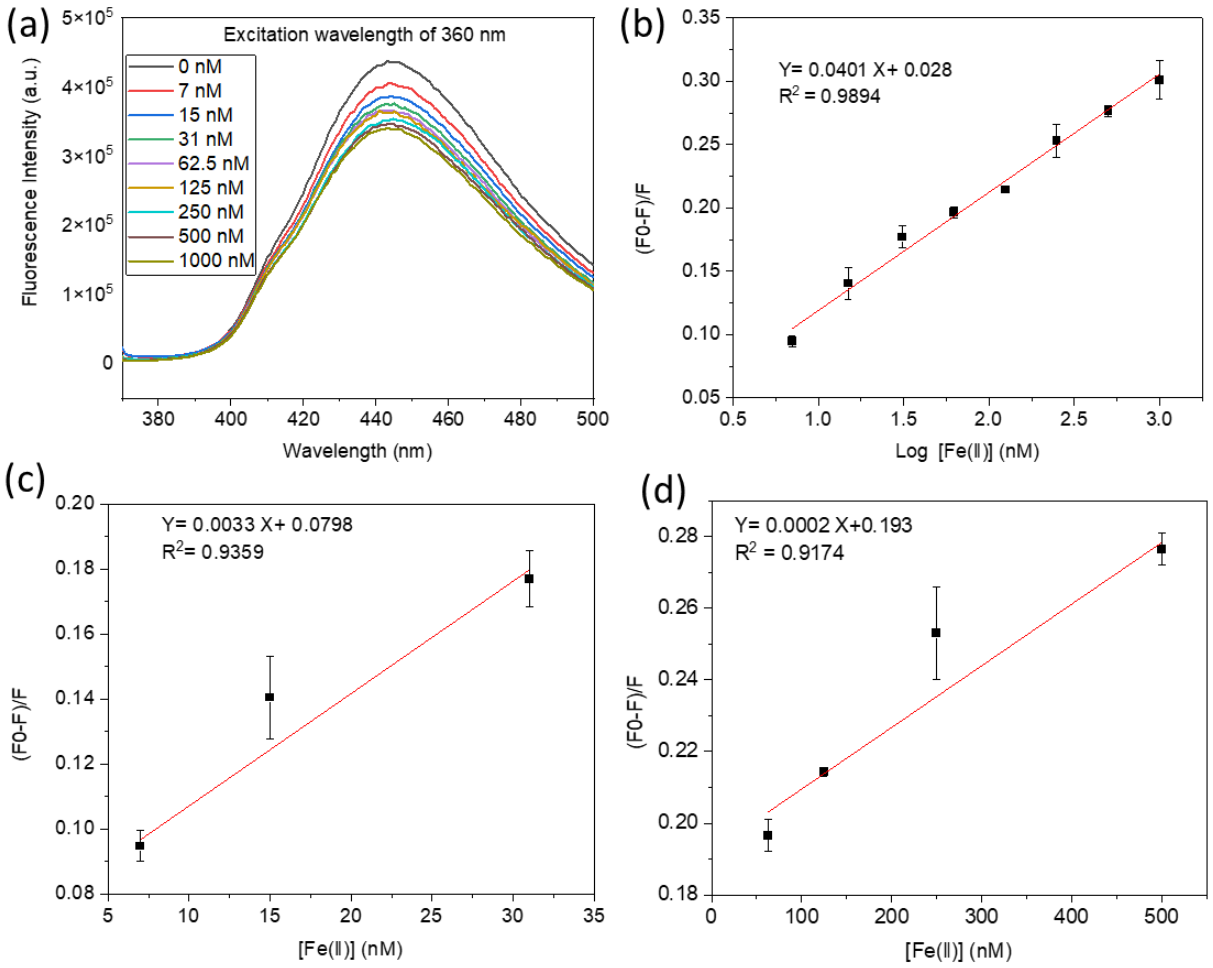


Here, a photoinduced electron transfer (PET) process is proposed (Illustration 4) to address the quenching mechanism of the N, B-doped CNDs by $Fe^{2+}$ ions [232], [246]. There is a less stable electron in the $Fe^{2+}$ structure at the $3d^6$ electronic configuration, compared to the stable configuration of $3d^5$. The electrons from $Fe^{2+}$ ions could transfer to acceptor sites of N, B-doped CNDs, becoming more stable $Fe^{3+}$ ions and forming quenched complex N, B-doped CNDs- $[Fe^{3+}]_n$ [232].

**Illustration 4. Proposed Mechanism for the Quenching Reaction Between N, B-doped CNDs, and $Fe^{2+}$ Ions.**

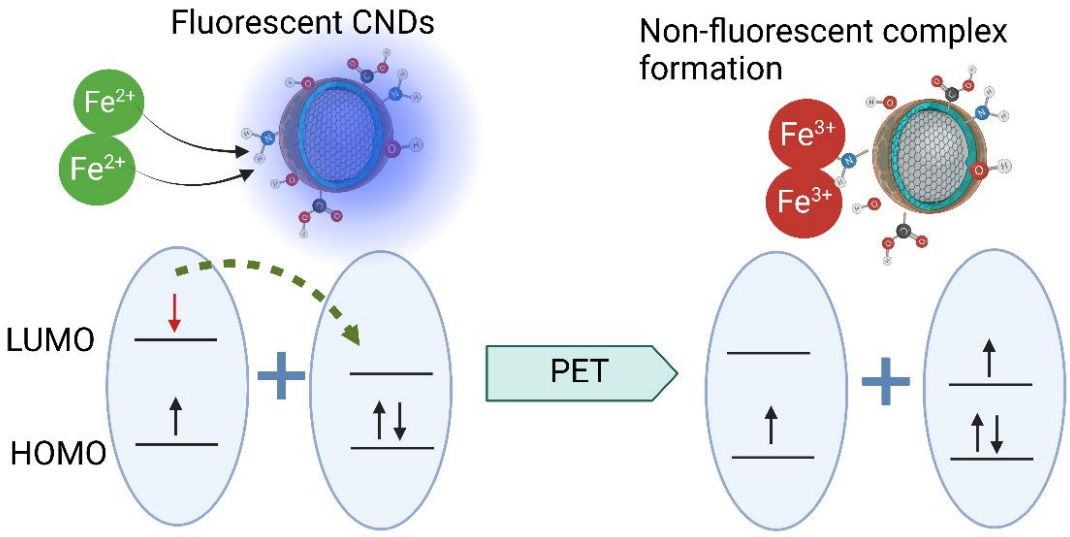


To further verify the hypothesized charge transfer quenching mechanism, cyclic voltammetry (CV) was performed. Figure 25 presents the cyclic voltammograms associated with oxidation and reduction of $Fe^{2+}$ ions before and after the inclusion of the CNDs into the system. The CV oxidation and reduction peaks of $Fe^{2+}$ were visibly suppressed as the CND concentration was raised from 0 to 0.05 mg/mL. From these results, one can conclude that the N, B-doped CNDs-$[Fe^{3+}]_n$ complex is formed thus decreasing the redox reaction due to the less availability of $Fe^{2+}$.

**Figure 25. Cyclic Voltammograms of $Fe^{2+}$ Incubated with Different Concentrations of N, B-doped CNDs.**

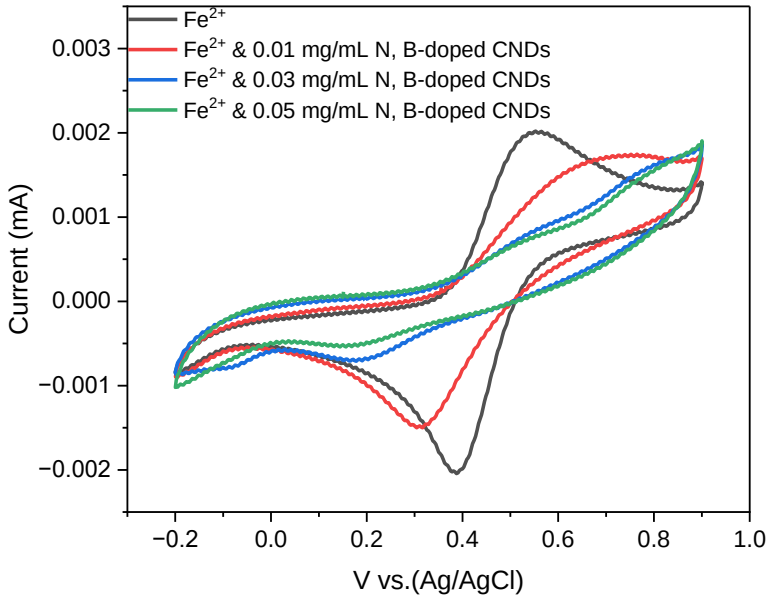


**Recovery Experiments and Real Sample Analysis**

Within the initial $Fe^{2+}$ concentration range, three distinct levels at low (31 nM), medium (125 nM), and high (1000 nM) concentrations were prepared. The recovery percentage of known amounts of spiked $Fe^{2+}$ in tap water samples using N, B-doped CNDs were calculated and reported in Table 7.

**Table 7. Recovery (%) of Spiked $Fe^{2+}$ in Tap Water Samples.**

| Spiked $Fe^{2+}$ (nM) | Segment | $\frac{F_0 - F}{F}$ | $Fe^{2+}$ (nM) | Average recovery (%) | Relative error (%) of recovery |
|---|---|---|---|---|---|
| 31 | First | 0.18 | 30.10 | 97.09 ± 4.82 | 2.9 |
| 125 | Second | 0.22 | 127.48 | 101.98 ± 3.26 | 1.98 |
| 1000 | Second | 0.40 | 1030.82 | 103.08 ± 1.78 | 3.08 |

**Detection of $Fe^{2+}$ in Living Cells**

As-synthesized N, B-doped CNDs could be employed for bioimaging due to their strong intrinsic blue fluorescence. MitoTracker green was used to dye the mitochondria of the EA.hy926 cells. Cells cultured only with CNDs show bright blue fluorescence in the absence of $Fe^{2+}$ ions (control), as can be seen in Figure 26a. After 15 minutes of incubation with both $Fe^{2+}$ and N, B-doped CNDs, moderate fluorescence quenching was observed (Figure 26b), which was almost completed 1 h afterward (Figure 26c). The observed trend suggests that 1h is sufficient for monitoring the $Fe^{2+}$ action in EA.hy926 cells.

**Figure 26. The Fluorescence Images of EA.hy926 Cells Treated with CNDs in the Absence of $Fe^{2+}$ ions (a), in the Presence of $Fe^{2+}$ Ions After 15 min (b), and 1h (c).**

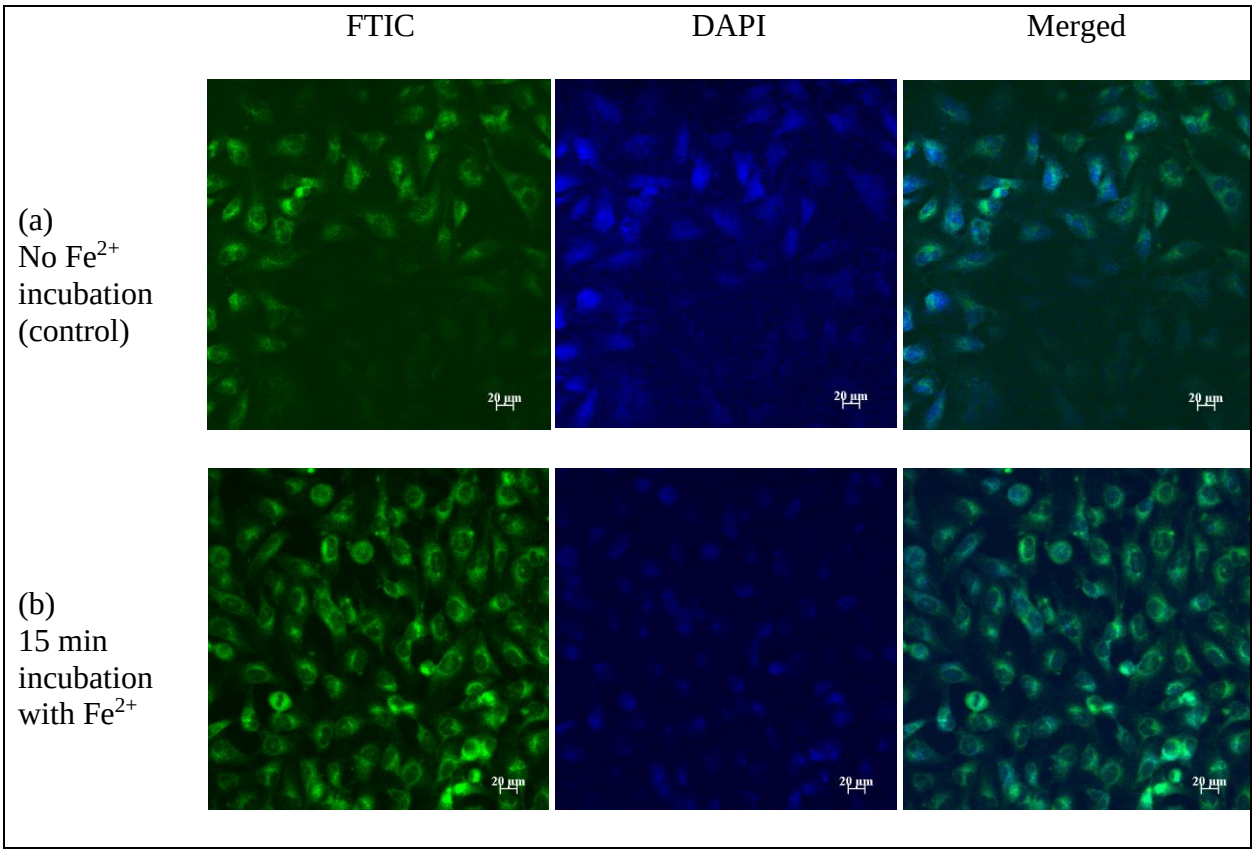

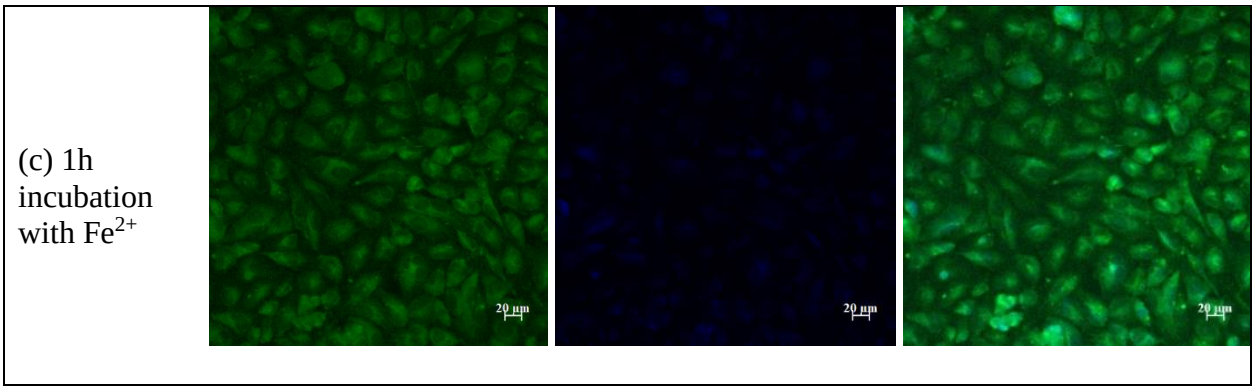


**UV-Vis Analysis**

Figure 27a represents the UV-Vis spectrum of N, B-doped CNDs incubated with and without $Fe^{2+}$. The UV-Vis spectrum of CNDs typically exhibits two significant peaks at approximately 240 and 350 nm due to π–π* transitions of C═C and n–π* transitions of non-binding orbitals mostly belonging to C═O, respectively [28]. Following incubation with $Fe^{2+}$ ions (50 μM), both maximum peaks of N, B-doped CNDs (0.01 mg/mL) display a minor blue shift. The $Fe^{2+}$ ions can interact with the N, B-doped CNDs and cause a shift in their electronic energy levels, which in turn affects the absorption spectra of the UV-Vis peaks. The Tauc plots driven from UV-Vis absorption spectra of N,B-doped CNDs before and after the addition of $Fe^{2+}$ was drawn. The band-gap energies of CNDs without and with the addition of $Fe^{2+}$ are obtained as 3.160 and 3.149, respectively (Figure 27b,c). This phenomenon could confirm the complex formation of CNDs with $Fe^{2+}$ through which the electronic structure of the N,B-doped CNDs is modified, resulting in changes in their optical properties. The interaction between the CNDs and $Fe^{2+}$ ions induces charge transfer between the two species, leading to the formation of a new energy level within the band gap of the CNDs. This is due to the changes in the highest occupied molecular orbital (HOMO) and lowest unoccupied molecular orbital (LUMO) energy levels.

**Figure 27. UV-Vis Absorbance of N, B-doped CNDs With and Without $Fe^{2+}$ Incubation (a). Tauc Plot for Band-Gap Energy Calculations for N, B-Doped CNDs Without (b), and With (c) $Fe^{2+}$ Addition.**

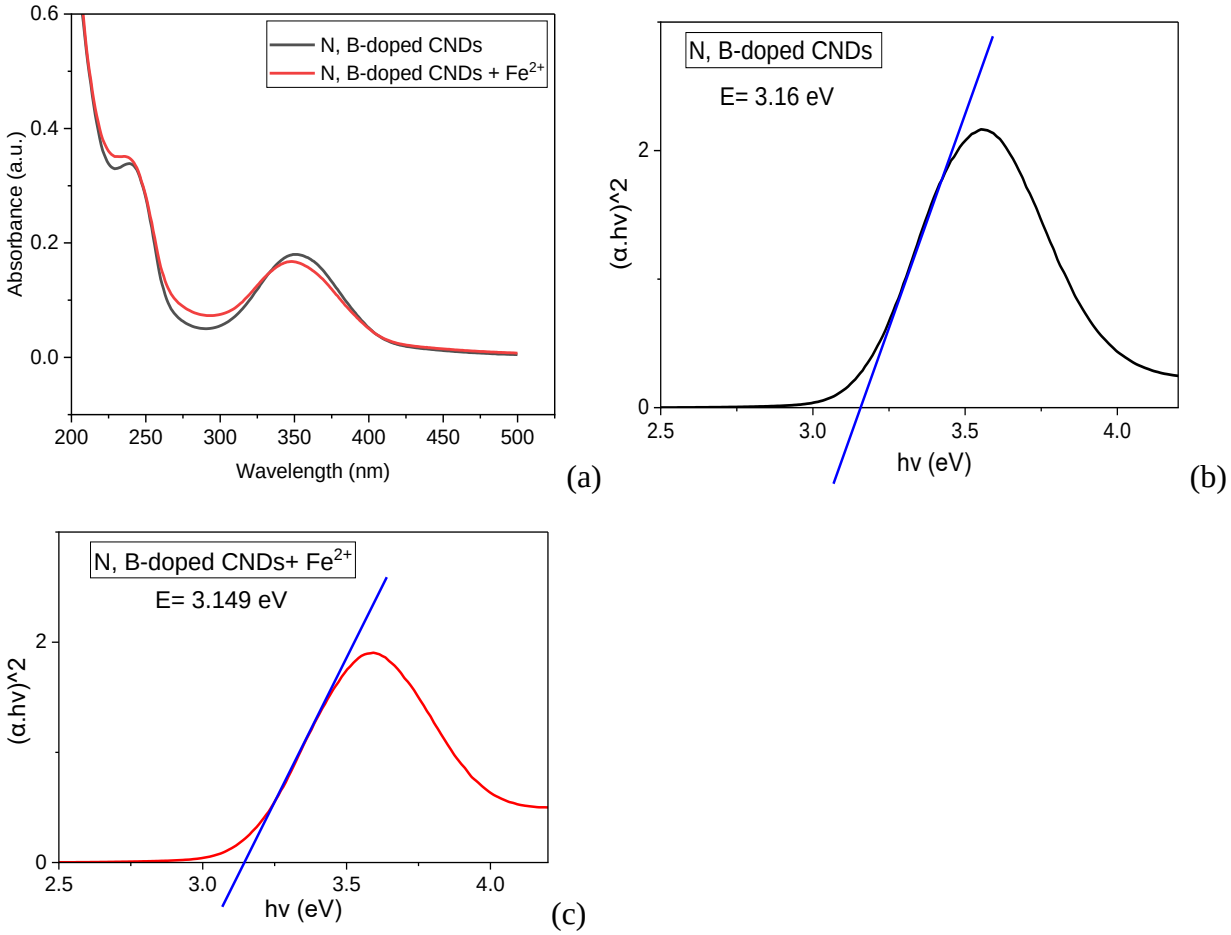


**A comparison**

Most $Fe^{2+}$ sensors presented in the literature either do not detect $Fe^{2+}$ and $Fe^{3+}$ selectively or require sophisticated components to increase selectivity. For example, the CND sensors designed by Wei et al were able to detect $Fe^{2+}$ ions, but their selectivity was limited by the shielding effects induced by tartaric and ascorbic acid present in the media [237]. Another CND-based sensor introduced by Xiao et al. was sensitive and selective and has a linear range at the μM scales [247]. The use of NaOH and other components raises biocompatibility concerns for biological

applications. In another report, a highly sensitive CND-based sensor was proposed by Liu et.al that can detect both $Fe^{2+}$ and $Fe^{3+}$ [248]. Table 8 summarizes recent research on fluorescent-based sensors used for $Fe^{2+}$ detection.

**Table 8. Comparative Study of Fluorescent-Based Sensors Used for $Fe^{2+}$ Detection Reported in Literature.**

| Sensor compound | Action mechanism | LOD | Linear range | Ref. |
|---|---|---|---|---|
| ascorbic acid-based fluorescent chemo-sensor | Turn-Off fluorescence | 0.185 μM | 0–500 mM | [228] |
| CNDs | On-Off fluorescence | 51 mM | 10–100 μM | [237] |
| N-oxide chemistry-based (Ac-MtFluNox) | Turn-On fluorescence | NA | NA | [249] |
| CNDs | Turn-On fluorescence | 60 nM | 0.5–2.0 μM | [247] |
| Rhodamine-based fluorescent polyacrylic nanoparticles | Turn-On fluorescence | 2.63 μM | 4–320 μM | [250] |
| CNDs | Turn-Off fluorescence | 7.5 nM | 0.020–10 μM | [248] |
| CNDs | Turn-Off fluorescence | 1.8 nM | 7 nM–1 μM | Present research |

## Conclusion

Here, we introduced highly fluorescent N, B-doped CNDs synthesized with a one-step microwave method providing high selectivity and sensitivity for detecting $Fe^{2+}$ in water and live cells. The concentration-dependent drop in fluorescence is a quantitative tool making these CNDs practical "Turn-Off" sensors for $Fe^{2+}$ detection. The proposed sensor showed high selectivity towards $Fe^{2+}$ ions, even in the presence of other metal ions commonly found in water and living cells. The LOD for the proposed sensor was calculated as 1.8 nM. N, B-doped CNDs are taken up

by endothelial cells, emitting a vivid blue fluorescence. The CNDs' fluorescence is inhibited after being exposed to $Fe^{2+}$, demonstrating their sensitivity to this metal ion in cells. Overall, the use of N, B-doped CNDs in metal ion detection offers improved sensitivity, selectivity, and stability, making it a useful tool in fields such as environmental monitoring, clinical diagnostics, and food safety testing.

# CHAPTER VI: CONCLUSION AND RECOMMENDATIONS

## Conclusions

In this study, we intended to investigate the optoelectronic properties and anti/pro-oxidation effects of CNDs doped with different heteroatoms. In the first part, we aimed to clarify how we can manipulate the optoelectronic properties of CNDs by employing and incorporating various heteroatoms such as N, P, and B in the structure of CNDs. A comparison of the characterization results of different synthesized co-doped CNDs with varied heteroatom levels revealed that their optoelectronic properties could be tuned by controlling the type and quantities of heteroatoms. The results show that both P and B dopants (as n-type and p-type donors, respectively) could successfully enhance the fluorescence of CNDs by dominantly influencing the carbonic core and interfering with the surface functional groups, respectively. Moreover, co-doping with N, P, and B could successfully increase the radical scavenging capabilities of the CNDs in chemical reactions (using DPPH radical scavenging assay and lucigenin chemiluminescence assay) due to providing more charge transfer platform which was discussed in detail.

The oxidative stress impact of co-doped CNDs *in vitro* is more complicated to discuss. The results of cell-based radical scavenging assays in EAhy.926 (normal) and A549 (cancer) cells showed that co-doped CNDs did not induce any ROS generation in normal cells within the non-toxic concentration range. A significant ROS induction was observed in cancer cells after exposure to CNDs. The results could offer a prooxidant capability of the introduced co-doped CNDs which is a well-established therapeutic solution in oxidative stress-associated disorders.

To further clarify the outcomes of the cellular studies, next we intended to focus on the probable pathway mechanism at the genetic level through which the contribution of CNDs to

oxidative stress might occur. We chose three antioxidant genes (GSTP1, PON1, and GPx3) which are most well-known as the first-line antioxidant defense genes against oxidative stress in cells. We monitored their expression level before and after treatment with two doses of co-doped CNDs. The RT-qPCR results in healthy cells and cancer cells turned out to be different. In cancer cells, a significant upregulation in the PON1 expression was observed after incubation with NB-CNDs which successfully could result in cell death after 24h. The same upregulation of PON1 was observed in A549 cells but with no final cell death after 24h. This could strengthen the hypothesis that co-doping (with N and B) could result in CNDs with prooxidant therapeutic potential. However, the RT-qPCR in healthy cells overall demonstrated a notable downregulation in all three selected genes. Regarding the fact that the low levels of antioxidant genes, specifically PON1, have been observed in the patients newly diagnosed with cancer, we concluded that CNDs might have the same effect on healthy cells. The proposed mechanism was based on the peroxidation of phospholipids in EAhy926 cells which could act as an inhibitor for the PON1 expression.

As an additional application, we evaluated the capability of NB-CNDs to be employed as a "Turn-Off" fluorescence-based sensor for the detection of $Fe^{2+}$. The NB-CNDs demonstrated high selectivity ( among many other metal ions) and high sensitivity (LOD=1.8 nM) for the detection of $Fe^{2+}$ in water. These CNDs could detect the $FE^{2+}$ ions in EA.hy926 cells confirmed with the confocal bioimaging technique.

Overall, based on the results and outcomes of this research, we believe that co-doping with N, P, and B served as s successful approach for enhancing the optoelectronic properties of CNDs which in turn could be used in many applications related to optoelectronic and biosensing fields. However, in the field of biological applications, the effect of co-doping needs more clarification. While the results at the cellular level showed satisfactory results in terms of oxidative stress

impacts of CNDs, our studies at the genetic level motivated us to come up with more detailed experiments to lighten these effects in cells. This could result in designing CNDs as more effective tools in biological applications.

## Recommendations for Future Works

Based on our learning in this research, a number of recommendations are being made for future researchers, as described below:

1. Using the design of experiments (DOE) for optimization of the synthesis parameters

DOE can be used to systematically investigate and optimize the synthesis of carbon nanodots (CNDs) by varying the factors that affect the synthesis process. For example, DOE can be used to determine the optimal precursor types and quantities, molar ratios of dopant heteroatoms, time, temperature, power, pressure, dialysis duration, etc. that result in the highest synthesis yield, particle size, particle zeta potential, the fluorescent emission wavelength and intensity, the excitation-dependency of emission, radical scavenging abilities, cytotoxicity, etc. DOE can also be used to identify interactions between the different variables and to determine the optimal levels of each variable for achieving the desired characteristics of CNDs. This allows researchers to optimize the synthesis process and produce CNDs with the desired properties for specific applications.

2. Evaluate the effect of exposure time on the cytotoxicity of CNDs.

The toxic behavior of CNDs could be dose- and time-dependent [251]. Here, we assessed the dose-dependency of our synthesized CNDs and discussed that the safe range resulting from the cell studies could have plausible toxic effects on the genomic material with an incubation time of 24h. We concluded that despite observing the downregulation of antioxidant genes in EAHY926 cells, no cell death was observed. We suggest that conducting a set of time-dependent toxicity

experiments might address this issue. The introduced CNDs might also cause normal cell death when the exposure time increases. A comparison between the effective incubation time needed for cancer cell death and the safe exposure time for healthy cells might lead us to reach a better conclusion of the overall anti/prooxidant therapeutic potential of the introduced CNDs for future studies.

3. Selection of prooxidant genes for genetic study

Since CNDs could intervene in the oxidative stress pathways in cells [197], we selected three antioxidant genes for our study and showed that their expression levels could be affected by the incubation of CNDs. There might be possible effects of CNDs on the prooxidant genes in cells as well, through which they could contribute to the oxidative stress pathways. This could involve examining the expression levels of genes involved in the generation of reactive oxygen species (ROS) or other prooxidant molecules and determining whether CNDs can modulate their expression levels. Such research could help shed light on the potential role of CNDs in promoting oxidative stress in cancer cells and apoptotic effects.

4. Expression pattern of proteins involved in oxidative stress.

As one step more to understanding the effect of CNDs on the oxidative stress pathways in cells, we suggest evaluation of the PON1, GSTP1, and GPx3-associated proteins in cells after exposure to CNDs. In this way, we will be able to conclude more confidently about the changes that occurred in cells at the protein levels.

# REFERENCES


[1] D. Reyes *et al.*, "Laser Ablated Carbon Nanodots for Light Emission," *Nanoscale Res. Lett.*, vol. 11, no. 1, p. 424, Dec. 2016, doi: 10.1186/s11671-016-1638-8.

[2] T. T. Meiling, P. J. Cywiński, and I. Bald, "White carbon: Fluorescent carbon nanoparticles with tunable quantum yield in a reproducible green synthesis," *Sci. Rep.*, vol. 6, no. 1, p. 28557, Jun. 2016, doi: 10.1038/srep28557.

[3] B. Das, P. Dadhich, P. Pal, P. K. Srivas, K. Bankoti, and S. Dhara, "Carbon nanodots from date molasses: New nanolights for the in vitro scavenging of reactive oxygen species," *J. Mater. Chem. B*, vol. 2, no. 39, pp. 6839–6847, Oct. 2014, doi: 10.1039/c4tb01020e.

[4] H. Li, Z. Kang, Y. Liu, and S.-T. Lee, "Carbon nanodots: synthesis, properties and applications," *J. Mater. Chem.*, vol. 22, no. 46, p. 24230, Dec. 2012, doi: 10.1039/c2jm34690g.

[5] I. J. Gomez, B. Arnaiz, M. Cacioppo, F. Arcudi, and M. Prato, "Nitrogen-doped carbon nanodots for bioimaging and delivery of paclitaxel," *J. Mater. Chem. B*, vol. 6, no. 35, pp. 5540–5548, Sep. 2018, doi: 10.1039/c8tb01796d.

[6] D. M. Arvapalli, A. T. Sheardy, K. C. Alapati, and J. Wei, "High Quantum Yield Fluorescent Carbon Nanodots for detection of Fe (III) Ions and Electrochemical Study of Quenching Mechanism," *Talanta*, vol. 209, p. 120538, Mar. 2020, doi: 10.1016/j.talanta.2019.120538.

[7] P. Miao, K. Han, Y. Tang, B. Wang, T. Lin, and W. Cheng, "Recent advances in carbon nanodots: synthesis, properties and biomedical applications," *Nanoscale*, vol. 7, no. 5, pp. 1586–1595, Feb. 2015, doi: 10.1039/C4NR05712K.

[8] S. Rai *et al.*, “Lignin derived reduced fluorescence carbon dots with theranostic approaches: Nano-drug-carrier and bioimaging,” *J. Lumin.*, vol. 190, pp. 492–503, Oct. 2017, doi: 10.1016/j.jlumin.2017.06.008.

[9] T. N. J. I. Edison, R. Atchudan, M. G. Sethuraman, J. J. Shim, and Y. R. Lee, “Microwave assisted green synthesis of fluorescent N-doped carbon dots: Cytotoxicity and bio-imaging applications,” *J. Photochem. Photobiol. B Biol.*, vol. 161, pp. 154–161, Aug. 2016, doi: 10.1016/j.jphotobiol.2016.05.017.

[10] B. Han, Y. Li, T. Peng, M. Yu, X. Hu, and G. He, “Fluorescent carbon dots directly derived from polyethyleneimine and their application for the detection of Co2+,” *Anal. Methods*, vol. 10, no. 25, pp. 2989–2993, Jul. 2018, doi: 10.1039/c8ay00481a.

[11] C. Wang, Z. Xu, and C. Zhang, “Polyethyleneimine-Functionalized Fluorescent Carbon Dots: Water Stability, pH Sensing, and Cellular Imaging,” *ChemNanoMat*, vol. 1, no. 2, pp. 122–127, Jun. 2015, doi: 10.1002/cnma.201500009.

[12] A. Chatzimarkou, T. G. Chatzimitakos, A. Kasouni, L. Sygellou, A. Avgeropoulos, and C. D. Stalikas, “Selective FRET-based sensing of 4-nitrophenol and cell imaging capitalizing on the fluorescent properties of carbon nanodots from apple seeds,” *Sensors Actuators B Chem.*, vol. 258, pp. 1152–1160, Apr. 2018, doi: 10.1016/j.snb.2017.11.182.

[13] P. A. Sajid, S. S. Chetty, S. Praneetha, A. V. Murugan, Y. Kumar, and L. Periyasamy, “One-pot microwave-assisted in situ reduction of Ag + and Au 3+ ions by Citrus limon extract and their carbon-dots based nanohybrids: a potential nano-bioprobe for cancer cellular imaging,” *RSC Adv.*, vol. 6, no. 105, pp. 103482–103490, Oct. 2016, doi: 10.1039/C6RA24033J.

[14] X. Wen *et al.*, “Green synthesis of carbon nanodots from cotton for multicolor imaging, patterning, and sensing,” *Sensors Actuators, B Chem.*, vol. 221, pp. 769–776, Dec. 2015, doi: 10.1016/j.snb.2015.07.019.

[15] A. Sachdev and P. Gopinath, “Green synthesis of multifunctional carbon dots from coriander leaves and their potential application as antioxidants, sensors and bioimaging agents,” *Analyst*, vol. 140, no. 12, pp. 4260–4269, Jun. 2015, doi: 10.1039/C5AN00454C.

[16] H. Jin, R. Gui, Y. Wang, and J. Sun, “Carrot-derived carbon dots modified with polyethyleneimine and nile blue for ratiometric two-photon fluorescence turn-on sensing of sulfide anion in biological fluids,” *Talanta*, vol. 169, pp. 141–148, Jul. 2017, doi: 10.1016/j.talanta.2017.03.083.

[17] A. Bayat, S. Masoum, and E. S. Hosseini, “Natural plant precursor for the facile and eco-friendly synthesis of carbon nanodots with multifunctional aspects,” *J. Mol. Liq.*, vol. 281, pp. 134–140, May 2019, doi: 10.1016/j.molliq.2019.02.074.

[18] N. Papaioannou *et al.*, “Structure and solvents effects on the optical properties of sugar-derived carbon nanodots,” *Sci. Rep.*, vol. 8, no. 1, p. 6559, Apr. 2018, doi: 10.1038/s41598-018-25012-8.

[19] L. Xiao and H. Sun, “Novel properties and applications of carbon nanodots,” *Nanoscale Horizons*, vol. 3, no. 6, pp. 565–597, Nov. 2018, doi: 10.1039/C8NH00106E.

[20] K. Ravishankar, K. M. Shelly, A. Narayanan, and R. Dhamodharan, “Rapid, solvent-free synthesis of amorphous, photoluminescent, carbon nanodots from imidazole and maleic anhydride solids,” *ACS Sustain. Chem. Eng.*, vol. 7, no. 15, pp. 13206–13216, Aug. 2019, doi: 10.1021/acssuschemeng.9b02446.

[21] F. Ostadhossein and D. Pan, “Functional carbon nanodots for multiscale imaging and therapy,” *WIREs Nanomedicine and Nanobiotechnology*, vol. 9, no. 3, p. e1436, May 2017, doi: 10.1002/wnan.1436.

[22] Y. Song *et al.*, “Investigation from chemical structure to photoluminescent mechanism: a type of carbon dots from the pyrolysis of citric acid and an amine,” *J. Mater. Chem. C*, vol. 3, no. 23, pp. 5976–5984, Jun. 2015, doi: 10.1039/C5TC00813A.

[23] A. Kasouni, T. Chatzimitakos, and C. Stalikas, “Bioimaging Applications of Carbon Nanodots: A Review,” *C*, vol. 5, no. 2, p. 19, Apr. 2019, doi: 10.3390/c5020019.

[24] R. Shokri and M. Amjadi, “A ratiometric fluorescence sensor for triticonazole based on the encapsulated boron-doped and phosphorous-doped carbon dots in the metal organic framework,” *Spectrochim. Acta Part A Mol. Biomol. Spectrosc.*, vol. 246, p. 118951, Feb. 2021, doi: 10.1016/j.saa.2020.118951.

[25] L. Largitte, N. A. Travlou, M. Florent, J. Secor, and T. J. Bandosz, “Effect of the surface chemistry on the photoluminescence properties of boron doped carbon dots,” *J. Photochem. Photobiol. A Chem.*, vol. 405, p. 112903, Jan. 2021, doi: 10.1016/j.jphotochem.2020.112903.

[26] J. Liu, R. Li, and B. Yang, “Carbon Dots: A New Type of Carbon-Based Nanomaterial with Wide Applications,” *ACS Cent. Sci.*, vol. 6, no. 12, pp. 2179–2195, Dec. 2020, doi: 10.1021/acscentsci.0c01306.

[27] F. Du *et al.*, “Rapid synthesis of multifunctional carbon nanodots as effective antioxidants, antibacterial agents, and quercetin nanoprobes,” *Talanta*, vol. 206, p. 120243, Jan. 2020, doi: 10.1016/j.talanta.2019.120243.

[28] Z. Ji *et al.*, “Tuning the Functional Groups on Carbon Nanodots and Antioxidant Studies,” *Molecules*, vol. 24, no. 1, p. 152, Jan. 2019, doi: 10.3390/molecules24010152.

[29] Z.-Q. Xu, J.-Y. Lan, J.-C. Jin, P. Dong, F.-L. Jiang, and Y. Liu, “Highly Photoluminescent Nitrogen-Doped Carbon Nanodots and Their Protective Effects against Oxidative Stress on Cells,” *ACS Appl. Mater. Interfaces*, vol. 7, no. 51, pp. 28346–28352, Dec. 2015, doi: 10.1021/acsami.5b08945.

[30] Z. Ji, D. M. Arvapalli, W. Zhang, Z. Yin, and J. Wei, “Nitrogen and sulfur co-doped carbon nanodots in living EA.hy926 and A549 cells: oxidative stress effect and mitochondria targeting,” *J. Mater. Sci.*, vol. 55, no. 14, pp. 6093–6104, May 2020, doi: 10.1007/s10853-020-04419-7.

[31] M. C. Ortega-Liebana *et al.*, “Upconverting Carbon Nanodots from Ethylenediaminetetraacetic Acid (EDTA) as Near-Infrared Activated Phototheranostic Agents,” *Chem. – A Eur. J.*, vol. 25, no. 21, pp. 5539–5546, Apr. 2019, doi: 10.1002/chem.201806307.

[32] V. K. Bajpai *et al.*, “Multifunctional N-P-doped carbon dots for regulation of apoptosis and autophagy in B16F10 melanoma cancer cells and in vitro imaging applications,” *Theranostics*, vol. 10, no. 17, pp. 7841–7856, 2020, doi: 10.7150/thno.42291.

[33] Y. Gong, B. Yu, W. Yang, and X. Zhang, “Phosphorus, and nitrogen co-doped carbon dots as a fluorescent probe for real-time measurement of reactive oxygen and nitrogen species inside macrophages,” *Biosens. Bioelectron.*, vol. 79, pp. 822–828, May 2016, doi: 10.1016/j.bios.2016.01.022.

[34] B. Shi, Y. Su, L. Zhang, M. Huang, R. Liu, and S. Zhao, “Nitrogen and Phosphorus Co-Doped Carbon Nanodots as a Novel Fluorescent Probe for Highly Sensitive Detection of

Fe3+ in Human Serum and Living Cells," *ACS Appl. Mater. Interfaces*, vol. 8, no. 17, pp. 10717–10725, May 2016, doi: 10.1021/acsami.6b01325.

[35] B. Das *et al.*, "Carbon Nanodots Doped Super-paramagnetic Iron Oxide Nanoparticles for Multimodal Bioimaging and Osteochondral Tissue Regeneration via External Magnetic Actuation," *ACS Biomater. Sci. Eng.*, vol. 5, no. 7, pp. 3549–3560, Jul. 2019, doi: 10.1021/acsbiomaterials.9b00571.

[36] A. Nicosia *et al.*, "Carbon Nanodots for On Demand Chemophotothermal Therapy Combination to Elicit Necroptosis: Overcoming Apoptosis Resistance in Breast Cancer Cell Lines," *Cancers (Basel).*, vol. 12, no. 11, p. 3114, Oct. 2020, doi: 10.3390/cancers12113114.

[37] Q. Yang *et al.*, "A novel mitochondria-targeted fluorescent probe based on carbon dots for Cu2+ imaging in living cells and zebrafish," *J. Photochem. Photobiol. A Chem.*, vol. 409, p. 113143, Mar. 2021, doi: 10.1016/j.jphotochem.2021.113143.

[38] P. Li and S. F. Y. Li, "Recent advances in fluorescence probes based on carbon dots for sensing and speciation of heavy metals," *Nanophotonics*, vol. 10, no. 2, pp. 877–908, Dec. 2020, doi: 10.1515/nanoph-2020-0507.

[39] W. Xuan *et al.*, "Reaction-Based 'Off–On' Fluorescent Probe Enabling Detection of Endogenous Labile Fe 2+ and Imaging of Zn 2+ -induced Fe 2+ Flux in Living Cells and Elevated Fe 2+ in Ischemic Stroke," *Bioconjug. Chem.*, vol. 27, no. 2, pp. 302–308, Feb. 2016, doi: 10.1021/acs.bioconjchem.5b00259.

[40] L. J. Mohammed and K. M. Omer, "Dual functional highly luminescence B, N Co-doped carbon nanodots as nanothermometer and Fe3+/Fe2+ sensor," *Sci. Rep.*, vol. 10, no. 1, p. 3028, Dec. 2020, doi: 10.1038/s41598-020-59958-5.

[41] H. Ding, X. H. X. B. Li, X. B. Chen, J. S. Wei, X. H. X. B. Li, and H. M. Xiong, “Surface states of carbon dots and their influences on luminescence,” *J. Appl. Phys.*, vol. 127, no. 23, p. 231101, Jun. 2020, doi: 10.1063/1.5143819.

[42] F. Yan, Y. Jiang, X. Sun, Z. Bai, Y. Zhang, and X. Zhou, “Surface modification and chemical functionalization of carbon dots: a review,” *Microchim. Acta*, vol. 185, no. 9, p. 424, Sep. 2018, doi: 10.1007/s00604-018-2953-9.

[43] L. Y. T. Chou, K. Ming, and W. C. W. Chan, “Strategies for the intracellular delivery of nanoparticles,” *Chem. Soc. Rev.*, vol. 40, no. 1, pp. 233–245, Jan. 2011, doi: 10.1039/C0CS00003E.

[44] F. Yan, Z. Sun, H. Zhang, X. Sun, Y. Jiang, and Z. Bai, “The fluorescence mechanism of carbon dots, and methods for tuning their emission color: a review,” *Microchim. Acta*, vol. 186, no. 8, p. 583, Aug. 2019, doi: 10.1007/s00604-019-3688-y.

[45] D. A. Kurdyukov *et al.*, “Template synthesis of monodisperse carbon nanodots,” *Phys. Solid State*, vol. 58, no. 12, pp. 2545–2549, Dec. 2016, doi: 10.1134/S1063783416120167.

[46] M. C. Ortega-Liebana *et al.*, “Uniform luminescent carbon nanodots prepared by rapid pyrolysis of organic precursors confined within nanoporous templating structures,” *Carbon N. Y.*, vol. 117, pp. 437–446, Jun. 2017, doi: 10.1016/j.carbon.2017.03.017.

[47] A. B. Bourlinos, A. Stassinopoulos, D. Anglos, R. Zboril, V. Georgakilas, and E. P. Giannelis, “Photoluminescent Carbogenic Dots,” *Chem. Mater.*, vol. 20, no. 14, pp. 4539–4541, Jul. 2008, doi: 10.1021/cm800506r.

[48] H. Liu *et al.*, “A fluorescent nanoprobe for 4-ethylguaiacol based on the use of a molecularly imprinted polymer doped with a covalent organic framework grafted onto carbon nanodots,” *Microchim. Acta*, vol. 186, no. 3, p. 182, Mar. 2019, doi: 10.1007/s00604-019-3306-z.

[49] J. Liu *et al.*, “Carbon Nanodot Surface Modifications Initiate Highly Efficient, Stable Catalysts for Both Oxygen Evolution and Reduction Reactions,” *Adv. Energy Mater.*, vol. 6, no. 9, p. 1502039, May 2016, doi: 10.1002/aenm.201502039.

[50] M. Liu and W. Chen, “Green synthesis of silver nanoclusters supported on carbon nanodots: enhanced photoluminescence and high catalytic activity for oxygen reduction reaction,” *Nanoscale*, vol. 5, no. 24, p. 12558, 2013, doi: 10.1039/c3nr04054b.

[51] A. Biswas, S. Paul, and A. Banerjee, “Carbon nanodots, Ru nanodots and hybrid nanodots: preparation and catalytic properties,” *J. Mater. Chem. A*, vol. 3, no. 29, pp. 15074–15081, Jun. 2015, doi: 10.1039/C5TA03355A.

[52] Y. Wang *et al.*, “Direct Solvent-Derived Polymer-Coated Nitrogen-Doped Carbon Nanodots with High Water Solubility for Targeted Fluorescence Imaging of Glioma,” *Small*, vol. 11, no. 29, pp. 3575–3581, Aug. 2015, doi: 10.1002/smll.201403718.

[53] J. A. Jaleel and K. Pramod, “Artful and multifaceted applications of carbon dot in biomedicine,” *J. Control. Release*, vol. 269, pp. 302–321, Jan. 2018, doi: 10.1016/j.jconrel.2017.11.027.

[54] S. C. Ray, A. Saha, N. R. Jana, and R. Sarkar, “Fluorescent Carbon Nanoparticles: Synthesis, Characterization, and Bioimaging Application,” *J. Phys. Chem. C*, vol. 113, no. 43, pp. 18546–18551, Oct. 2009, doi: 10.1021/jp905912n.

[55] M. Vedamalai *et al.*, “Carbon nanodots prepared from o-phenylenediamine for sensing of Cu2+ ions in cells,” *Nanoscale*, vol. 6, no. 21, pp. 13119–13125, Nov. 2014, doi: 10.1039/c4nr03213f.

[56] N. Sattarahmady, M. Rezaie-Yazdi, G. H. Tondro, and N. Akbari, “Bactericidal laser ablation of carbon dots: An in vitro study on wild-type and antibiotic-resistant Staphylococcus aureus,” *J. Photochem. Photobiol. B Biol.*, vol. 166, pp. 323–332, Jan. 2017, doi: 10.1016/j.jphotobiol.2016.12.006.

[57] N. Wang, X. Wei, A. Q. Zheng, T. Yang, M. L. Chen, and J. H. Wang, “Dual Functional Core-Shell Fluorescent Ag2S@Carbon Nanostructure for Selective Assay of E. coli O157:H7 and Bactericidal Treatment,” *ACS Sensors*, vol. 2, no. 3, pp. 371–378, Mar. 2017, doi: 10.1021/acssensors.6b00688.

[58] Q. Wang *et al.*, “Hollow luminescent carbon dots for drug delivery,” *Carbon N. Y.*, vol. 59, pp. 192–199, Aug. 2013, doi: 10.1016/j.carbon.2013.03.009.

[59] J. Tang *et al.*, “Carbon Nanodots Featuring Efficient FRET for Real-Time Monitoring of Drug Delivery and Two-Photon Imaging,” *Adv. Mater.*, vol. 25, no. 45, pp. 6569–6574, Dec. 2013, doi: 10.1002/adma.201303124.

[60] J. Du, N. Xu, J. Fan, W. Sun, and X. Peng, “Carbon Dots for In Vivo Bioimaging and Theranostics,” *Small*, vol. 15, no. 32, p. 1805087, Aug. 2019, doi: 10.1002/smll.201805087.

[61] T. Djenizian, E. Balaur, and P. Schmuki, “Direct immobilization of DNA on diamond-like carbon nanodots,” *Nanotechnology*, vol. 17, no. 8, pp. 2004–2007, Apr. 2006, doi: 10.1088/0957-4484/17/8/035.

[62] N. J. van Eck and L. Waltman, “Software survey: VOSviewer, a computer program for bibliometric mapping,” *Scientometrics*, vol. 84, no. 2, pp. 523–538, Aug. 2010, doi: 10.1007/s11192-009-0146-3.

[63] “Clarivate Analytics, Web of Science Core Collection,” 2022. http://apps.webofknowledge.com/.

[64] J. Mosquera, I. García, and L. M. Liz-Marzán, “Cellular Uptake of Nanoparticles versus Small Molecules: A Matter of Size,” *Acc. Chem. Res.*, vol. 51, no. 9, pp. 2305–2313, Sep. 2018, doi: 10.1021/acs.accounts.8b00292.

[65] N. D. Donahue, H. Acar, and S. Wilhelm, “Concepts of nanoparticle cellular uptake, intracellular trafficking, and kinetics in nanomedicine,” *Adv. Drug Deliv. Rev.*, vol. 143, pp. 68–96, Mar. 2019, doi: 10.1016/j.addr.2019.04.008.

[66] A. Truskewycz *et al.*, “Carbon Dot Therapeutic Platforms: Administration, Distribution, Metabolism, Excretion, Toxicity, and Therapeutic Potential,” *Small*, vol. 18, no. 16, p. 2106342, Apr. 2022, doi: 10.1002/smll.202106342.

[67] P. A. Rojas-Gutierrez, D. Bekah, J. Seuntjens, C. DeWolf, and J. A. Capobianco, “Cellular Uptake, Cytotoxicity and Trafficking of Supported Lipid-Bilayer-Coated Lanthanide Upconverting Nanoparticles in Alveolar Lung Cancer Cells,” *ACS Appl. Bio Mater.*, vol. 2, no. 10, pp. 4527–4536, Oct. 2019, doi: 10.1021/acsabm.9b00649.

[68] S. Ali and E. Rytting, “Influences of Nanomaterials on the Barrier Function of Epithelial Cells,” in *Nanomaterials*, 2014, pp. 45–54.

[69] S. Zhang *et al.*, “The adsorption behaviour of carbon nanodots modulated by cellular membrane potential,” *Environ. Sci. Nano*, vol. 7, no. 3, pp. 880–890, Mar. 2020, doi: 10.1039/c9en00991d.

[70] Y.-Y. Chen *et al.*, “Cytotoxicity and cell imaging of six types of carbon nanodots prepared through carbonization and hydrothermal processing of natural plant materials,” *RSC Adv.*, vol. 11, no. 27, pp. 16661–16674, May 2021, doi: 10.1039/D1RA01318A.

[71] L. Thoo, M. Z. Fahmi, I. N. Zulkipli, N. Keasberry, and A. Idris, “Interaction and cellular uptake of surface-modified carbon dot nanoparticles by J774.1 macrophages,” *Cent. Eur. J. Immunol.*, vol. 42, no. 3, pp. 324–330, 2017, doi: 10.5114/ceji.2017.70978.

[72] K. Ghosal and A. Ghosh, “Carbon dots: The next generation platform for biomedical applications,” *Mater. Sci. Eng. C*, vol. 96, pp. 887–903, Mar. 2019, doi: 10.1016/j.msec.2018.11.060.

[73] X. Yang *et al.*, “Photoluminescent carbon dots synthesized by microwave treatment for selective image of cancer cells,” *J. Colloid Interface Sci.*, vol. 456, pp. 1–6, Oct. 2015, doi: 10.1016/j.jcis.2015.06.002.

[74] H. Yan *et al.*, “Influence of the chirality of carbon nanodots on their interaction with proteins and cells,” *Nat. Commun.*, vol. 12, no. 1, p. 7208, Dec. 2021, doi: 10.1038/s41467-021-27406-1.

[75] M.-Y. Li *et al.*, “Role of surface charge on the interaction between carbon nanodots and human serum albumin,” *Spectrochim. Acta Part A Mol. Biomol. Spectrosc.*, vol. 204, pp. 484–494, Nov. 2018, doi: 10.1016/j.saa.2018.06.082.

[76] Z. Ji, Z. Yin, Z. Jia, and J. Wei, “Carbon Nanodots Derived from Urea and Citric Acid in Living Cells: Cellular Uptake and Antioxidation Effect,” *Langmuir*, vol. 36, no. 29, pp. 8632–8640, Jul. 2020, doi: 10.1021/acs.langmuir.0c01598.

[77] Y. Wei, X. Jin, T. Kong, W. Zhang, and B. Zhu, “The endocytic pathways of carbon dots in human adenoid cystic carcinoma cells,” *Cell Prolif.*, vol. 52, no. 3, pp. 1–7, May 2019, doi: 10.1111/cpr.12586.

[78] W. Zhang *et al.*, “Dark-Field Microscopic Study of Cellular Uptake of Carbon Nanodots: Nuclear Penetrability,” *Molecules*, vol. 27, no. 8, p. 2437, Apr. 2022, doi: 10.3390/molecules27082437.

[79] N. Liu and M. Tang, “Toxic effects and involved molecular pathways of nanoparticles on cells and subcellular organelles,” *J. Appl. Toxicol.*, vol. 40, no. 1, pp. 16–36, Jan. 2020, doi: 10.1002/jat.3817.

[80] B. Unnikrishnan, R.-S. Wu, S.-C. Wei, C.-C. Huang, and H.-T. Chang, “Fluorescent Carbon Dots for Selective Labeling of Subcellular Organelles,” *ACS Omega*, vol. 5, no. 20, pp. 11248–11261, May 2020, doi: 10.1021/acsomega.9b04301.

[81] X. Zhang *et al.*, “Advances in organelle-targeting carbon dots,” *Fullerenes, Nanotub. Carbon Nanostructures*, vol. 29, no. 5, pp. 394–406, May 2021, doi: 10.1080/1536383X.2020.1852217.

[82] T.-H. Chen and W.-L. Tseng, “Self-Assembly of Monodisperse Carbon Dots into High-Brightness Nanoaggregates for Cellular Uptake Imaging and Iron(III) Sensing,” *Anal. Chem.*, vol. 89, no. 21, pp. 11348–11356, Nov. 2017, doi: 10.1021/acs.analchem.7b02193.

[83] X. Zhang *et al.*, “A Cytotoxicity Study of Fluorescent Carbon Nanodots Using Human Bronchial Epithelial Cells,” *J. Nanosci. Nanotechnol.*, vol. 13, no. 8, pp. 5254–5259, Aug. 2013, doi: 10.1166/jnn.2013.7528.

[84] D. Y. Zhang *et al.*, “Ruthenium complex-modified carbon nanodots for lysosome-targeted one- and two-photon imaging and photodynamic therapy,” *Nanoscale*, vol. 9, no. 47, pp. 18966–18976, Dec. 2017, doi: 10.1039/c7nr05349e.

[85] C. Yang, R. Ogaki, L. Hansen, J. Kjems, and B. M. Teo, “Theranostic carbon dots derived from garlic with efficient anti-oxidative effects towards macrophages,” *RSC Adv.*, vol. 5, no. 118, pp. 97836–97840, Nov. 2015, doi: 10.1039/C5RA16874K.

[86] Y. Yang *et al.*, “iRGD-decorated red shift emissive carbon nanodots for tumor targeting fluorescence imaging,” *J. Colloid Interface Sci.*, vol. 509, pp. 515–521, Jan. 2018, doi: 10.1016/j.jcis.2017.09.007.

[87] C. Scialabba *et al.*, “Highly Homogeneous Biotinylated Carbon Nanodots: Red-Emitting Nanoheaters as Theranostic Agents toward Precision Cancer Medicine,” *ACS Appl. Mater. Interfaces*, vol. 11, no. 22, pp. 19854–19866, Jun. 2019, doi: 10.1021/acsami.9b04925.

[88] Y. Shen *et al.*, “Mitochondria-targeting supra-carbon dots: Enhanced photothermal therapy selective to cancer cells and their hyperthermia molecular actions,” *Carbon N. Y.*, vol. 156, pp. 558–567, Jan. 2020, doi: 10.1016/j.carbon.2019.09.079.

[89] Y. Wang, D. Zhou, H. Huang, Y. Wang, Z. Hu, and X. Li, “A yellow-emissive carbon nanodot-based ratiometric fluorescent nanosensor for visualization of exogenous and endogenous hydroxyl radicals in the mitochondria of live cells,” *J. Mater. Chem. B*, vol. 7, no. 23, pp. 3737–3744, Jun. 2019, doi: 10.1039/c9tb00289h.

[90] N. Zhou *et al.*, “Elucidating the endocytosis, intracellular trafficking, and exocytosis of carbon dots in neural cells,” *RSC Adv.*, vol. 4, no. 107, pp. 62086–62095, Nov. 2014, doi: 10.1039/c4ra09525a.

[91] A. Sachdev and P. Gopinath, “Green synthesis of multifunctional carbon dots from coriander leaves and their potential application as antioxidants, sensors and bioimaging agents,” *Analyst*, vol. 140, no. 12, pp. 4260–4269, Jun. 2015, doi: 10.1039/C5AN00454C.

[92] E. Kirbas Cilingir *et al.*, “Metformin derived carbon dots: Highly biocompatible fluorescent nanomaterials as mitochondrial targeting and blood-brain barrier penetrating biomarkers,” *J. Colloid Interface Sci.*, vol. 592, pp. 485–497, Jun. 2021, doi: 10.1016/j.jcis.2021.02.058.

[93] J. Xu, F. Zeng, H. Wu, C. Hu, C. Yu, and S. Wu, “Preparation of a Mitochondria-targeted and NO-Releasing Nanoplatform and its Enhanced Pro-Apoptotic Effect on Cancer Cells,” *Small*, vol. 10, no. 18, pp. 3750–3760, Sep. 2014, doi: 10.1002/smll.201400437.

[94] D. H. Hasenöhrl *et al.*, “Bulbous gold–carbon nanodot hybrid nanoclusters for cancer therapy,” *J. Mater. Chem. B*, vol. 5, no. 43, pp. 8591–8599, Nov. 2017, doi: 10.1039/C7TB02039B.

[95] S. Guo *et al.*, “Fluorescent Carbon Dots Shuttling between Mitochondria and the Nucleolus for in Situ Visualization of Cell Viability,” *ACS Appl. Bio Mater.*, vol. 4, no. 1, pp. 928–934, Jan. 2021, doi: 10.1021/acsabm.0c01408.

[96] P. P. Fu, Q. Xia, H.-M. Hwang, P. C. Ray, and H. Yu, “Mechanisms of nanotoxicity: Generation of reactive oxygen species,” *J. Food Drug Anal.*, vol. 22, no. 1, pp. 64–75, Mar. 2014, doi: 10.1016/j.jfda.2014.01.005.

[97] M. Havrdova *et al.*, “Toxicity of carbon dots – Effect of surface functionalization on the cell viability, reactive oxygen species generation and cell cycle,” *Carbon N. Y.*, vol. 99, no. 99, pp. 238–248, Apr. 2016, doi: 10.1016/j.carbon.2015.12.027.

[98] L. Shi *et al.*, “Eco-friendly synthesis of nitrogen-doped carbon nanodots from wool for multicolor cell imaging, patterning, and biosensing,” *Sensors Actuators, B Chem.*, vol. 235, pp. 316–324, Nov. 2016, doi: 10.1016/j.snb.2016.05.094.

[99] Q.-X. Mao, L. Han, Y. Shu, X.-W. Chen, and J.-H. Wang, “Improving the biocompatibility of carbon nanodots for cell imaging,” *Talanta*, vol. 161, pp. 54–61, Dec. 2016, doi: 10.1016/j.talanta.2016.08.031.

[100] G. G. Naik *et al.*, “Asparagus racemosus root-derived carbon nanodots as a nano-probe for biomedical applications,” *J. Mater. Sci.*, vol. 57, no. 43, pp. 20380–20401, Nov. 2022, doi: 10.1007/s10853-022-07908-z.

[101] M. D. Brand, “Mitochondrial generation of superoxide and hydrogen peroxide as the source of mitochondrial redox signaling,” *Free Radic. Biol. Med.*, vol. 100, pp. 14–31, Nov. 2016, doi: 10.1016/j.freeradbiomed.2016.04.001.

[102] S. Belperain, Z. Y. Kang, A. Dunphy, B. Priebe, N. H. L. Chiu, and Z. Jia, “Anti-Inflammatory Effect and Cellular Uptake Mechanism of Carbon Nanodots in in Human Microvascular Endothelial Cells,” *Nanomaterials*, vol. 11, no. 5, p. 1247, May 2021, doi: 10.3390/nano11051247.

[103] B. Yang, Y. Chen, and J. Shi, “Reactive Oxygen Species (ROS)-Based Nanomedicine,” *Chem. Rev.*, vol. 119, no. 8, pp. 4881–4985, Apr. 2019, doi: 10.1021/acs.chemrev.8b00626.

[104] M. Redza-Dutordoir and D. A. Averill-Bates, “Activation of apoptosis signalling pathways by reactive oxygen species,” *Biochim. Biophys. Acta - Mol. Cell Res.*, vol. 1863, no. 12, pp. 2977–2992, Dec. 2016, doi: 10.1016/j.bbamcr.2016.09.012.

[105] B. Halliwell, “Free radicals and antioxidants – quo vadis?,” *Trends Pharmacol. Sci.*, vol. 32, no. 3, pp. 125–130, Mar. 2011, doi: 10.1016/j.tips.2010.12.002.

[106] S. Galadari, A. Rahman, S. Pallichankandy, and F. Thayyullathil, “Reactive oxygen species and cancer paradox: To promote or to suppress?,” *Free Radic. Biol. Med.*, vol. 104, pp. 144–164, Mar. 2017, doi: 10.1016/j.freeradbiomed.2017.01.004.

[107] A. V. Snezhkina *et al.*, “ROS Generation and Antioxidant Defense Systems in Normal and Malignant Cells,” *Oxid. Med. Cell. Longev.*, vol. 2019, pp. 1–17, Aug. 2019, doi: 10.1155/2019/6175804.

[108] S. Prasad, S. C. Gupta, and A. K. Tyagi, “Reactive oxygen species (ROS) and cancer: Role of antioxidative nutraceuticals,” *Cancer Lett.*, vol. 387, pp. 95–105, Feb. 2017, doi: 10.1016/j.canlet.2016.03.042.

[109] X. Li, P. Fang, J. Mai, E. T. Choi, H. Wang, and X. Yang, “Targeting mitochondrial reactive oxygen species as novel therapy for inflammatory diseases and cancers,” *J. Hematol. Oncol.*, vol. 6, no. 1, p. 19, Dec. 2013, doi: 10.1186/1756-8722-6-19.

[110] M. P. Murphy, “How mitochondria produce reactive oxygen species,” *Biochem. J.*, vol. 417, no. 1, pp. 1–13, Jan. 2009, doi: 10.1042/BJ20081386.

[111] J. D. Hayes, A. T. Dinkova-Kostova, and K. D. Tew, “Oxidative Stress in Cancer,” *Cancer Cell*, vol. 38, no. 2, pp. 167–197, Aug. 2020, doi: 10.1016/j.ccell.2020.06.001.

[112] N. R. Madamanchi and M. S. Runge, “Mitochondrial Dysfunction in Atherosclerosis,” *Circ. Res.*, vol. 100, no. 4, pp. 460–473, Mar. 2007, doi: 10.1161/01.RES.0000258450.44413.96.

[113] S. Di Meo, T. T. Reed, P. Venditti, and V. M. Victor, “Role of ROS and RNS Sources in Physiological and Pathological Conditions,” *Oxid. Med. Cell. Longev.*, vol. 2016, pp. 1–44, 2016, doi: 10.1155/2016/1245049.

[114] W. Gao *et al.*, “Integrating Pt Nanoparticles with Carbon Nanodots to Achieve Robust Cascade Superoxide Dismutase-Catalase Nanozyme for Antioxidant Therapy,” *SSRN Electron. J.*, Aug. 2022, doi: 10.2139/ssrn.4183271.

[115] N. Gong *et al.*, “Carbon-dot-supported atomically dispersed gold as a mitochondrial oxidative stress amplifier for cancer treatment,” *Nat. Nanotechnol.*, vol. 14, no. 4, pp. 379–387, Apr. 2019, doi: 10.1038/s41565-019-0373-6.

[116] Z. Ji *et al.*, “Tuning the Functional Groups on Carbon Nanodots and Antioxidant Studies,” *Molecules*, vol. 24, no. 1, p. 152, Jan. 2019, doi: 10.3390/molecules24010152.

[117] W. Zhang *et al.*, “Antioxidant Capacity of Nitrogen and Sulfur Codoped Carbon Nanodots,” *ACS Appl. Nano Mater.*, vol. 1, no. 6, pp. 2699–2708, Jun. 2018, doi: 10.1021/acsanm.8b00404.

[118] D. Zhou, H. Huang, J. Yu, and Z. Hu, “Lysosome-targetable selenium-doped carbon nanodots for in situ scavenging free radicals in living cells and mice,” *Microchim. Acta*, vol. 188, no. 7, p. 223, Jul. 2021, doi: 10.1007/s00604-021-04883-1.

[119] X. Wei *et al.*, “Green Synthesis of Fluorescent Carbon Dots from Gynostemma for Bioimaging and Antioxidant in Zebrafish,” *ACS Appl. Mater. Interfaces*, vol. 11, no. 10, pp. 9832–9840, Mar. 2019, doi: 10.1021/acsami.9b00074.

[120] Y. Li, X. Zhang, M. Zheng, S. Liu, and Z. Xie, “Dopamine carbon nanodots as effective photothermal agents for cancer therapy,” *RSC Adv.*, vol. 6, no. 59, pp. 54087–54091, Jun. 2016, doi: 10.1039/c6ra02932a.

[121] B. Perillo *et al.*, “ROS in cancer therapy: the bright side of the moon,” *Exp. Mol. Med.*, vol. 52, no. 2, pp. 192–203, Feb. 2020, doi: 10.1038/s12276-020-0384-2.

[122] D.-K. Ji *et al.*, “Controlled functionalization of carbon nanodots for targeted intracellular production of reactive oxygen species,” *Nanoscale Horizons*, vol. 5, no. 8, pp. 1240–1249, Jul. 2020, doi: 10.1039/D0NH00300J.

[123] H. Huang *et al.*, “Selenium-doped two-photon fluorescent carbon nanodots for in-situ free radical scavenging in mitochondria,” *J. Colloid Interface Sci.*, vol. 567, pp. 402–409, May 2020, doi: 10.1016/j.jcis.2020.02.011.

[124] F. Lu *et al.*, “Hydroxyl functionalized carbon dots with strong radical scavenging ability promote cell proliferation,” *Mater. Res. Express*, vol. 6, no. 6, p. 065030, Mar. 2019, doi: 10.1088/2053-1591/ab0c55.

[125] N. Mauro *et al.*, “Decagram-Scale Synthesis of Multicolor Carbon Nanodots: Self-Tracking Nanoheaters with Inherent and Selective Anticancer Properties,” *ACS Appl. Mater. Interfaces*, vol. 14, no. 2, pp. 2551–2563, Jan. 2022, doi: 10.1021/acsami.1c19599.

[126] J. Shen, S. Shang, X. Chen, D. Wang, and Y. Cai, “Highly fluorescent N, S-co-doped carbon dots and their potential applications as antioxidants and sensitive probes for Cr (VI) detection,” *Sensors Actuators, B Chem.*, vol. 248, pp. 92–100, Sep. 2017, doi: 10.1016/j.snb.2017.03.123.

[127] R. R. Gaddam *et al.*, “Facile synthesis of carbon dot and residual carbon nanobeads: Implications for ion sensing, medicinal and biological applications,” *Mater. Sci. Eng. C*, vol. 73, pp. 643–652, Apr. 2017, doi: 10.1016/j.msec.2016.12.095.

[128] E. Durantie *et al.*, “Carbon nanodots: Opportunities and limitations to study their biodistribution at the human lung epithelial tissue barrier,” *Biointerphases*, vol. 13, no. 6, p. 06D404, Dec. 2018, doi: 10.1116/1.5043373.

[129] D. Li *et al.*, “Fluorescent Carbon Dots Derived from Maillard Reaction Products: Their Properties, Biodistribution, Cytotoxicity, and Antioxidant Activity,” *J. Agric. Food Chem.*, vol. 66, no. 6, pp. 1569–1575, Feb. 2018, doi: 10.1021/acs.jafc.7b05643.

[130] B. Das, P. Pal, P. Dadhich, J. Dutta, and S. Dhara, “In Vivo Cell Tracking, Reactive Oxygen Species Scavenging, and Antioxidative Gene Down Regulation by Long-Term Exposure of Biomass-Derived Carbon Dots,” *ACS Biomater. Sci. Eng.*, vol. 5, no. 1, pp. 346–356, Jan. 2019, doi: 10.1021/acsbiomaterials.8b01101.

[131] S. Xue *et al.*, “Cu,Zn Dopants Boost Electron Transfer of Carbon Dots for Antioxidation,” *Small*, vol. 17, no. 31, p. 2102178, Aug. 2021, doi: 10.1002/smll.202102178.

[132] L. Wang *et al.*, “Ultrahigh-yield synthesis of N-doped carbon nanodots that down-regulate ROS in zebrafish,” *J. Mater. Chem. B*, vol. 5, no. 38, pp. 7848–7860, Oct. 2017, doi: 10.1039/C7TB01114H.

[133] M. Havrdová *et al.*, “Intracellular Trafficking of Cationic Carbon Dots in Cancer Cell Lines MCF-7 and HeLa—Time Lapse Microscopy, Concentration-Dependent Uptake, Viability, DNA Damage, and Cell Cycle Profile,” *Int. J. Mol. Sci.*, vol. 23, no. 3, p. 1077, Jan. 2022, doi: 10.3390/ijms23031077.

[134] F. Ayaz, M. Ö. Alaş, M. Oğuz, and R. Genç, “Aluminum doped carbon nanodots as potent adjuvants on the mammalian macrophages,” *Mol. Biol. Rep.*, vol. 46, no. 2, pp. 2405–2415, Apr. 2019, doi: 10.1007/s11033-019-04701-1.

[135] W. Zhang, Z. Zeng, and J. Wei, “Electrochemical Study of DPPH Radical Scavenging for Evaluating the Antioxidant Capacity of Carbon Nanodots,” *J. Phys. Chem. C*, vol. 121, no. 34, pp. 18635–18642, Aug. 2017, doi: 10.1021/acs.jpcc.7b05353.

[136] Y. Han *et al.*, “Near-infrared-II photothermal ultra-small carbon dots promoting anticancer efficiency by enhancing tumor penetration,” *J. Colloid Interface Sci.*, vol. 616, pp. 595–604, Jun. 2022, doi: 10.1016/j.jcis.2022.02.083.

[137] M.-H. Chan *et al.*, “Natural Carbon Nanodots: Toxicity Assessment and Theranostic Biological Application,” *Pharmaceutics*, vol. 13, no. 11, p. 1874, Nov. 2021, doi: 10.3390/pharmaceutics13111874.

[138] Y. Wang *et al.*, “Sugar-originated carbon nanodots selectively damage the tumor and enhance the sensitivity of chemotherapy,” *Nano Today*, vol. 38, p. 101200, Jun. 2021, doi: 10.1016/j.nantod.2021.101200.

[139] X. Liu *et al.*, “Endogenous NO-releasing Carbon Nanodots for Tumor-specific Gas Therapy,” *Acta Biomater.*, vol. 136, pp. 485–494, Dec. 2021, doi: 10.1016/j.actbio.2021.09.051.

[140] B. Kong *et al.*, “Carbon dots as nanocatalytic medicine for anti-inflammation therapy,” *J. Colloid Interface Sci.*, vol. 611, pp. 545–553, Apr. 2022, doi: 10.1016/j.jcis.2021.12.107.

[141] J. Gao *et al.*, “Phenylenediamine-Based Carbon Nanodots Alleviate Acute Kidney Injury via Preferential Renal Accumulation and Antioxidant Capacity,” *ACS Appl. Mater. Interfaces*, vol. 12, no. 28, pp. 31745–31756, Jul. 2020, doi: 10.1021/acsami.0c05041.

[142] F. Wu, H. Su, Y. Cai, W.-K. Wong, W. Jiang, and X. Zhu, “Porphyrin-Implanted Carbon Nanodots for Photoacoustic Imaging and in Vivo Breast Cancer Ablation,” *ACS Appl. Bio Mater.*, vol. 1, no. 1, pp. 110–117, Jul. 2018, doi: 10.1021/acsabm.8b00029.

[143] C.-L. Li *et al.*, “Carbon dots prepared from ginger exhibiting efficient inhibition of human hepatocellular carcinoma cells,” *J. Mater. Chem. B*, vol. 2, no. 28, p. 4564, Jun. 2014, doi: 10.1039/c4tb00216d.

[144] G. Xu *et al.*, “In Vivo Tumor Photoacoustic Imaging and Photothermal Therapy Based on Supra-(Carbon Nanodots),” *Adv. Healthc. Mater.*, vol. 8, no. 2, p. 1800995, Jan. 2019, doi: 10.1002/adhm.201800995.

[145] C. Hu, M. Li, J. Qiu, and Y.-P. Sun, “Design and fabrication of carbon dots for energy conversion and storage,” *Chem. Soc. Rev.*, vol. 48, no. 8, pp. 2315–2337, Apr. 2019, doi: 10.1039/C8CS00750K.

[146] S. N. Baker and G. A. Baker, “Luminescent Carbon Nanodots: Emergent Nanolights,” *Angew. Chemie Int. Ed.*, vol. 49, no. 38, pp. 6726–6744, Sep. 2010, doi: 10.1002/anie.200906623.

[147] V. C. Hoang, K. Dave, and V. G. Gomes, “Carbon quantum dot-based composites for energy storage and electrocatalysis: Mechanism, applications and future prospects,” *Nano Energy*, vol. 66, p. 104093, Dec. 2019, doi: 10.1016/j.nanoen.2019.104093.

[148] X. Gao, C. Du, Z. Zhuang, and W. Chen, “Carbon quantum dot-based nanoprobes for metal ion detection,” *J. Mater. Chem. C*, vol. 4, no. 29, pp. 6927–6945, Jul. 2016, doi: 10.1039/C6TC02055K.

[149] C. Liu, P. Zhang, F. Tian, W. Li, F. Li, and W. Liu, “One-step synthesis of surface passivated carbon nanodots by microwave assisted pyrolysis for enhanced multicolor photoluminescence and bioimaging,” *J. Mater. Chem.*, vol. 21, no. 35, p. 13163, Aug. 2011, doi: 10.1039/c1jm12744f.

[150] G. Yang *et al.*, “Exploring the Emissive States of Heteroatom-Doped Graphene Quantum Dots,” *J. Phys. Chem. C*, vol. 122, no. 11, pp. 6483–6492, Mar. 2018, doi: 10.1021/acs.jpcc.8b01385.

[151] A. Sciortino, A. Cannizzo, and F. Messina, “Carbon Nanodots: A Review—From the Current Understanding of the Fundamental Photophysics to the Full Control of the Optical Response,” *C*, vol. 4, no. 4, p. 67, Dec. 2018, doi: 10.3390/c4040067.

[152] K. Wei *et al.*, “Simple Semiempirical Method for the Location Determination of HOMO and LUMO of Carbon Dots,” *J. Phys. Chem. C*, vol. 125, no. 13, pp. 7451–7457, Apr. 2021, doi: 10.1021/acs.jpcc.1c00812.

[153] Y. Park, J. Yoo, B. Lim, W. Kwon, and S.-W. Rhee, “Improving the functionality of carbon nanodots: doping and surface functionalization,” *J. Mater. Chem. A*, vol. 4, no. 30, pp. 11582–11603, Jul. 2016, doi: 10.1039/C6TA04813G.

[154] X. Yan, B. Li, X. Cui, Q. Wei, K. Tajima, and L. S. Li, “Independent tuning of the band gap and redox potential of graphene quantum dots,” *J. Phys. Chem. Lett.*, vol. 2, no. 10, pp. 1119–1124, May 2011, doi: 10.1021/jz200450r.

[155] J. T. Margraf, V. Strauss, D. M. Guldi, and T. Clark, “The Electronic Structure of Amorphous Carbon Nanodots,” *J. Phys. Chem. B*, vol. 119, no. 24, pp. 7258–7265, Jun. 2015, doi: 10.1021/jp510620j.

[156] L. Li and T. Dong, “Photoluminescence tuning in carbon dots: surface passivation or/and functionalization, heteroatom doping,” *J. Mater. Chem. C*, vol. 6, no. 30, pp. 7944–7970, Aug. 2018, doi: 10.1039/C7TC05878K.

[157] D. Cammi *et al.*, “Enhancement of the Sub-Band-Gap Photoconductivity in ZnO Nanowires through Surface Functionalization with Carbon Nanodots,” *J. Phys. Chem. C*,

vol. 122, no. 3, pp. 1852–1859, Jan. 2018, doi: 10.1021/acs.jpcc.7b10288.

[158] J. Zhou *et al.*, "Carbon dots doped with heteroatoms for fluorescent bioimaging: a review," *Microchim. Acta*, vol. 184, no. 2, pp. 343–368, Feb. 2017, doi: 10.1007/s00604-016-2043-9.

[159] P. Zuo, X. Lu, Z. Sun, Y. Guo, and H. He, "A review on syntheses, properties, characterization and bioanalytical applications of fluorescent carbon dots," *Microchim. Acta*, vol. 183, no. 2, pp. 519–542, Feb. 2016, doi: 10.1007/s00604-015-1705-3.

[160] Y. Jia, Y. Hu, Y. Li, Q. Zeng, X. Jiang, and Z. Cheng, "Boron doped carbon dots as a multifunctional fluorescent probe for sorbate and vitamin B12," *Microchim. Acta*, vol. 186, no. 2, pp. 1–10, Feb. 2019, doi: 10.1007/s00604-018-3196-5.

[161] C. J. Reckmeier, J. Schneider, A. S. Susha, and A. L. Rogach, "Luminescent colloidal carbon dots: optical properties and effects of doping [Invited]," *Opt. Express*, vol. 24, no. 2, p. A312, Jan. 2016, doi: 10.1364/oe.24.00a312.

[162] M. A. S. Shaik, D. Samanta, M. Shaw, I. Mondal, R. Basu, and A. Pathak, "Fluorescent N, S co-doped carbon dots for tartrazine sensing and mechanistic perception of their radical scavenging activity," *Sensors and Actuators Reports*, vol. 4, p. 100127, Nov. 2022, doi: 10.1016/j.snr.2022.100127.

[163] Y. Li *et al.*, "Aggregation induced red shift emission of phosphorus doped carbon dots," *RSC Adv.*, vol. 7, no. 51, pp. 32225–32228, Jun. 2017, doi: 10.1039/c7ra04781a.

[164] A. Pal, K. Ahmad, D. Dutta, and A. Chattopadhyay, "Boron Doped Carbon Dots with Unusually High Photoluminescence Quantum Yield for Ratiometric Intracellular pH Sensing," *ChemPhysChem*, vol. 20, no. 8, pp. 1018–1027, Apr. 2019, doi: 10.1002/cphc.201900140.

[165] X. Hai, Q.-X. X. Mao, W.-J. J. Wang, X.-F. F. Wang, X.-W. W. Chen, and J.-H. H. Wang, "An acid-free microwave approach to prepare highly luminescent boron-doped graphene quantum dots for cell imaging," *J. Mater. Chem. B*, vol. 3, no. 47, pp. 9109–9114, Nov. 2015, doi: 10.1039/C5TB01954K.

[166] M. K. Barman, B. Jana, S. Bhattacharyya, and A. Patra, "Photophysical Properties of Doped Carbon Dots (N, P, and B) and Their Influence on Electron/Hole Transfer in Carbon Dots–Nickel (II) Phthalocyanine Conjugates," *J. Phys. Chem. C*, vol. 118, no. 34, pp. 20034–20041, Aug. 2014, doi: 10.1021/jp507080c.

[167] A. B. Bourlinos *et al.*, "Green and simple route toward boron doped carbon dots with significantly enhanced non-linear optical properties," *Carbon N. Y.*, vol. 83, pp. 173–179, Mar. 2015, doi: 10.1016/j.carbon.2014.11.032.

[168] B. Zhi *et al.*, "Investigation of phosphorous doping effects on polymeric carbon dots: Fluorescence, photostability, and environmental impact," *Carbon N. Y.*, vol. 129, pp. 438–449, Apr. 2018, doi: 10.1016/j.carbon.2017.12.004.

[169] Christé, Esteves da Silva, and Pinto da Silva, "Evaluation of the Environmental Impact and Efficiency of N-Doping Strategies in the Synthesis of Carbon Dots," *Materials (Basel).*, vol. 13, no. 3, p. 504, Jan. 2020, doi: 10.3390/ma13030504.

[170] A. T. Sheardy, D. M. Arvapalli, and J. Wei, "Experimental and Time-Dependent Density Functional Theory Modeling Studies on the Optical Properties of Carbon Nanodots," *J. Phys. Chem. C*, vol. 124, no. 8, pp. 4684–4692, Feb. 2020, doi: 10.1021/acs.jpcc.9b10373.

[171] Z. Zeng *et al.*, "A fluorescence-electrochemical study of carbon nanodots (CNDs) in bio- and photoelectronic applications and energy gap investigation," *Phys. Chem. Chem. Phys.*, vol. 19, no. 30, pp. 20101–20109, Aug. 2017, doi: 10.1039/C7CP02875J.

[172] P. Makuła, M. Pacia, and W. Macyk, “How To Correctly Determine the Band Gap Energy of Modified Semiconductor Photocatalysts Based on UV–Vis Spectra,” *J. Phys. Chem. Lett.*, vol. 9, no. 23, pp. 6814–6817, Dec. 2018, doi: 10.1021/acs.jpclett.8b02892.

[173] P. R. Jubu, F. K. Yam, V. M. Igba, and K. P. Beh, “Tauc-plot scale and extrapolation effect on bandgap estimation from UV–vis–NIR data – A case study of β-Ga2O3,” *J. Solid State Chem.*, vol. 290, p. 121576, Oct. 2020, doi: 10.1016/j.jssc.2020.121576.

[174] S. B. Kedare and R. P. Singh, “Genesis and development of DPPH method of antioxidant assay,” *J. Food Sci. Technol.*, vol. 48, no. 4, pp. 412–422, Aug. 2011, doi: 10.1007/s13197-011-0251-1.

[175] N. Alizadeh, A. Salimi, and R. Hallaj, “A strategy for visual optical determination of glucose based on a smartphone device using fluorescent boron-doped carbon nanoparticles as a light-up probe,” *Microchim. Acta*, vol. 187, no. 1, p. 14, Jan. 2020, doi: 10.1007/s00604-019-3871-1.

[176] S. Huang, E. Yang, J. Yao, X. Chu, Y. Liu, and Q. Xiao, “Nitrogen, phosphorus and sulfur tri-doped carbon dots are specific and sensitive fluorescent probes for determination of chromium(VI) in water samples and in living cells,” *Microchim. Acta*, vol. 186, no. 12, p. 851, Dec. 2019, doi: 10.1007/s00604-019-3941-4.

[177] G. Kalaiyarasan, J. Joseph, and P. Kumar, “Phosphorus-Doped Carbon Quantum Dots as Fluorometric Probes for Iron Detection,” *ACS Omega*, vol. 5, no. 35, pp. 22278–22288, Sep. 2020, doi: 10.1021/acsomega.0c02627.

[178] D. Zhao, Z. Zhang, X. Liu, R. Zhang, and X. Xiao, “Rapid and low-temperature synthesis of N, P co-doped yellow emitting carbon dots and their applications as antibacterial agent and detection probe to Sudan Red I,” *Mater. Sci. Eng. C*, vol. 119, p. 111468, Feb. 2021, doi: 10.1016/j.msec.2020.111468.

[179] S. Garcia, R. J. Rosenbauer, J. Palandri, and M. M. Maroto-Valer, “Sequestration of non-pure carbon dioxide streams in iron oxyhydroxide-containing saline repositories,” *Int. J. Greenh. Gas Control*, vol. 7, pp. 89–97, Mar. 2012, doi: 10.1016/j.ijggc.2011.12.004.

[180] Q. Hu *et al.*, “Capillary electrophoretic study of amine/carboxylic acid-functionalized carbon nanodots,” *J. Chromatogr. A*, vol. 1304, pp. 234–240, Aug. 2013, doi: 10.1016/j.chroma.2013.07.035.

[181] J. C. Vinci *et al.*, “Spectroscopic characteristics of carbon dots (C-dots) derived from carbon fibers and conversion to sulfur-bridged C-dots nanosheets,” *Appl. Spectrosc.*, vol. 69, no. 9, pp. 1082–1090, Sep. 2015, doi: 10.1366/14-07749.

[182] M. T. Hasan *et al.*, “Nitrogen-doped graphene quantum dots: Optical properties modification and photovoltaic applications,” *Nano Res.*, vol. 12, no. 5, pp. 1041–1047, May 2019, doi: 10.1007/s12274-019-2337-4.

[183] S. Sarkar, K. Das, M. Ghosh, and P. K. Das, “Amino acid functionalized blue and phosphorous-doped green fluorescent carbon dots as bioimaging probe,” *RSC Adv.*, vol. 5, no. 81, pp. 65913–65921, Jul. 2015, doi: 10.1039/c5ra09905f.

[184] R. Sekar *et al.*, “Recent Developments in Heteroatom/Metal-Doped Carbon Dot-Based Image-Guided Photodynamic Therapy for Cancer,” *Pharmaceutics*, vol. 14, no. 9, p. 1869, Sep. 2022, doi: 10.3390/pharmaceutics14091869.

[185] M. K. Barman and A. Patra, “Current status and prospects on chemical structure driven photoluminescence behaviour of carbon dots,” *J. Photochem. Photobiol. C Photochem. Rev.*, vol. 37, pp. 1–22, Dec. 2018, doi: 10.1016/j.jphotochemrev.2018.08.001.

[186] T. T. Meiling *et al.*, “Photophysics and Chemistry of Nitrogen-Doped Carbon Nanodots with High Photoluminescence Quantum Yield,” *J. Phys. Chem. C*, vol. 122, no. 18, pp. 10217–10230, May 2018, doi: 10.1021/acs.jpcc.8b00748.

[187] R. Maiti, S. Mukherjee, S. Haldar, D. Bhowmick, and S. K. Ray, “Novel thermal quenching characteristics of luminescent carbon nanodots via tailoring the surface chemical groups,” *Carbon N. Y.*, vol. 104, pp. 226–232, Aug. 2016, doi: 10.1016/j.carbon.2016.04.004.

[188] K. Suzuki *et al.*, “Energy transfer induced by carbon quantum dots in porous zinc oxide nanocomposite films,” *J. Phys. Chem. C*, vol. 119, no. 5, pp. 2837–2843, Feb. 2015, doi: 10.1021/jp510661d.

[189] A. M. Puziy, O. I. Poddubnaya, B. Gawdzik, M. Sobiesiak, and M. Sprynskyy, “Structural Evolution of Polyimide-Derived Carbon during Phosphoric Acid Activation,” *C*, vol. 8, no. 3, p. 47, Sep. 2022, doi: 10.3390/c8030047.

[190] Z. Wu, Y. Liu, C. Deng, H. Zhao, R. Zhao, and H. Chen, “The critical role of boric acid as electrolyte additive on the electrochemical performance of lead-acid battery,” *J. Energy Storage*, vol. 27, p. 101076, Feb. 2020, doi: 10.1016/j.est.2019.101076.

[191] S. Zhu *et al.*, “Surface chemistry routes to modulate the photoluminescence of graphene quantum dots: From fluorescence mechanism to up-conversion bioimaging applications,” *Adv. Funct. Mater.*, vol. 22, no. 22, pp. 4732–4740, Nov. 2012, doi: 10.1002/adfm.201201499.

[192] Y. Zhang *et al.*, “One-step microwave synthesis of N-doped hydroxyl-functionalized carbon dots with ultra-high fluorescence quantum yields,” *Nanoscale*, vol. 8, no. 33, pp. 15281–15287, Aug. 2016, doi: 10.1039/c6nr03125k.

[193] X. Li, S. Zhang, S. A. Kulinich, Y. Liu, and H. Zeng, “Engineering surface states of carbon dots to achieve controllable luminescence for solid-luminescent composites and sensitive Be2+ detection,” *Sci. Rep.*, vol. 4, no. 1, p. 4976, May 2015, doi: 10.1038/srep04976.

[194] L. Lei *et al.*, “Tailoring chemical structures and intermolecular interactions of melem intermediates for highly efficient photocatalytic hydrogen evolution of g-C3N4,” *Appl. Surf. Sci.*, vol. 563, p. 150384, Oct. 2021, doi: 10.1016/j.apsusc.2021.150384.

[195] S. Li, X. Zhao, and H. Zhang, “Aging retardation strategy of PVDF membranes: evaluation of free radical scavenging effect of nano-particles,” *New J. Chem.*, vol. 45, no. 13, pp. 6108–6119, Apr. 2021, doi: 10.1039/d0nj05980c.

[196] H. Rizwan, S. Pal, S. Sabnam, and A. Pal, “High glucose augments ROS generation regulates mitochondrial dysfunction and apoptosis via stress signalling cascades in keratinocytes,” *Life Sci.*, vol. 241, p. 117148, Jan. 2020, doi: 10.1016/j.lfs.2019.117148.

[197] S. Khan *et al.*, “Recent Advances in Carbon Nanodots: A Promising Nanomaterial for Biomedical Applications,” *Int. J. Mol. Sci.*, vol. 22, no. 13, p. 6786, Jun. 2021, doi: 10.3390/ijms22136786.

[198] C. Dong *et al.*, “Inhibition of oxidative stress in vivo through enzyme-like activity of carbon dots,” *Appl. Mater. Today*, vol. 25, p. 101178, Dec. 2021, doi: 10.1016/j.apmt.2021.101178.

[199] A. E. Yuzhalin and A. G. Kutikhin, “Inherited variations in the SOD and GPX gene families and cancer risk,” *Free Radic. Res.*, vol. 46, no. 5, pp. 581–599, May 2012, doi: 10.3109/10715762.2012.658515.

[200] C. Gouédard, R. Barouki, and Y. Morel, “Induction of the paraoxonase-1 gene expression by resveratrol,” *Arterioscler. Thromb. Vasc. Biol.*, vol. 24, no. 12, pp. 2378–2383, Dec. 2004, doi: 10.1161/01.ATV.0000146530.24736.ce.

[201] M. Garelnabi, D. Litvinov, and H. Mahini, “Antioxidant and anti-inflammatory role of paraoxonase 1: Implication in arteriosclerosis diseases,” *N. Am. J. Med. Sci.*, vol. 4, no. 11, p. 523, Nov. 2012, doi: 10.4103/1947-2714.103310.

[202] J. Cui *et al.*, “GSTP1 and cancer: Expression, methylation, polymorphisms and signaling (Review),” *Int. J. Oncol.*, vol. 56, no. 4, pp. 867–878, Feb. 2020, doi: 10.3892/ijo.2020.4979.

[203] O. Y. Mian *et al.*, “GSTP1 Loss results in accumulation of oxidative DNA base damage and promotes prostate cancer cell survival following exposure to protracted oxidative stress,” *Prostate*, vol. 76, no. 2, pp. 199–206, Feb. 2016, doi: 10.1002/pros.23111.

[204] E. Van Dyck *et al.*, “Bronchial airway gene expression in smokers with lung or head and neck cancer,” *Cancer Med.*, vol. 3, no. 2, pp. 322–336, Apr. 2014, doi: 10.1002/cam4.190.

[205] O. M. Ighodaro and O. A. Akinloye, “First line defence antioxidants-superoxide dismutase (SOD), catalase (CAT) and glutathione peroxidase (GPX): Their fundamental role in the entire antioxidant defence grid,” *Alexandria J. Med.*, vol. 54, no. 4, pp. 287–293, Dec. 2018, doi: 10.1016/j.ajme.2017.09.001.

[206] S. Nirgude and B. Choudhary, “Insights into the role of GPX3, a highly efficient plasma antioxidant, in cancer,” *Biochem. Pharmacol.*, vol. 184, p. 114365, Feb. 2021, doi: 10.1016/j.bcp.2020.114365.

[207] R. F. Burk, G. E. Olson, V. P. Winfrey, K. E. Hill, and D. Yin, “Glutathione peroxidase-3 produced by the kidney binds to a population of basement membranes in the gastrointestinal tract and in other tissues,” *Am. J. Physiol. - Gastrointest. Liver Physiol.*, vol. 301, no. 1, pp. 32–38, Jul. 2011, doi: 10.1152/ajpgi.00064.2011.

[208] H. Mahmoudinasab and M. Saadat, “Expressions of some antioxidant genes in SH-SY5Y cells treated with β-lapachone, morphine and electromagnetic field,” *Mol. Biol. Rep.*, vol. 45, no. 3, pp. 379–387, Jun. 2018, doi: 10.1007/s11033-018-4172-1.

[209] X. Ma, W. Gao, M. I. Halawa, Y. Lan, J. Li, and G. Xu, “Lucigenin fluorescent assay of tyrosinase activity and its inhibitor screening,” *Sensors Actuators, B Chem.*, vol. 280, pp. 41–45, Feb. 2019, doi: 10.1016/j.snb.2018.10.044.

[210] F. Hedayat, S. Stevanovic, B. Miljevic, S. Bottle, and Z. D. D. Ristovski, “Review-evaluating the molecular assays for measuring the oxidative potential of particulate matter,” *Chem. Ind. Chem. Eng. Q.*, vol. 21, no. 1–2, pp. 201–210, Jan. 2015, doi: 10.2298/CICEQ140228031H.

[211] J. Zhang *et al.*, “Glutathione prevents high glucose-induced pancreatic fibrosis by suppressing pancreatic stellate cell activation via the ROS/TGFβ/SMAD pathway,” *Cell Death Dis.*, vol. 13, no. 5, p. 440, May 2022, doi: 10.1038/s41419-022-04894-7.

[212] M. H. Rashnavadi, Z. Tahmasebi, Z. Piravar, and A. M. Gholi, “N-Acetyl-L-cysteine effects on oxidative stress-induced high glucose-cultured human dermal fibroblasts,” *Gene Reports*, vol. 26, p. 101522, Mar. 2022, doi: 10.1016/j.genrep.2022.101522.

[213] F. Zhao, Y. Zhao, Y. Liu, X. Chang, C. Chen, and Y. Zhao, “Cellular Uptake, Intracellular Trafficking, and Cytotoxicity of Nanomaterials,” *Small*, vol. 7, no. 10, pp. 1322–1337, May 2011, doi: 10.1002/smll.201100001.

[214] F. Lao *et al.*, “Fullerene Nanoparticles Selectively Enter Oxidation-Damaged Cerebral Microvessel Endothelial Cells and Inhibit JNK-Related Apoptosis,” *ACS Nano*, vol. 3, no. 11, pp. 3358–3368, Nov. 2009, doi: 10.1021/nn900912n.

[215] S. Wu, W. Zhu, P. Thompson, and Y. A. Hannun, “Evaluating intrinsic and non-intrinsic cancer risk factors,” *Nat. Commun.*, vol. 9, no. 1, p. 3490, Aug. 2018, doi: 10.1038/s41467-018-05467-z.

[216] R. Aghakhani, M. Nasiri, and D. Irani, “Glutathione peroxidase 1 gene polymorphism in nephrolithiasis patients from South of Iran,” *Iran. J. Kidney Dis.*, vol. 11, no. 1, pp. 29–35, 2017, Accessed: Feb. 21, 2023. [Online]. Available: https://pubmed.ncbi.nlm.nih.gov/28174350/.

[217] M. Alizadeh, M. Nasiri, M. Samadi, N. Ghasemi, and A. Moradi, “Association of M55L and Q192R polymorphisms of paraoxonase 1 gene (PON1) with recurrent pregnancy loss risk: A case–control study,” *Int. J. Reprod. Biomed.*, vol. 19, no. 6, pp. 559–568, Jul. 2021, doi: 10.18502/ijrm.v19i6.9377.

[218] G. Pizzino *et al.*, “Oxidative Stress: Harms and Benefits for Human Health,” *Oxid. Med. Cell. Longev.*, vol. 2017, pp. 1–13, 2017, doi: 10.1155/2017/8416763.

[219] M. Sima *et al.*, “The Differential Effect of Carbon Dots on Gene Expression and DNA Methylation of Human Embryonic Lung Fibroblasts as a Function of Surface Charge and Dose,” *Int. J. Mol. Sci.*, vol. 21, no. 13, p. 4763, Jul. 2020, doi: 10.3390/ijms21134763.

[220] M. B. D. Aldonza *et al.*, “Paraoxonase-1 (PON1) induces metastatic potential and apoptosis escape via its antioxidative function in lung cancer cells,” *Oncotarget*, vol. 8, no. 26, pp. 42817–42835, Jun. 2017, doi: 10.18632/oncotarget.17069.

[221] S. Hume, G. L. Dianov, and K. Ramadan, “A unified model for the G1/S cell cycle transition,” *Nucleic Acids Res.*, vol. 48, no. 22, pp. 12483–12501, Dec. 2020, doi: 10.1093/nar/gkaa1002.

[222] E. T. Elkiran, N. Mar, B. Aygen, F. Gursu, A. Karaoglu, and S. Koca, “Serum paraoxonase and arylesterase activities in patients with lung cancer in a Turkish population,” *BMC Cancer*, vol. 7, no. 1, p. 48, Dec. 2007, doi: 10.1186/1471-2407-7-48.

[223] Y. Faridvand, A. E. Oskuyi, and M.-H. Khadem-Ansari, “Serum 8-isoprostane levels and paraoxonase 1 activity in patients with stage I multiple myeloma,” *Redox Rep.*, vol. 21, no. 5, pp. 1–5, Feb. 2016, doi: 10.1179/1351000215Y.0000000034.

[224] I. M. Medina-Díaz *et al.*, “The Relationship between Cancer and Paraoxonase 1,” *Antioxidants*, vol. 11, no. 4, p. 697, Mar. 2022, doi: 10.3390/antiox11040697.

[225] M. Jovanovic-Tucovic *et al.*, “AMP-activated protein kinase inhibits MPP+-induced oxidative stress and apoptotic death of SH-SY5Y cells through sequential stimulation of Akt and autophagy,” *Eur. J. Pharmacol.*, vol. 863, p. 172677, Nov. 2019, doi: 10.1016/j.ejphar.2019.172677.

[226] H. Ozaki and H. Li, “Rejection of organic compounds by ultra-low pressure reverse osmosis membrane,” *Water Res.*, vol. 36, no. 1, pp. 123–130, Jan. 2002, doi: 10.1016/S0043-1354(01)00197-X.

[227] P. Omur-Ozbek and A. M. Dietrich, “Retronasal perception and flavour thresholds of iron and copper in drinking water,” *J. Water Health*, vol. 9, no. 1, pp. 1–9, Mar. 2011, doi: 10.2166/wh.2011.157b.

[228] U. Duru Kamaci, M. Kamaci, and A. Peksel, “A dual responsive colorimetric sensor based on polyazomethine and ascorbic acid for the detection of Al (III) and Fe (II) ions,” *Spectrochim. Acta Part A Mol. Biomol. Spectrosc.*, vol. 254, p. 119650, Jun. 2021, doi: 10.1016/j.saa.2021.119650.

[229] A. T. Aron, A. G. Reeves, and C. J. Chang, “Activity-based sensing fluorescent probes for iron in biological systems,” *Curr. Opin. Chem. Biol.*, vol. 43, pp. 113–118, Apr. 2018, doi: 10.1016/j.cbpa.2017.12.010.

[230] T. Hirayama and H. Nagasawa, “Chemical tools for detecting Fe ions,” *J. Clin. Biochem. Nutr.*, vol. 60, no. 1, pp. 39–48, Jan. 2017, doi: 10.3164/jcbn.16-70.

[231] M. Formica, V. Fusi, L. Giorgi, and M. Micheloni, “New fluorescent chemosensors for metal ions in solution,” *Coord. Chem. Rev.*, vol. 256, no. 1–2, pp. 170–192, Jan. 2012, doi: 10.1016/j.ccr.2011.09.010.

[232] T. Skorjanc, D. Shetty, and M. Valant, “Covalent Organic Polymers and Frameworks for Fluorescence-Based Sensors,” *ACS Sensors*, vol. 6, no. 4, pp. 1461–1481, Apr. 2021, doi: 10.1021/acssensors.1c00183.

[233] A. M. Şenol, Y. Onganer, and K. Meral, “An unusual ‘off-on’ fluorescence sensor for iron(III) detection based on fluorescein–reduced graphene oxide functionalized with polyethyleneimine,” *Sensors Actuators B Chem.*, vol. 239, pp. 343–351, Feb. 2017, doi: 10.1016/j.snb.2016.08.025.

[234] X. Gao, C. Du, Z. Zhuang, and W. Chen, “Carbon quantum dot-based nanoprobes for metal ion detection,” *J. Mater. Chem. C*, vol. 4, no. 29, pp. 6927–6945, Jul. 2016, doi: 10.1039/C6TC02055K.

[235] F. Yan, D. Kong, Y. Luo, Q. Ye, Y. Wang, and L. Chen, “Carbon nanodots prepared for dopamine and Al3+ sensing, cellular imaging and logic gate operation,” *Mater. Sci. Eng. C*, vol. 68, pp. 732–738, Nov. 2016, doi: 10.1016/j.msec.2016.05.123.

[236] K. Radhakrishnan, P. Panneerselvam, and M. Marieeswaran, “A green synthetic route for the surface-passivation of carbon dots as an effective multifunctional fluorescent sensor for the recognition and detection of toxic metal ions from aqueous solution,” *Anal. Methods*, vol. 11, no. 4, pp. 490–506, Jan. 2019, doi: 10.1039/C8AY02451K.

[237] S. Wei *et al.*, “A sensitive ‘ON–OFF’ fluorescent probe based on carbon dots for Fe 2+ detection and cell imaging,” *Analyst*, vol. 145, no. 6, pp. 2357–2366, Mar. 2020, doi: 10.1039/C9AN02309G.

[238] Y. Sun, P. Sun, and W. Guo, “Fluorescent probes for iron, heme, and related enzymes,” *Coord. Chem. Rev.*, vol. 429, p. 213645, Feb. 2021, doi: 10.1016/j.ccr.2020.213645.

[239] R. S. Zeidan, S. M. Han, C. Leeuwenburgh, and R. Xiao, “Iron homeostasis and organismal aging,” *Ageing Res. Rev.*, vol. 72, p. 101510, Dec. 2021, doi: 10.1016/J.ARR.2021.101510.

[240] P. Makuła, M. Pacia, and W. Macyk, “How To Correctly Determine the Band Gap Energy of Modified Semiconductor Photocatalysts Based on UV–Vis Spectra,” *J. Phys. Chem. Lett.*, vol. 9, no. 23, pp. 6814–6817, Dec. 2018, doi: 10.1021/acs.jpclett.8b02892.

[241] S. Sasan, T. Chopra, A. Gupta, D. Tsering, K. K. Kapoor, and R. Parkesh, “Fluorescence ‘Turn-Off’ and Colorimetric Sensor for Fe 2+ , Fe 3+ , and Cu 2+ Ions Based on a 2,5,7-Triarylimidazopyridine Scaffold,” *ACS Omega*, vol. 7, no. 13, pp. 11114–11125, Apr. 2022, doi: 10.1021/acsomega.1c07193.

[242] T. Yamashita and P. Hayes, “Analysis of XPS spectra of Fe2+ and Fe3+ ions in oxide materials,” *Appl. Surf. Sci.*, vol. 254, no. 8, pp. 2441–2449, Feb. 2008, doi: 10.1016/j.apsusc.2007.09.063.

[243] H. Boaz and G. K. Rollefson, “The Quenching of Fluorescence. Deviations from the Stern-Volmer Law,” *J. Am. Chem. Soc.*, vol. 72, no. 8, pp. 3435–3443, Aug. 1950, doi: 10.1021/ja01164a032.

[244] L. Meng, A. P. F. Turner, and W. C. Mak, “Soft and flexible material-based affinity sensors,” *Biotechnol. Adv.*, vol. 39, p. 107398, Mar. 2020, doi: 10.1016/j.biotechadv.2019.05.004.

[245] D. Genovese, M. Cingolani, E. Rampazzo, L. Prodi, and N. Zaccheroni, “Static quenching upon adduct formation: a treatment without shortcuts and approximations,” *Chem. Soc. Rev.*, vol. 50, no. 15, pp. 8414–8427, Aug. 2021, doi: 10.1039/D1CS00422K.

[246] K. M. Omer and A. Q. Hassan, “Chelation-enhanced fluorescence of phosphorus doped carbon nanodots for multi-ion detection,” *Microchim. Acta*, vol. 184, no. 7, pp. 2063–2071, Jul. 2017, doi: 10.1007/s00604-017-2196-1.

[247] S. J. Xiao, Z. J. Chu, J. Zuo, X. J. Zhao, C. Z. Huang, and L. Zhang, “Fluorescent carbon dots: facile synthesis at room temperature and its application for Fe2+ sensing,” *J. Nanoparticle Res.*, vol. 19, no. 2, p. 84, Feb. 2017, doi: 10.1007/s11051-016-3698-1.

[248] F. Liu *et al.*, “Fluorimetric and colorimetric analysis of total iron ions in blood or tap water using nitrogen-doped carbon dots with tunable fluorescence,” *New J. Chem.*, vol. 42, no. 12, pp. 9676–9683, Jun. 2018, doi: 10.1039/C8NJ00711J.

[249] T. Hirayama, S. Kadota, M. Niwa, and H. Nagasawa, “A mitochondria-targeted fluorescent probe for selective detection of mitochondrial labile Fe(ii).,” *Metallomics*, vol. 10, no. 6, pp. 794–801, Jun. 2018, doi: 10.1039/C8MT00049B.

[250] S. Ghezelsefloo, J. Keyvan Rad, M. Hajiali, and A. R. Mahdavian, “Rhodamine-based fluorescent polyacrylic nanoparticles: A highly selective and sensitive chemosensor for Fe (II) and Fe (III) cations in water,” *J. Environ. Chem. Eng.*, vol. 9, no. 2, p. 105082, Apr. 2021, doi: 10.1016/j.jece.2021.105082.

[251] Y. Song, D. Feng, W. Shi, X. Li, and H. Ma, “Parallel comparative studies on the toxic effects of unmodified CdTe quantum dots, gold nanoparticles, and carbon nanodots on live cells as well as green gram sprouts,” *Talanta*, vol. 116, pp. 237–244, Nov. 2013, doi: 10.1016/J.TALANTA.2013.05.022.

APPENDIX A: EFFECT OF DOPING HETEROATOMS ON THE OPTICAL BEHAVIORS AND RADICAL SCAVENGING PROPERTIES OF CNDS

**Figure S1.1. AFM Results of E-CNDs (a), Low P%-CNDs (b), High P%-CNDs (c), Low B%-CNDs (d), and High B%-CNDs (e).**

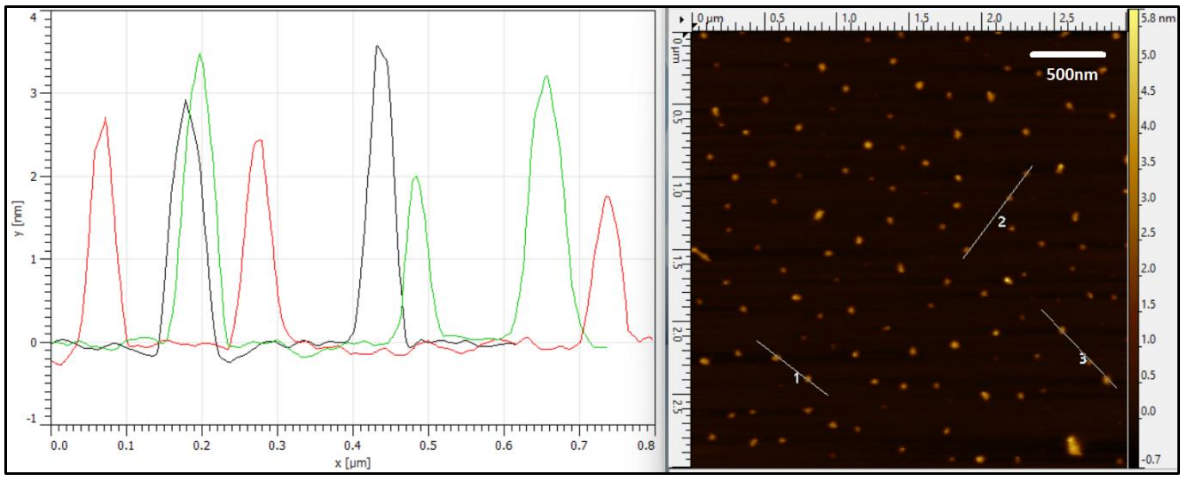


(a)

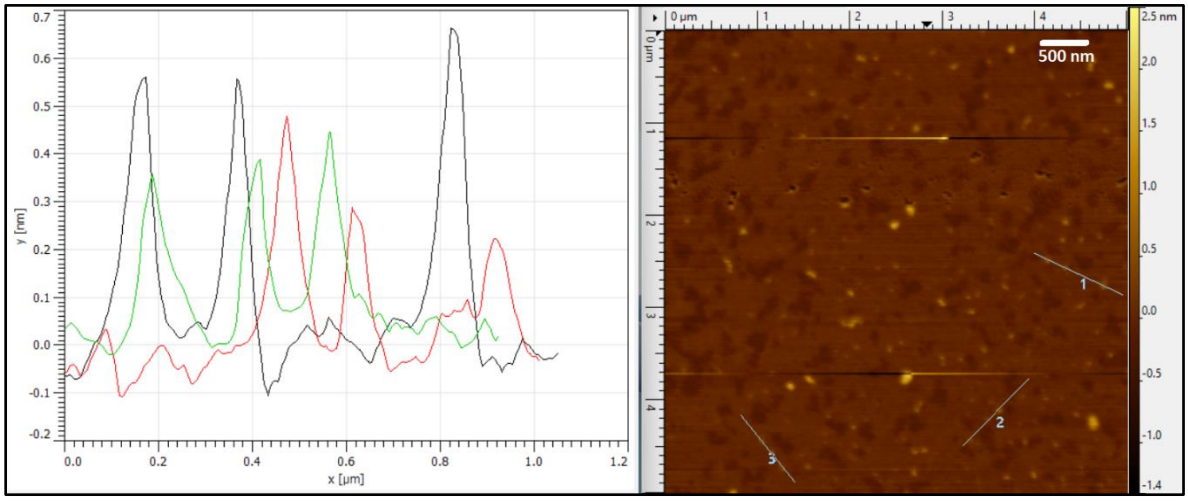


(b)

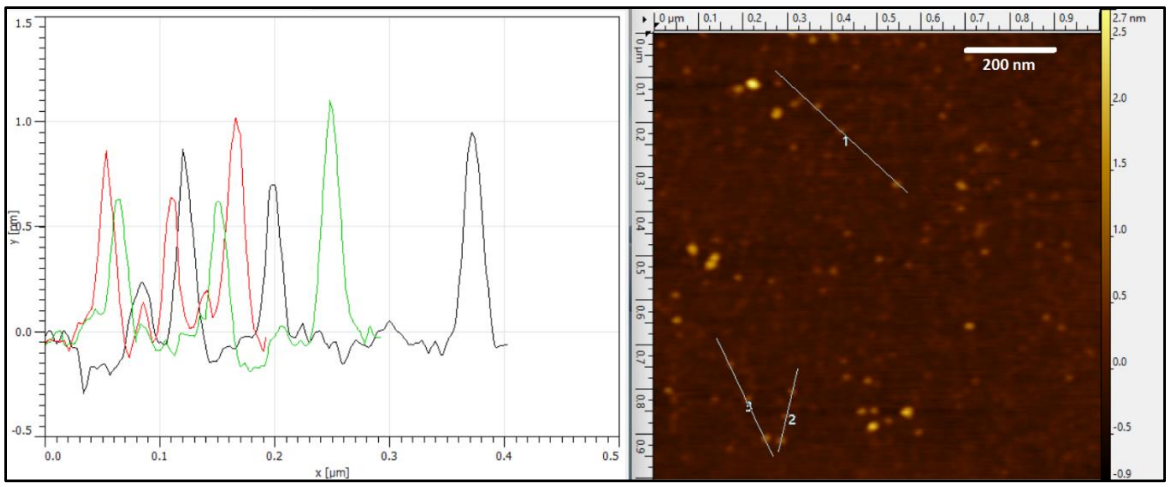


(c)

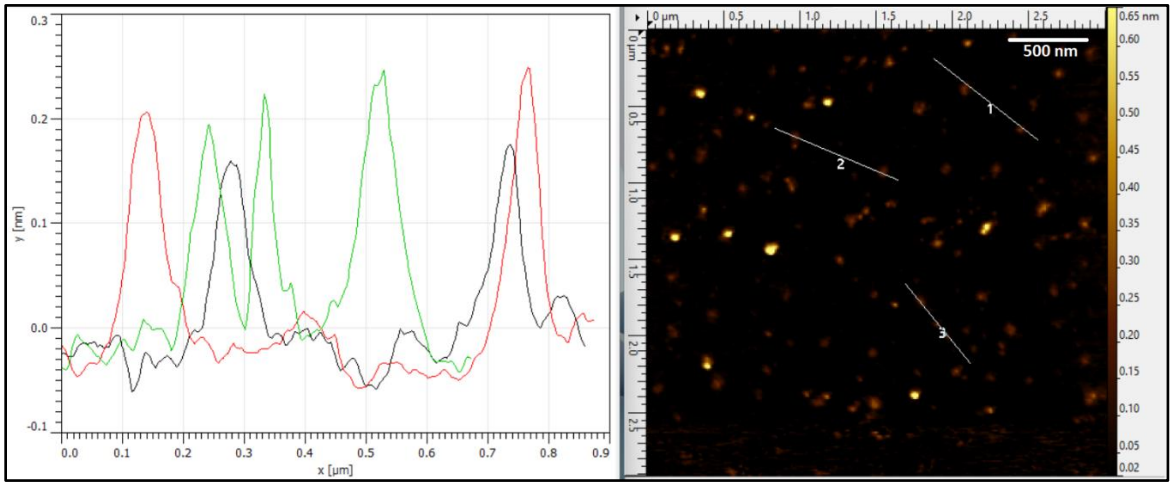


(d)

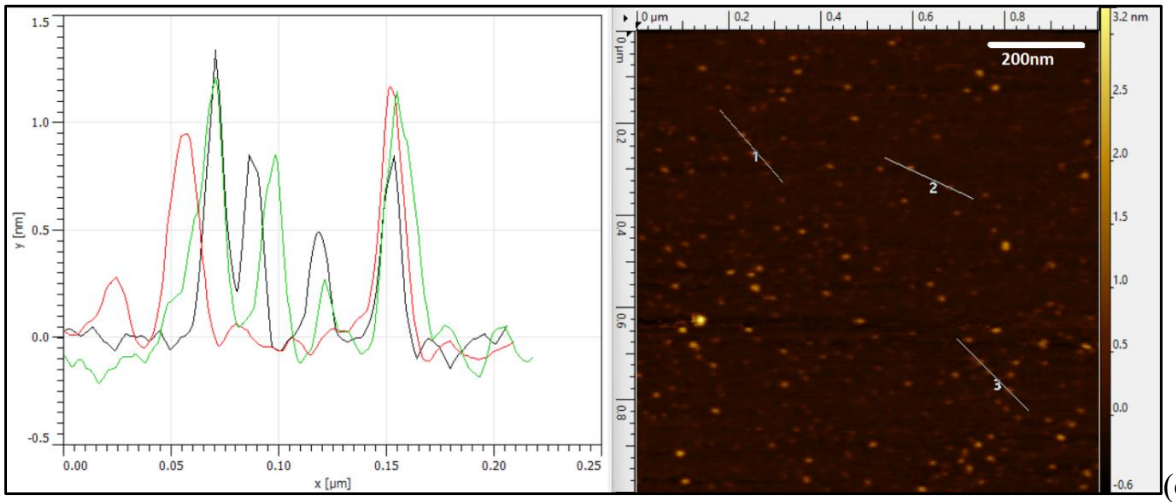


(e)

**Figure S1.2. XPS Survey Analysis of E-CNDs (a), Low P%-CNDs (b), High P%-CNDs (c), Low B%-CNDs (d), and High B%-CNDs (e).**

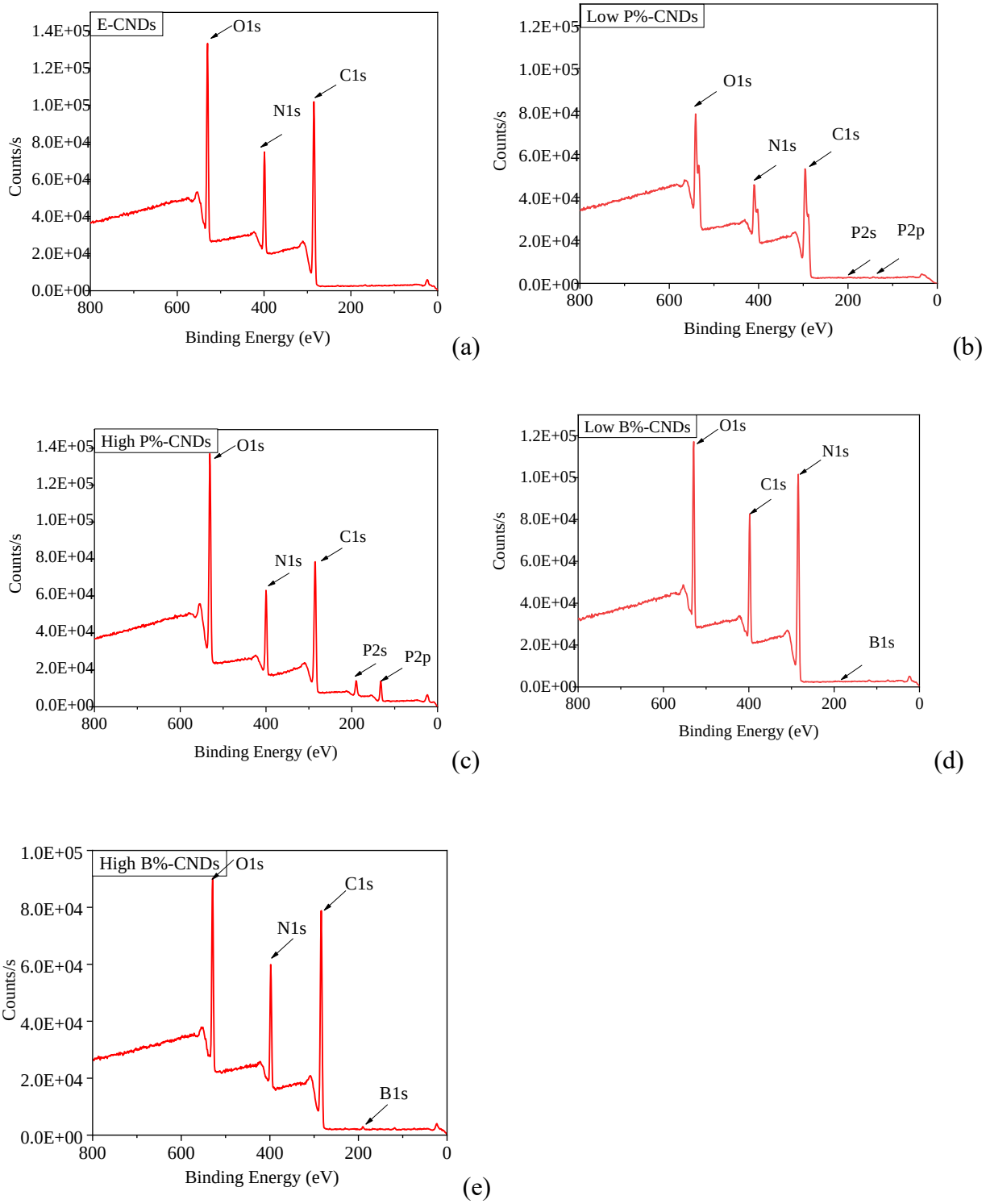

**Figure S1.3. XPS Scan of P 2p in Low P% CNDs (a), P 2p in High P% CNDs (b), B 1s in Low B% CNDs (c), B 1s in High B% CNDs (d), N 1s in E-CNDs (e) N 1s in High P%-CNDs (f), and N 1s in High B%-CNDs (g).**

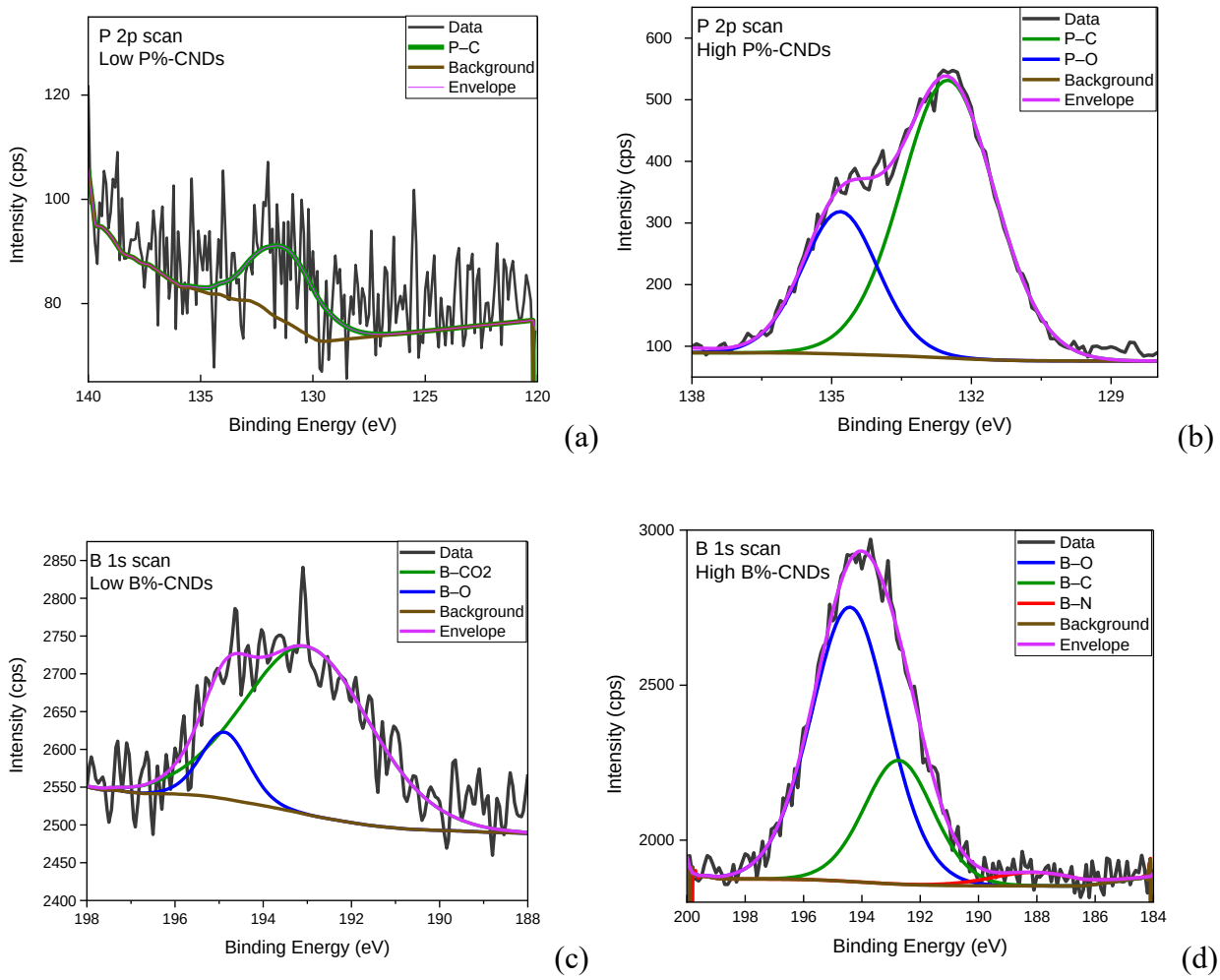

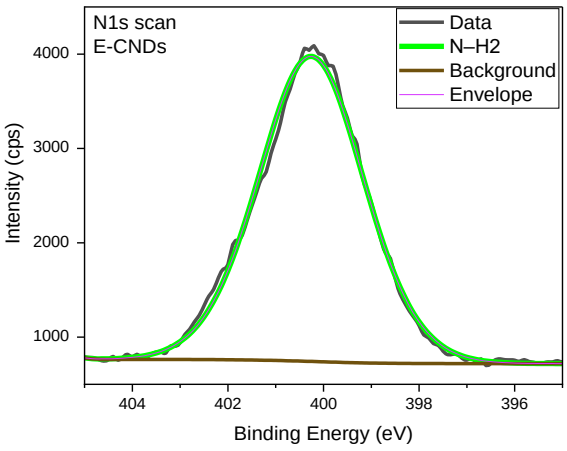
N1s scan
E-CNDs
Data
N–H2
Background
Envelope
Intensity (cps)
Binding Energy (eV)

(e)

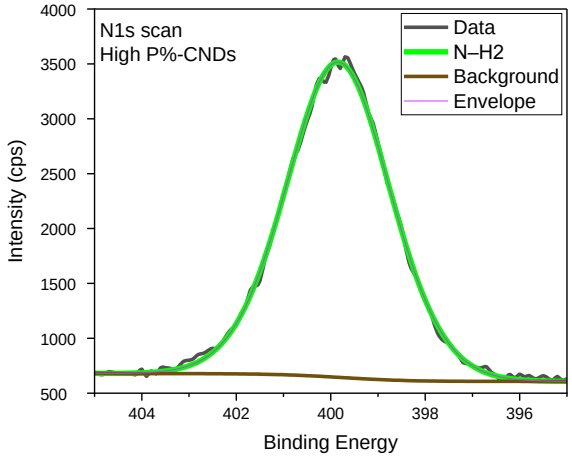
N1s scan
High P%-CNDs
Data
N–H2
Background
Envelope
Intensity (cps)
Binding Energy

(f)

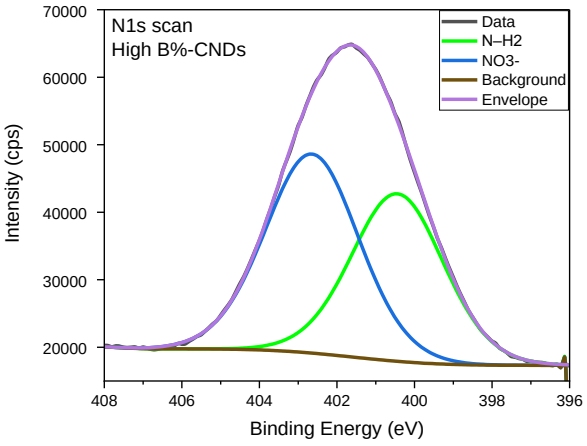
N1s scan
High B%-CNDs
Data
N–H2
NO3-
Background
Envelope
Intensity (cps)
Binding Energy (eV)

(g)

**Table S1.1. Percentage of Dopant Elements Across Different CND Samples Extracted from XPS Results**

| CNDs Type | Dopant element | atomic percentage |
|---|---|---|
| | P | B |
| E-CNDs | 0.04 | 0 |
| Low P%-CNDs | 0.38 | 0 |
| High P%-CNDs | 4.47 | 0 |
| Low B%-CNDs | 0 | 0.5 |
| High B%-CNDs | 0 | 1.95 |

**Table S1.2. Atomic Percentage of Detected Phosphorous Chemical Bonds by XPS.**

| | Low P%-CNDs | High P%-CNDs |
|---|---|---|
| P-C % | 100 | 70.05 |
| P-O % | 0 | 29.09 |
| P-N % | 0 | 0.86 |

**Table S1.3. Atomic Percentage of Detected Boron Chemical Bonds by XPS**

| | Low B%-CNDs | High B%-CNDs |
|---|---|---|
| B-COO % | 87.04 | 0 |
| B-O % | 12.96 | 68.69 |
| B-C % | 0 | 27.68 |
| B-N % | 0 | 3.62 |

**Figure S1.4. DLS Graph of E-CNDs (a), Low P%-CNDs (b), High P%-CNDs (c), Low B%-CNDs(d), and High B%-CNDs (e).**

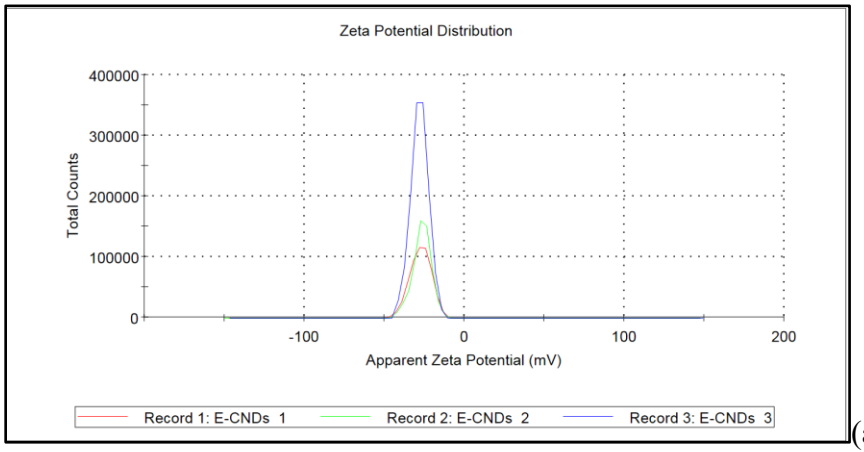

(a)

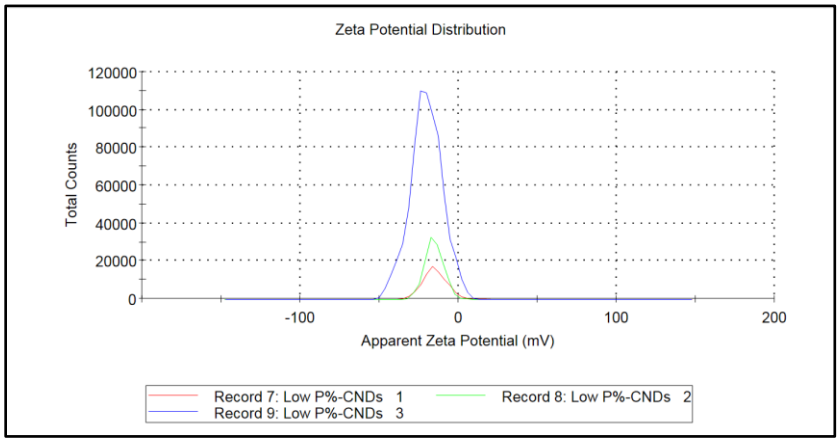

(b)

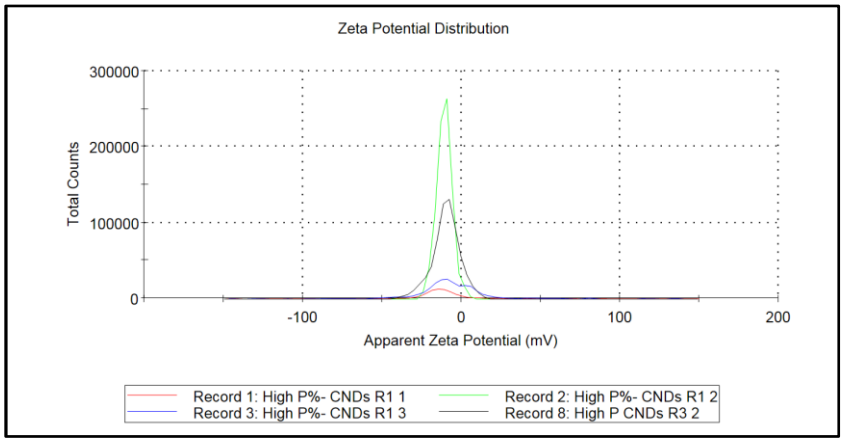

(c)

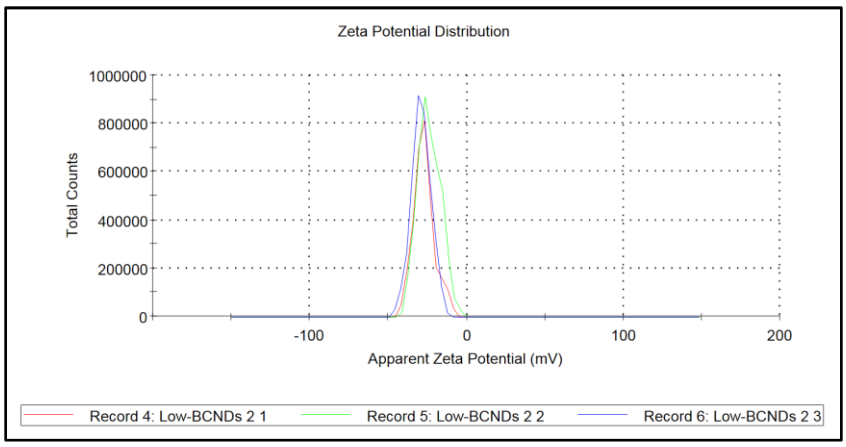
Zeta Potential Distribution
1000000
800000
600000
400000
200000
0
Total Counts
-100
0
100
200
Apparent Zeta Potential (mV)
Record 4: Low-BCNDs 2 1
Record 5: Low-BCNDs 2 2
Record 6: Low-BCNDs 2 3
(d)

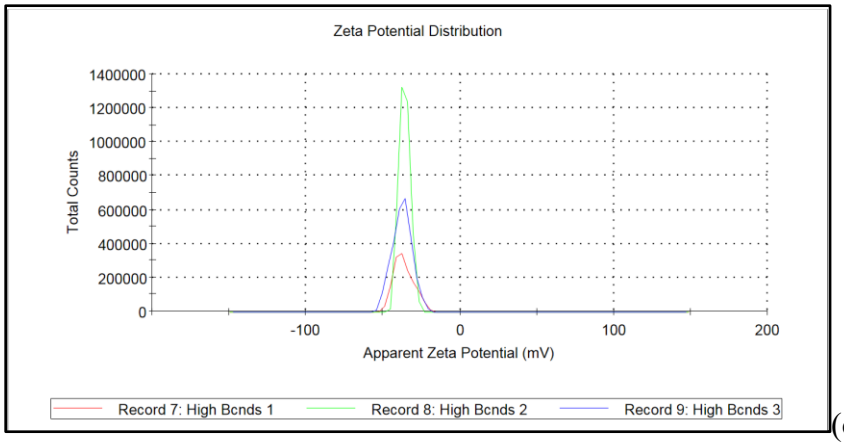
Zeta Potential Distribution
1400000
1200000
1000000
800000
600000
400000
200000
0
Total Counts
-100
0
100
200
Apparent Zeta Potential (mV)
Record 7: High Bcnds 1
Record 8: High Bcnds 2
Record 9: High Bcnds 3
(e)

**Figure S1.5. Zeta Potential Values of Different CNDs Samples (a), and ID/IG Ratios of E-CNDs, High P%-CNDs, and High B%-CNDs (b).**

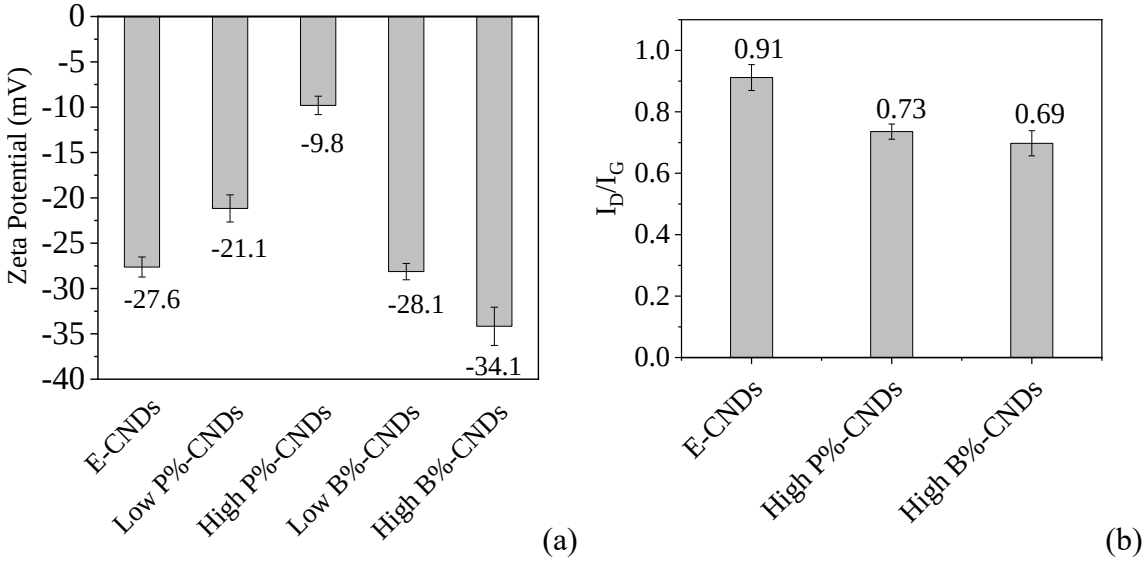

**Figure S1.6. Raman Spectra of E-CNDs, High P%-CNDs, and High B%-CNDs**

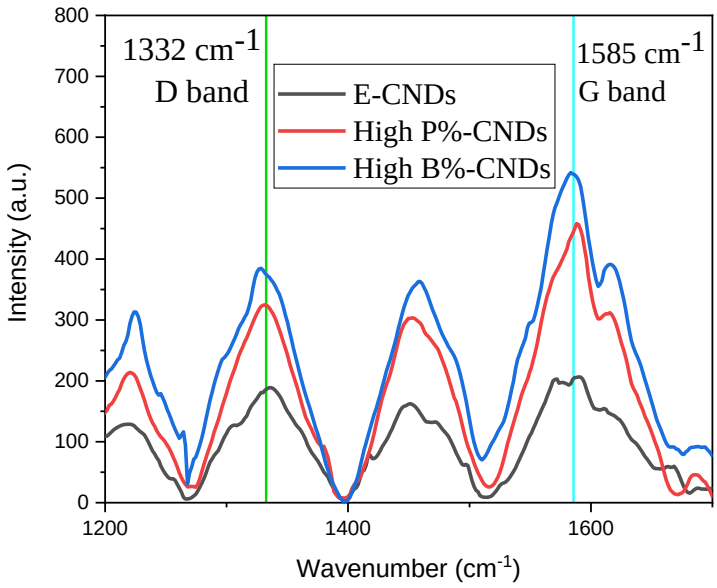

**Table S1.4. $I_D/I_G$ Ratios and Bond Lengths in Different CND Samples. The Bond Length Data were Obtained from National Institute of Standards and Technology (NIST[1]) Data base.**

| CNDs type | E-CNDs | High P%-CNDs | High B%-CNDs | All CNDs |
|---|---|---|---|---|
| $I_D/I_G$ ratio | 0.91 | 0.73 | 0.69 | – |
| Chemical Bond | C–N | C–P | C–B | C–C (average in graphite) |
| Length (pm) | 117 | 156 | 149 | 142 |
| Difference with C–C (%) | 17.46 | 9.85 | 4.92 | – |

[1] Computational Chemistry Comparison and Benchmark DataBase Standard - Reference Database 101, Experimental Diatomic bond lengths - Release 22 (May 2022) https://cccbdb.nist.gov/diatomicexpbondx.asp (Accessed 2023 -01 -21)

**Figure S1.7. The Tauc Plots Representing the Band-Gap Energy of CND Samples.**

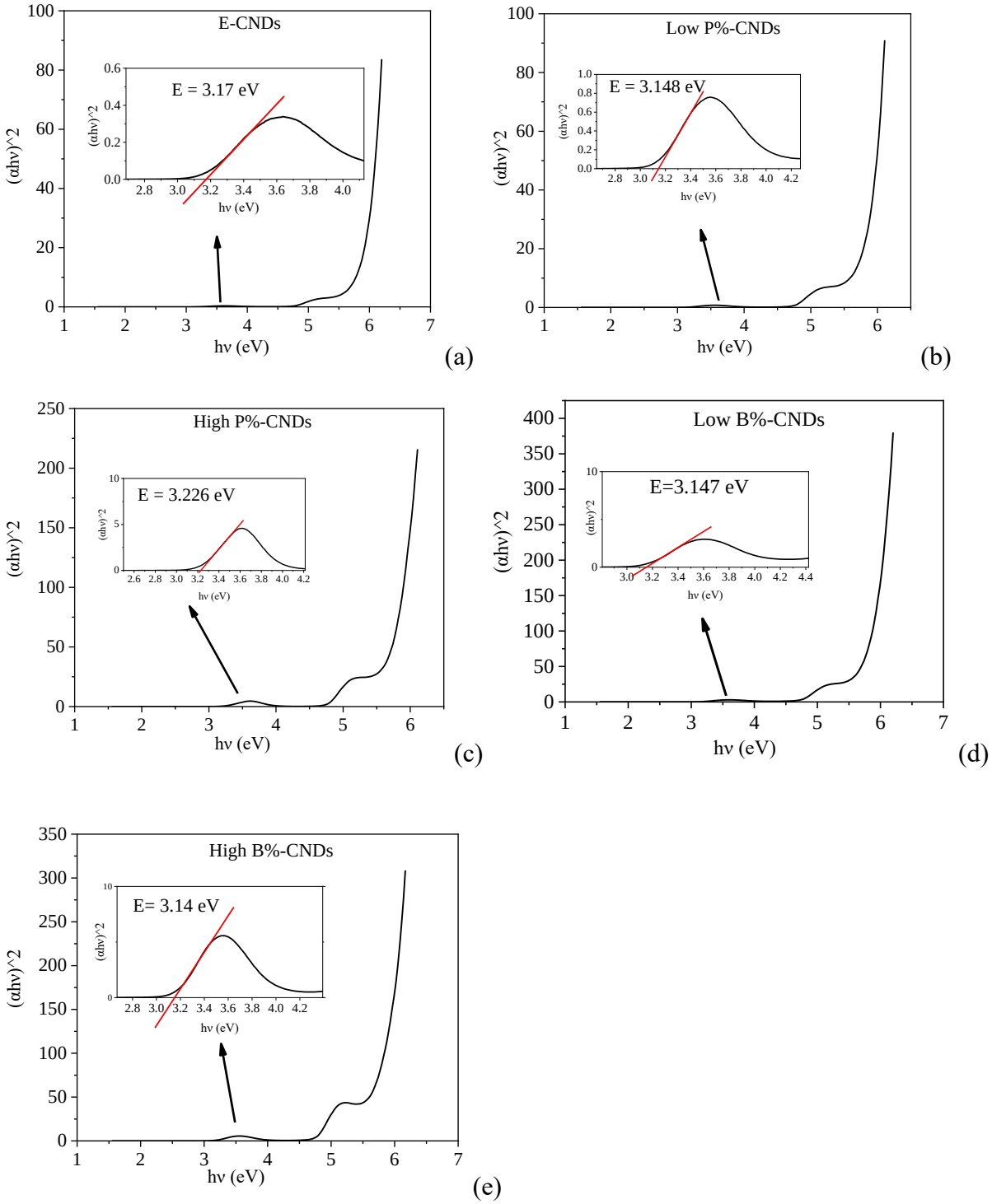

**Figure S1.8. Fluorescence Intensity of CND Samples**

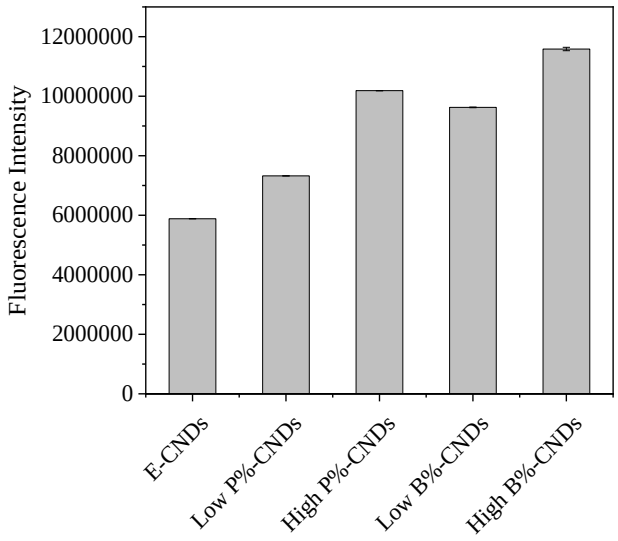

**Table S1.5. Dominance and Ratios of Fit Peaks' FWHM for E-CNDs, High P%-CNDs, and High B%-CNDs.**

| | E-CNDs | High P%-CNDs | High B%-CNDs |
|---|---|---|---|
| Dominance of Fit peak | 1 | 1 | 2 |
| FWHM of Fit peak 1/FWHM of Fit peak 2 | 0.63 | 0.62 | 0.58 |

**Figure S1.9. QY of CND Samples Compared to that of QS (a) and Calculated QY of CND Samples (b)**

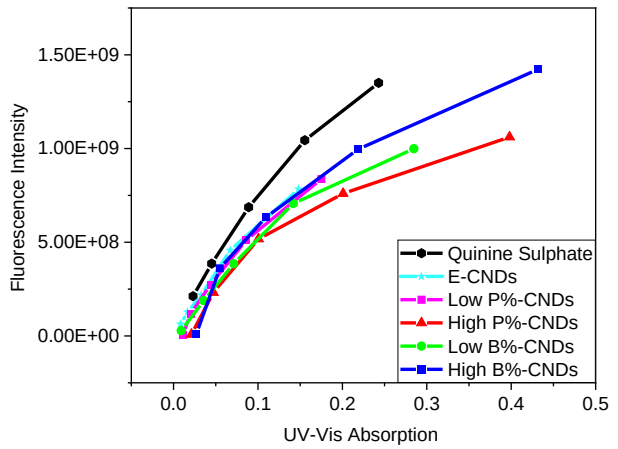


(a)

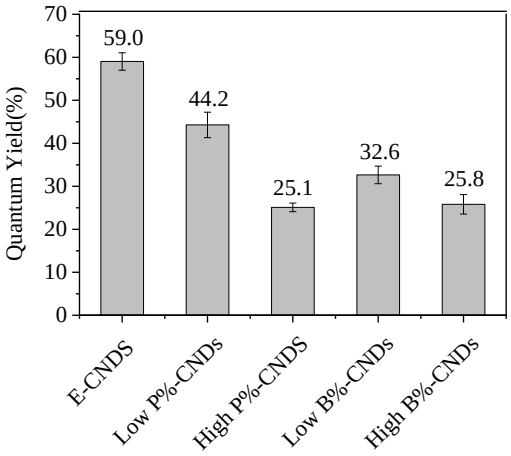


(b)

APPENDIX B: EFFECT OF CARBON NANODOTS DOPED WITH DIFFERENT HETEROATOMS ON THE OXIDATIVE STRESS IN CELLS AND THE PATTERN OF THE OXIDATIVE STRESS-RELATED GENE'S EXPRESSION

**Figure S2.1. AFM Results of N-CNDs (a), NP-CNDs (b), and NB-CNDs (c).**

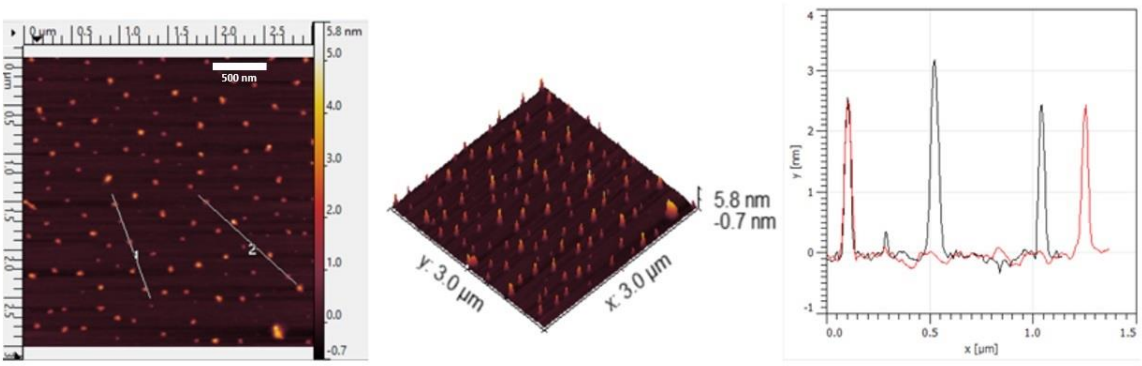


(a)

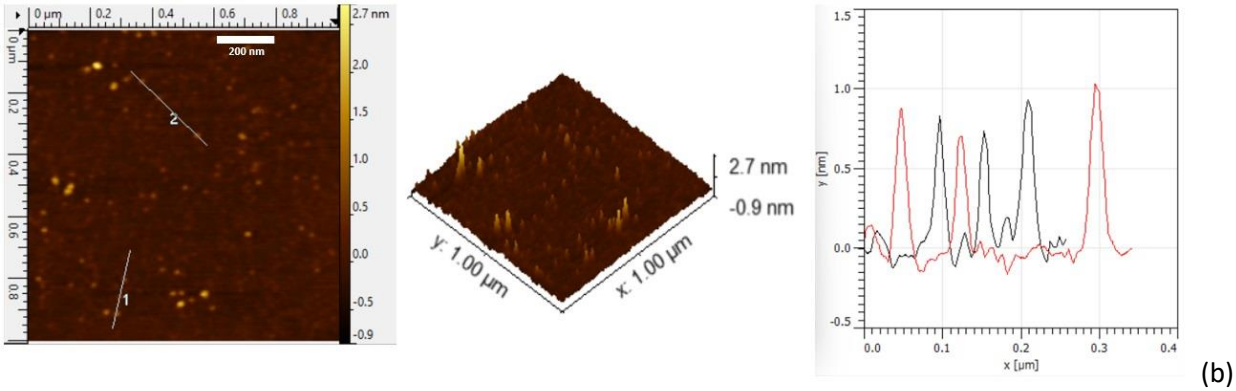


(b)

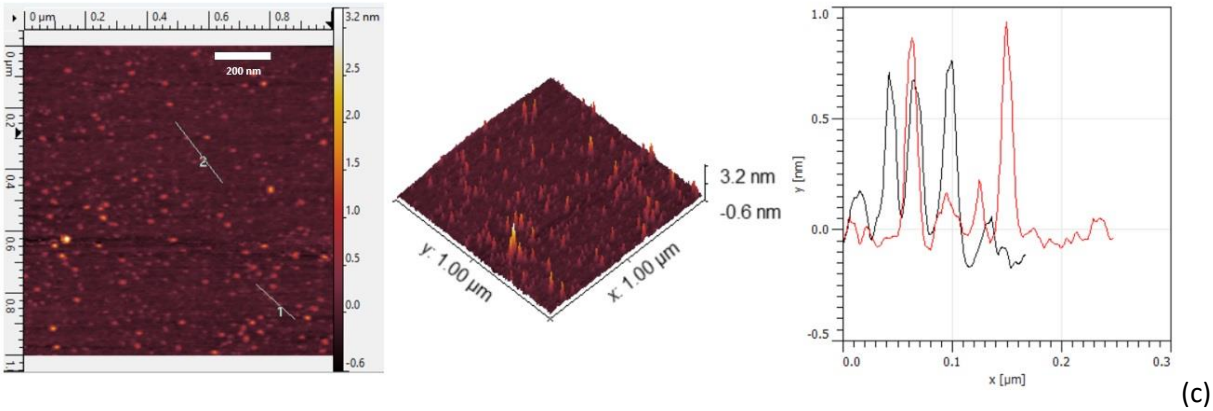
0 µm
0.2
0.4
0.6
0.8
3.2 nm
200 nm
2.5
2.0
1.5
1.0
0.5
0.0
-0.6
1
2
3.2 nm
-0.6 nm
y: 1.00 µm
x: 1.00 µm
1.0
0.5
0.0
-0.5
y [nm]
0.0
0.1
0.2
0.3
x [µm]

(c)

**Figure S2.2. DLS Graph of N-CNDs (a), NP-CNDs (b), and NB-CNDs (c).**

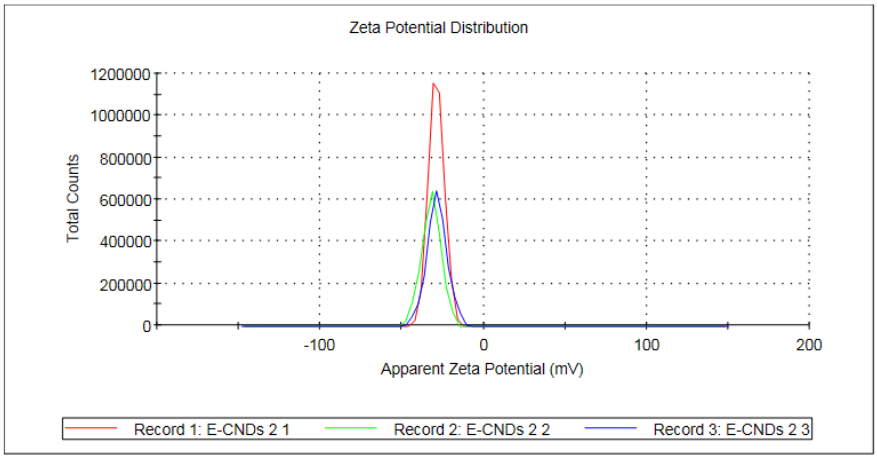


**(a)**

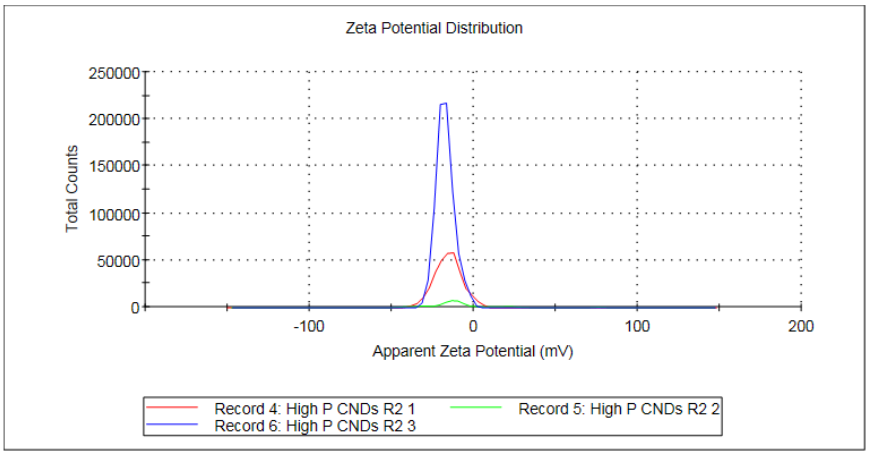


(b)

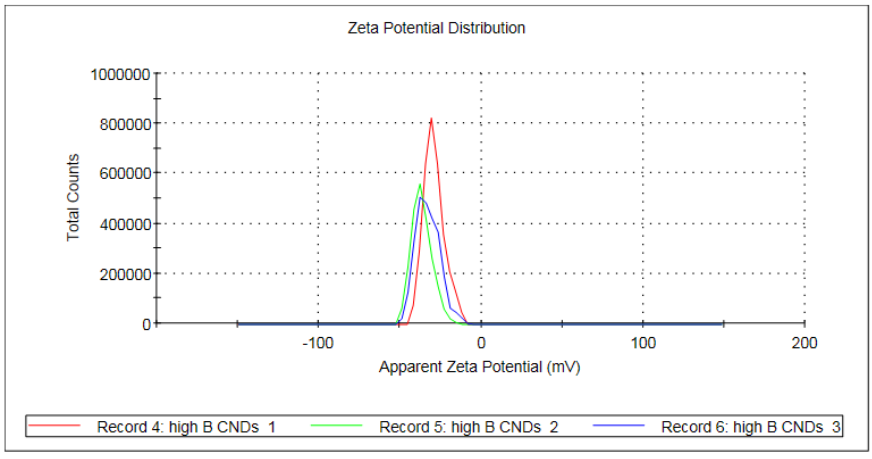


(c)

**Figure S2.3. XPS Survey Analysis of N-CNDs (a), NP-CNDs (b), and NB-CNDs (c)**

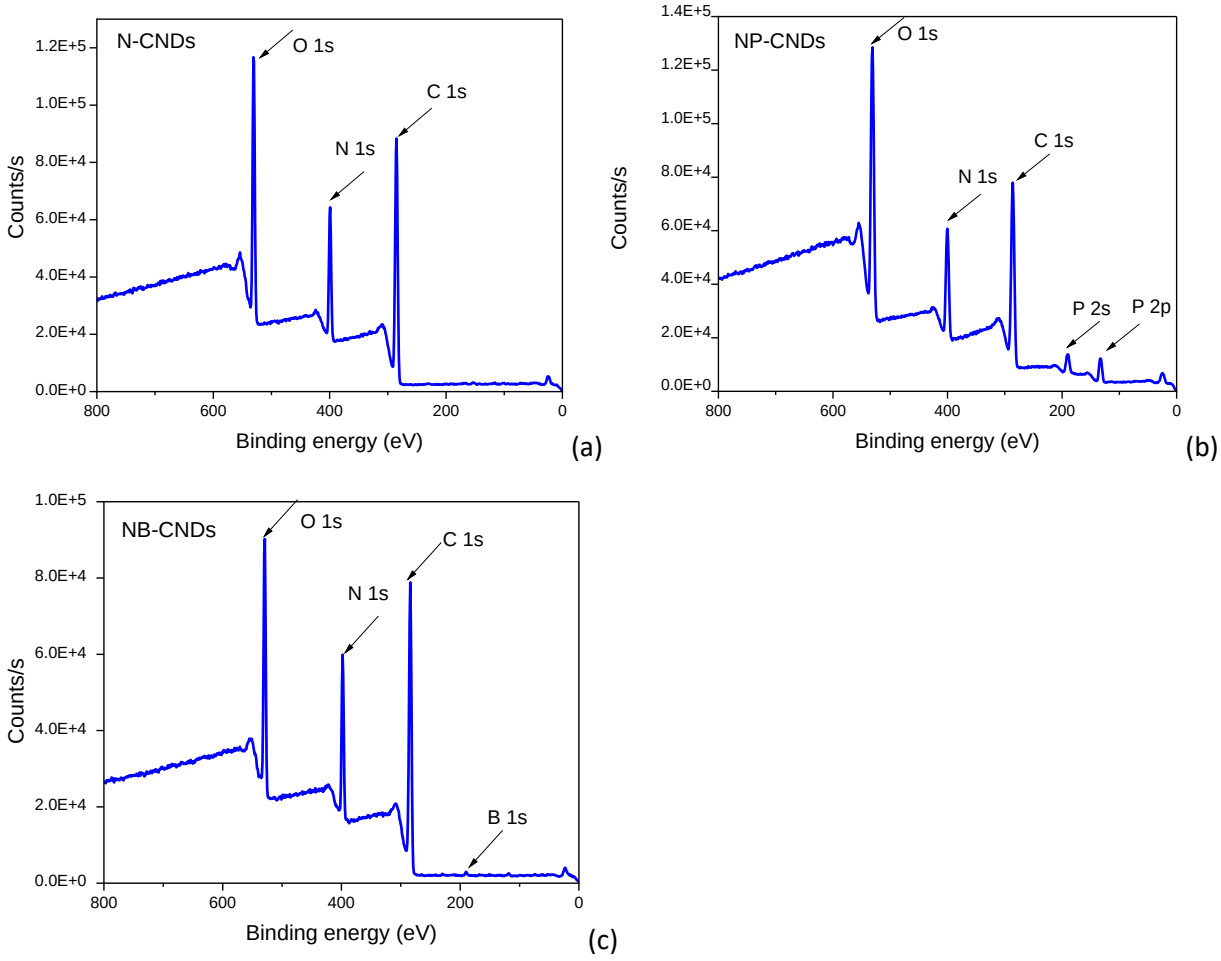

**Table S2.1. The Quantity of Dopant Elements in Different CND Samples Per XPS Results.**

| CNDs Type | Dopant element atomic percentage | |
|---|---|---|
| | P | B |
| N-CNDs | 0.04 | 0 |
| NP-CNDs | 4.47 | 0 |
| NB-CNDs | 0 | 1.95 |